

QUANTITATIVE TWO-PHOTON REDOX FLUORESCENCE MICROSCOPY OF
NEUROMETABOLIC DYNAMICS

A Dissertation

Presented to the Faculty of the Graduate School

of Cornell University

in Partial Fulfillment of the Requirements for the Degree of

Doctor of Philosophy

by

Harshad Dilip Vishwasrao

January 2005

© 2005 Harshad Dilip Vishwasrao

QUANTITATIVE TWO-PHOTON REDOX FLUORESCENCE MICROSCOPY OF NEUROMETABOLIC DYNAMICS

Harshad Dilip Vishwasrao, Ph.D.

Cornell University 2005

The fluorescence of the intracellular electron donor reduced nicotinamide adenine dinucleotide (NADH) is a well established probe of cellular metabolic state. This technique, called redox fluorimetry, can be combined with two-photon microscopy to provide functional imaging deep in living neural tissue with a spatio-temporal resolution far exceeding that of conventional functional imaging techniques (e.g. fMRI, PET). This resolution offers a new opportunity to explore spatio-temporal heterogeneities in the response of neural tissue to stressors such as metabolic inhibition and activity induced metabolic load. These metabolic responses were found to differ between cell types in the brain (astrocytes and neurons) and between sub-cellular compartments (mitochondria and cytosol). The time course of compartmental responses revealed that transient hypoxia caused an NADH increase followed by a post-hypoxic mitochondrial NADH hyperoxidation and a cytosolic lactate accumulation. A similar analysis of the time course of electrical activity induced metabolic responses revealed that the metabolic cost of neural activity was first met by oxidative neuronal metabolism followed by glycolytic metabolism in astrocytes.

The accuracy of redox-fluorimetry is limited however, by the effect of the local environment on the fluorescence of intracellular NADH. To characterize the effect of the intracellular environment on the photophysical properties of intracellular NADH, we measure its time resolved fluorescence and rotational anisotropy decays. These decays characterize the excited state and rotational dynamics of intracellular NADH, and from them we can infer how metabolic inhibition affects the enzyme binding states of NADH and the local viscosity for NADH rotational motion. The net effect is a reduction of the

average lifetime of intracellular NADH fluorescence upon metabolic inhibition, causing the fluorescence increase during inhibition to underestimate significantly the actual concentration increase.

Historically, measurements of the NADH response to metabolic perturbations have not significantly described the complexity of this response. The research presented here shows that metabolism associated changes of intracellular NADH are not only spatio-temporally heterogeneous, but also entail changes in the NADH conformation and its photophysical properties. By characterizing and accounting for these effects, we make progress towards quantitative redox-fluorimetry and the development of an accurate picture of in vivo NADH dynamics.

BIOGRAPHICAL SKETCH

Harshad Dilip Vishwasrao began his life on a balmy 7th of November, 1974 in Bombay, India. He spent his early years shuttling between the tropical west coast of India and the slightly chillier suburbs of St. Paul, Minnesota. Like many others, his interest in science began with dinosaurs, galaxies and Transformers. But his particular focus on physics would wait until he chanced upon Eddington's treatise on relativity in the libraries of Bombay Scottish School – a middle school more renowned for its illustrious show business alumni than for its scientists. This fascination with physics proved to be enduring and, together with a predilection for cutting class, followed him to college. Despite his abysmal attendance record, Harshad graduated magna cum laude in 1997 from the University of Pennsylvania with majors in physics and mathematics. It was at Penn that he first learned of the complex interface between physics and biology. The idea of mathematical reducibility in systems as complex as Life was entrancing and led to graduate study with Watt Webb at Cornell University. At Cornell, he did his doctoral research on the imaging and spectroscopy of neuro-metabolic dynamics and went on to a post-doctoral research position in neurobiology at Columbia University.

ACKNOWLEDGEMENTS

It has been said that Prometheus was the first graduate student. Then I cannot help but think that his tortured existence would have been mollified somewhat by a friend with a sympathetic ear ... and a can of eagle repellent. Over the past seven years Jessica, John, Merlin, Kat and Kevin have kept me sane, if not always sober. I will always be grateful for the camping trips, the drives around the lake, the home-cooked meals, Friday night movies and Taco Bell dinners. And the occasional squirt of eagle repellent.

No tale is complete without a telling – and most of this thesis was whispered to a laptop over an endless stream of americano at Autumn Leaves Used Books. To Liz, Heather, Logan, Joe, Neil, Jeff and the rest of the usuals and unusuals at Autumn Leaves: a big thanks for the camaraderie and the caffeine.

I would like to thank Watt Webb for his guidance and his uncanny ability to assemble talented, generous people. The Webb Group has been the ideal environment to learn and explore, and I owe a debt of gratitude to its members that made it a joy to work in a windowless basement every day. To Ahmed Heikal and Karl Kasischke, who have taught me so much of what I know – I can only hope that I was a good student. To Warren Zipfel and Becky Williams for advice, commiseration, fancy coffee and for not telling Prof. Webb about all of the *other* things that I broke. To Mike Levene for his discourses on optics and socio-economics, both of which he delivered in Fourier space. To Dan Dombeck for being a source and sounding board for ideas great and small. And to his wife Liz for all the great material. To Ray Molloy, who has always had the answer, even if it was somewhat inaudible. To Liz Rhoades for all the cupcakes, literal and metaphorical. To Sally ‘Tato’ Kim for just being the nicest person ever. To Dan Larson, together we gave something back to the

Webb Group – a stolen sofa. To Sam Hess for my first and only flying lesson. And to the rest of the Webb Group, it has been my deepest honor.

Lastly, I would like to thank my family ... for simply being there.

TABLE OF CONTENTS

1. Introduction	1
1.1 Biological context and motivation	1
1.2 Towards quantitative redox fluorimetry	3
2. Background and experimental procedures	8
2.1 Overview of Cellular Energy Metabolism	8
2.1.1 Pathways of NADH oxidation and reduction	8
2.1.2 Mitochondrial NADH level	11
2.2 Two-photon fluorescence microscopy	16
2.3 Steady state (wavelength resolved) spectroscopy	18
2.3.1 Solution steady state fluorescence spectroscopy	18
2.3.2 In vivo fluorescence spectroscopy: scanning stage technique	19
2.3.3 In vivo fluorescence spectroscopy: wavelength resolved spectroscopy	19
2.4 Time resolved fluorescence spectroscopy	20
2.4.1 Definition of fluorescence and anisotropy decay	20
2.4.2 Experimental set-up	21
2.4.3 Functional form of fluorescence decay	23
2.4.4 Functional form of fluorescence anisotropy decay	25
2.4.5 Fitting protocol	27
2.4.6 G factor determination	31
2.4.7 Number of decay components	32
2.5 The hippocampal brain slice	33
2.5.1 Hippocampal slice architecture	33
2.5.2 Sample preparation	35
2.5.2.1 Primary dissociated neuronal cultures	35
2.5.2.2 Acute hippocampal slices	35
2.5.3 Slice maintenance: perfusion chambers	36
2.5.3.1 Open chamber	36
2.5.3.2 Closed chamber	38
2.5.4 Surface damage due to preparation	39
2.5.5 Photobleaching and photodamage	41
2.6 Diffusion of oxygen into tissue	42
2.6.1 The reaction diffusion equation	42
2.6.2 Approximations to the reaction diffusion equation	44
2.6.3 Steady state oxygen profile in a brain slice	46
3. Intrinsic fluorescence in brain tissue	51
3.1 Sources of intrinsic signals in brain tissue (other than NADH)	51
3.1.1 Amino acids	52
3.1.2 Retinoids	52

3.1.3	Lipofuscin	54
3.1.4	Microtubules	54
3.1.5	Induced autofluorescence	55
3.1.6	NADPH	57
3.1.7	Flavins	58
3.2	Identification of NADH	58
3.2.1	Morphology of intrinsic fluorescence	59
3.2.1.1	Cultured neural cells	59
3.2.1.2	Acute hippocampal slices	60
3.2.2	Pharmacological response of intrinsic fluorescence	62
3.2.2.1	Response of cultured neurons and glial cells to inhibition and uncoupling	63
3.2.2.2	Response of intrinsic fluorescence in brain slices to cyanide	63
3.2.2.3	Oxygen dependence of intrinsic fluorescence in brain slices	66
3.2.3	Steady state (wavelength resolved) spectroscopy of intrinsic fluorescence	68
3.3	Intrinsic fluorescence in astrocytes versus neuropil	73
3.3.1	Glial cells in the hippocampus	73
3.3.2	NADH fluorescence in GFAP-GFP labeled astrocytes	75
3.4	Conclusions	79
4.	Imaging <i>in vivo</i> NADH dynamics	83
4.1	Motion correction	83
4.1.1	Strategy for motion correction	84
4.1.2	Measures of image similarity	85
4.1.3	Extrapolating motion correction from an image pair to an image series	89
4.1.4	Reduction of motion artifact	90
4.1.5	Post motion correction artifact in intensity based region of interest selection: difference-intensity anti-correlation	93
4.1.6	Limitation of motion correction protocol	97
4.2	NADH response to hypoxia induced metabolic inhibition	98
4.2.1	Energy metabolism in resting neurons	98
4.2.2	Effects of hypoxia	99
4.2.3	Analysis of hypoxia time series	101
4.2.3.1	Structure of time series	101
4.2.3.2	Motion correction and sub-series definition	102
4.2.3.3	Intensity changes of percentile bins	104
4.2.3.4	Discussion of heterogeneous response to hypoxia	107
4.2.4	Conclusions	108
4.3	NADH response to activity induced metabolic load	109
4.3.1	Energy metabolism in active neurons	109

4.3.2	Stimulation and imaging protocol	110
4.3.3	Image analysis protocol	111
4.3.3.1	Motion correction	111
4.3.3.2	Criterion for significance of response	112
4.3.3.3	Definition of overshoot and dip masks	112
4.3.3.4	Application of dip and overshoot masks	114
4.3.4	Results of analysis	114
4.3.4.1	Correlation of dip and overshoot regions	114
4.3.4.2	Baseline intensity histograms of dip and overshoot regions	117
4.3.4.3	Time evolution of the dip and overshoot regions	118
4.3.5	Discussion of heterogeneous response to activity	119
4.3.6	Conclusion	121
5.	NADH conformation and concentration in brain tissue	125
5.1	Introduction to intracellular NADH conformation and concentration	125
5.2	Photophysics of NADH in solution	127
5.2.1	Aqueous solution	127
5.2.2	Environmental effects	128
5.2.2.1	Viscosity	128
5.2.2.2	Enzyme binding	130
5.2.2.3	pH	131
5.2.2.4	Oxygen quenching	132
5.2.3	Strickler-Berg calculation of radiative rate	133
5.3	Fluorescence anisotropy and lifetime in tissue	137
5.3.1	Tissue fluorescence measurements	137
5.3.1.1	Fluorescence decay functional form	138
5.3.1.2	Average fluorescence decay parameters	140
5.3.2	Comparative measurements of NADH in solution	144
5.3.3	Identification of intracellular free and enzyme bound NADH	146
5.3.4	Calculating the local intracellular viscosity	148
5.3.5	Discussion of intracellular NADH conformation and environment	148
5.4	Regional variations of intrinsic NADH photophysics	151
5.5	Concentration calibration of intracellular NADH	153
5.6	Optical properties of brain slices	157
5.6.1	Absorption	157
5.6.2	Scattering	159
5.7	Conclusions	160

LIST OF FIGURES

Figure 1.1 NADH and NAD ⁺ form a redox pair	3
Figure 1.2 Current state of redox-fluorimetry	4
Figure 2.1 Cellular pathways of NADH oxidation and reduction	9
Figure 2.2 Regulation of mitochondrial [NADH]/[NAD ⁺] level	12
Figure 2.3 Generic two-photon laser scanning microscope	16
Figure 2.4 Two-photon scanning stage spectroscopy apparatus	22
Figure 2.5 Anisotropy and lifetime global analysis fitting algorithm	30
Figure 2.6 G Factor determination using coumarin as a fluorescence standard	32
Figure 2.7 Architecture of the hippocampal slice	34
Figure 2.8 Open slice perfusion chamber	37
Figure 2.9 Hypoxia induced metabolic inhibition is possible even in an open slice chamber	38
Figure 2.10 Closed slice perfusion chamber	39
Figure 2.11 Live-Dead assay of depth dependent cell viability	40
Figure 2.12 Semi-infinite approximation of a brain slice to calculate the oxygen gradient	46
Figure 2.13 Oxygen profile in a brain slice	47
Figure 3.1 SHG from aligned microtubules in axons	55
Figure 3.2 Induced autofluorescence due to severe photodamage	56
Figure 3.3 Intrinsic fluorescence in cultured neurons and glial cells	59
Figure 3.4 Colocalization of NADH and Rh123 in cultured neurons and hippocampal slices	61
Figure 3.5 Response of intrinsic fluorescence in cultured neurons to inhibition and uncoupling	63
Figure 3.6 Response of hippocampal brain slice to cyanide	64
Figure 3.7 Temporal response of brain slice intrinsic fluorescence to cyanide	65
Figure 3.8 Dose dependence of intrinsic fluorescence to cyanide	66
Figure 3.9 Response of brain slice intrinsic fluorescence to transient hypoxia	67
Figure 3.10 Bath oxygen dependence of intrinsic fluorescence	68
Figure 3.11 Power dependence of aqueous NADH fluorescence and intrinsic fluorescence	69
Figure 3.12 Spectroscopic identification of intrinsic NADH	70
Figure 3.13 Response of the yellow tissue fluorescence to hypoxia	71
Figure 3.14 Effect of enzyme binding on NADH fluorescence	72
Figure 3.15 Intrinsic fluorescence image showing glia in the neuropil	74
Figure 3.16 GFP labeled astrocytes in a transgenic mouse hippocampus	76
Figure 3.17 Identification of astrocytes by GFAP-GFP and NADH	77
Figure 3.18 Immunostain for GFAP in fixed brain tissue	78
Figure 3.19 NADH fluorescence versus GFAP-GFP fluorescence around a typical astrocyte	79

Figure 4.1 Strategy for motion correction	85
Figure 4.2 Pairwise calculation of relative shift vector	87
Figure 4.3 Correlation decays show motion correction reduces motion artifact	92
Figure 4.4 Difference-intensity anti-correlation	94
Figure 4.5 Methods of reducing intensity dependent spontaneous intensity changes	97
Figure 4.6 Mean intensity of intrinsic fluorescence during transient hypoxia	103
Figure 4.7 Intensity histograms of intrinsic fluorescence during transient hypoxia	105
Figure 4.8 Response of the brightest and dimmest pixels to hypoxia	106
Figure 4.9 Spatial relation of dip, overshoot and NADH	115
Figure 4.10 Baseline intensity histograms of dip region (green), overshoot region (red) and entire tissue (black)	117
Figure 4.11 Response of intrinsic fluorescence to stimulation	119
Figure 5.1 Effect of viscosity on NADH photophysics	129
Figure 5.2 Calculated change in the radiative rate due to simulated fluorescence spectral shift	134
Figure 5.3 Calculated change in radiative rate due to simulated absorption shift	135
Figure 5.4 Strickler-Berg relation predicts the radiative rate of free NADH in a viscous environment	136
Figure 5.5 Case study - number of components required for tissue fluorescence decay fit	139
Figure 5.6 Intrinsic fluorescence decays	140
Figure 5.7 Anisotropy decays of intrinsic fluorescence	142
Figure 5.8 Anisotropy of free and bound NADH	145
Figure 5.9 Lifetimes and hypoxic responses of different hippocampal regions	153
Figure 5.10 Calibrating intrinsic NADH fluorescence to concentration	154
Figure 5.11 Map of NADH concentration - before correcting for quantum yield	155

LIST OF TABLES

Table 2.1 Mechanisms of effectors of mitochondrial NADH	14
Table 2.2 Accuracy of models of oxygen consumption kinetics	43
Table 3.1 Fluorescent amino acids	52
Table 4.1 Summary of measures of image similarity	89
Table 5.1 Effect of enzyme binding on NADH photophysics	131
Table 5.2 Excited state decay rates of aqueous NADH under aerobic conditions	133
Table 5.3 Mean (SEM) fit parameters for intrinsic fluorescence decays	141
Table 5.4 Mean (SEM) anisotropy decay fit parameters	143
Table 5.5 Summary of intrinsic NADH conformation identification	146
Table 5.6 Correction factors for estimating intrinsic NADH concentration	156

LIST OF ABBREVIATIONS

2PM – two-photon microscopy

ACSF – artificial cerebro-spinal fluid

ATP – adenosine triphosphate

CA1 – cell area 1

CA3 – cell area 3

CNS – central nervous system

DG – dentate gyrus

ETC – electron transport chain

FAD⁺ or FADH₂ – flavin adenine dinucleotide (oxidized or reduced)

MPM – multi-photon microscopy

NA – numerical aperture

NADH or NAD⁺ – beta nicotinamide adenine dinucleotide (reduced or oxidized)

NADPH or NADP⁺ - beta nicotinamide adenine dinucleotide phosphate (reduced or oxidized)

PMT – photomultiplier tube

SLM – stratum lacunosum-moleculare

SO – stratum oriens

SP – stratum pyramidale

SR – stratum radiatum

Chapter One

Introduction

1.1 Biological context and motivation

Metabolism in the central nervous system (CNS) remains an area of active research and profound controversy (1). This controversy surrounds every scale of neural systems – from sub-cellular and cellular metabolic compartments to functional regions in the brain. At the smallest scale – the distribution of metabolic load between aerobic and anaerobic processes remains controversial (2,3). The role of astrocytes and neurons in supplying energy for rapid electrical activity and whether the demand is dominated by pre-synaptic or post-synaptic processes (4) is also uncertain. There is even evidence that chronic inhibition of mitochondrial metabolism is linked to neurodegenerative diseases (5).

The wealth of open questions in the field of neurometabolism requires techniques that can monitor rapid changes in metabolic processes on a cellular and sub-cellular level. Current techniques to probe neural energy metabolism are limited by either temporal or spatial resolution. Metabolic mapping techniques have revealed

the distribution and/or activities of metabolic enzymes on regional, cellular and sub-cellular scales in the brain. However these techniques, which include 2-deoxyglucose autoradiography (6,7) and cytochrome oxidase histochemistry (8) require fixation and staining of tissue, making them ill suited for the study of rapid metabolic dynamics in living systems.

In contrast, *in situ* techniques such as positron emission tomography (PET) and functional magnetic resonance imaging (fMRI) are routinely used in measuring neuro-metabolic and neuro-vascular dynamics in living subjects. PET utilizes ^{18}F -fluorodeoxyglucose as a tracer to image glucose metabolism in the intact brain (9). Functional magnetic resonance imaging utilizes changes in the blood oxygen content as an indirect measure of neuronal activity (10). However the spatial resolution of these techniques ($\gg 1\text{mm}$), possibly to the level of single cortical columns, while adequate to discriminate macroscopic anatomical regions in the brain, is insufficient to resolve metabolic processes on a cellular level. Two-photon microscopy (2PM) (11) provides an ideal technique for high-resolution fluorescence imaging in highly scattering tissue such as brain (12,13).

Reduced nicotinamide adenine dinucleotide (NADH) - a fluorophore intrinsic to most tissues - is also the principal carrier of reducing equivalents in energy metabolism. NADH and its non-fluorescent oxidized form NAD^+ form a redox pair (Fig.(1.1)) whose population ratio ($[\text{NADH}]/[\text{NAD}^+]$), as measured by intrinsic NADH fluorescence, is a well established probe of metabolic state in systems ranging from cultured cells to intact tissue (14,15). This technique, known as redox-fluorimetry, has traditionally used UV light to excite NADH fluorescence. Due to the low penetration of UV light into tissue, fluorescence is excited from essentially only the surface of the tissue. Combining redox-fluorimetry with 2PM however provides

the opportunity to monitor metabolic dynamics, with high resolution, deep in functioning neural tissue.

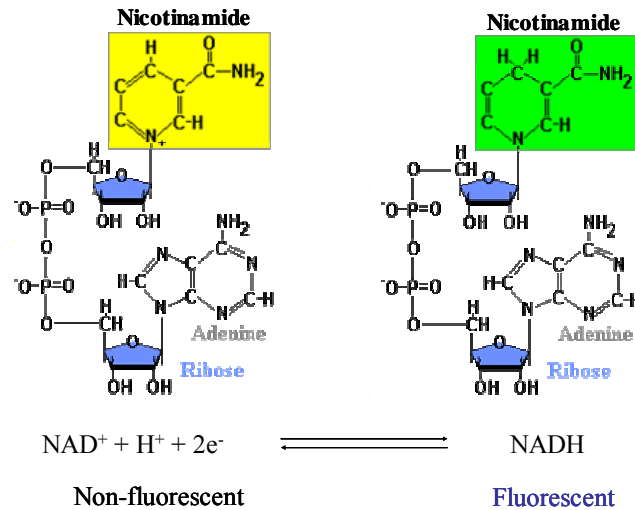


Figure 1.1 NADH and NAD⁺ form a redox pair. NAD has two nucleotide rings – adenine and nicotinamide. The nicotinamide ring is fluorescent in NADH but not in NAD⁺.

1.2 Towards quantitative redox-fluorimetry

Numerous theoretical treatments of cellular and mitochondrial metabolism have been developed (16-20) to elucidate the relationship between NADH concentration and other metabolic parameters such as rate of oxygen consumption, levels of ATP and other intermediate metabolites. The synthesis of these theoretical treatments with experimental measurements from redox-fluorimetry aims to develop a complete picture of *in vivo* cellular metabolism.

To achieve this synthesis however, we must be able to measure the *in vivo* concentration of NADH rather than just the fluorescence. Quantifying *in vivo* NADH concentration dynamics involves characterizing the effect of a number of factors

which can broadly be categorized as physiological factors, molecular factors and optical factors (Fig. 1.2).

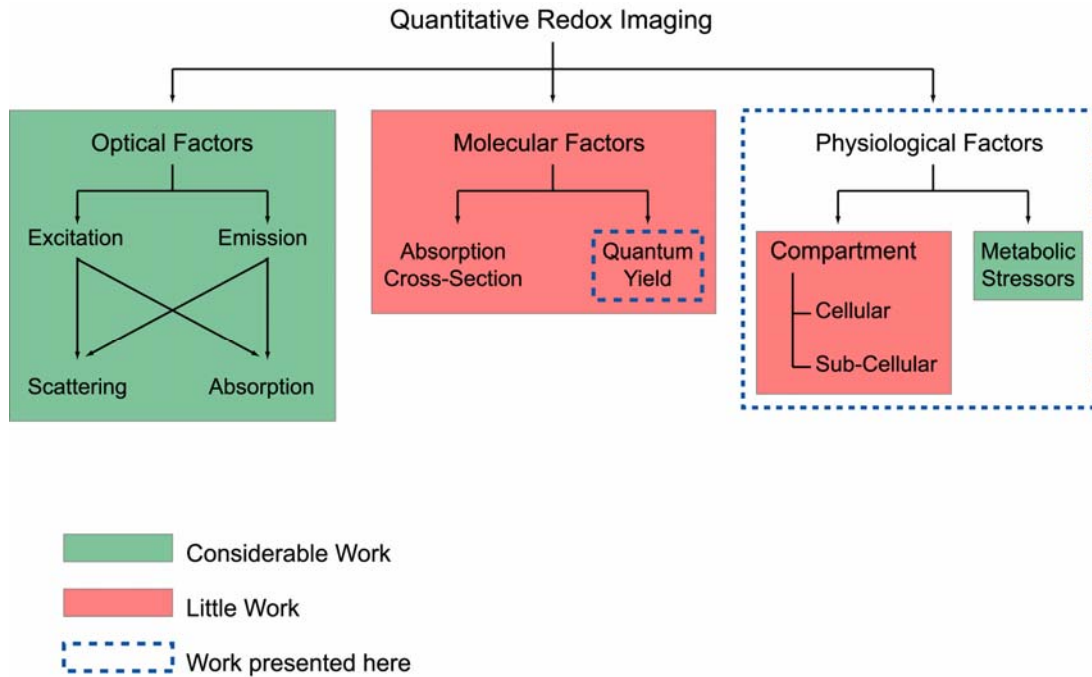


Figure 1.2 Current state of redox fluorimetry

Physiological Factors: Intracellular NADH fluorescence and its response to metabolic stressors (e.g. metabolic load, inhibition, etc.) have been well characterized in many systems. However, until recently, redox-fluorimetric techniques have lacked the spatio-temporal resolution to explore the heterogeneity of this fluorescence and its dynamics in the brain. Combining the high resolution of 2PM of intrinsic NADH with motion correction algorithms, we are able to follow differences in the neurometabolic dynamics of cellular and sub-cellular compartments. Motion corrected two-photon redox fluorimetry of neurometabolism is developed in Chapters 3 and 4.

Molecular Factors: The fluorescence observed in 2PM depends on not just the fluorophore concentration (C) but also on the photophysical properties of the fluorophore itself, specifically its 2P absorption cross-section (σ_2) and fluorescence

quantum yield (Φ_f) (21). The quantum yield of NADH is known to be affected by its local environment and isomerization state. As a result, inferring intracellular NADH concentration from its fluorescence requires a characterization of the intracellular NADH conformation and local environment, presented here in Chapter 5. A consideration of the two-photon absorption cross-section of intracellular NADH will not be presented as, to date, no good method exists to measure σ_2 in tissue.

Optical Factors: Both the excitation and emission light is attenuated due to wavelength dependent scattering and absorption in brain tissue – considerable work has been done on characterizing these effects by other researchers, and hence their results will be summarized only briefly in Chapter 5.

The work presented here represents an extension of conventional redox-fluorimetry. By furthering the ability to quantify intracellular NADH concentration and resolve the fine spatial structure of its dynamics, we come closer to being able to quantitatively describe neural energy metabolism in native neural tissue.

References

1. Barinaga, M. (1997) *Science* **276**, 196-198
2. Fox, P. T., Raichle, M. E., Mintun, M. A., and Dence, C. (1988) *Science* **241**, 462-464
3. Malonek, D., and Grinvald, A. (1996) *Science* **272**, 551-554
4. Dirocco, R. J., Kageyama, G. H., and Wongriley, M. T. T. (1989) *Computerized Medical Imaging and Graphics* **13**, 81-92
5. Beal, M. F. (1992) *Annals of Neurology* **31**, 119-130
6. Sokoloff, L., Reivich, M., Kennedy, C., Desrosiers, M. H., Patlak, C. S., Pettigrew, K. D., Sakurada, O., and Shinohara, M. (1977) *Journal of Neurochemistry* **28**, 897-916
7. Kennedy, C., Desrosiers, M. H., Jehle, J. W., Reivich, M., Sharpe, F., and Sokoloff, L. (1975) *Science* **187**, 850-853
8. Kageyama, G. H., and Wongriley, M. T. T. (1982) *Neuroscience* **7**, 2337-2361
9. Reivich, M., Kuhl, D., Wolf, A., Greenberg, J., Phelps, M., Ido, T., Casella, V., Fowler, J., Hoffman, E., Alavi, A., Som, P., and Sokoloff, L. (1979) *Circulation Research* **44**, 127-137
10. Ogawa, S., Lee, T. M., Kay, A. R., and Tank, D. W. (1990) *Proceedings of the National Academy of Sciences of the United States of America* **87**, 9868-9872
11. Denk, W., Strickler, J. H., and Webb, W. W. (1990) *Science* **248**, 73-76
12. Denk, W., and Svoboda, K. (1997) *Neuron* **18**, 351-357
13. Helmchen, F., Fee, M. S., Tank, D. W., and Denk, W. (2001) *Neuron* **31**, 903-912
14. Chance, B., and Thorell, B. (1959) *Nature* **184**, 931-934
15. Chance, B., Jobsis, F., Schoener, B., and Cohen, P. (1962) *Science* **137**, 499-&
16. Aubert, A., Costalat, R., and Valabregue, R. (2001) *Acta Biotheoretica* **49**, 301-326
17. Wilson, D. F., Owen, C. S., and Erecinska, M. (1979) *Archives of Biochemistry and Biophysics* **195**, 494-504
18. Jin, Q. S., and Bethke, C. M. (2002) *Biophysical Journal* **83**, 1797-1808

19. Korzeniewski, B., and Zoladz, J. A. (2001) *Biophysical Chemistry* **92**, 17-34
20. Jafri, M. S., Dudycha, S. J., and O'Rourke, B. (2001) *Annual Review of Biomedical Engineering* **3**, 57-81
21. Xu, C., and Webb, W. W. (1996) *Journal of the Optical Society of America B-Optical Physics* **13**, 481-491

Chapter Two

Background and Experimental Procedures

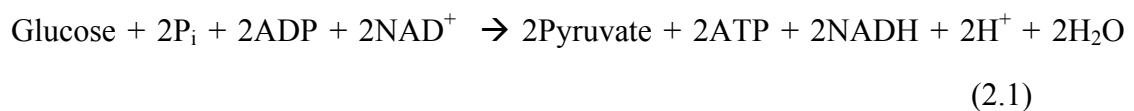
2.1 Overview of cellular energy metabolism

2.1.1 Pathways of NADH oxidation and reduction

The pathways of metabolism that are particularly relevant to our studies of NADH are those of the respiratory cycle or glucose/energy metabolism (1). Energy metabolism can be conveniently considered as four distinct sub-processes which either source or sink NADH and whose relative rates therefore determine the cellular concentration of NADH.

These four pathways, represented schematically in Fig.2.1, are:

1. Glycolysis (Yield: 2 NADH per molecule glucose)



This is a 10 step process catalyzed by 10 different enzymes. The sole enzyme that uses NAD^+ as a substrate is glyceraldehyde 3-phosphate dehydrogenase. The key control

enzyme in glycolysis is the allosteric enzyme phosphofructokinase (PFK) (1). The activity of PFK – and therefore the forward rate of glycolysis increases in response to ADP build up or low levels of ATP.

Glycolysis is not an efficient source of ATP however (net yield = 2 ATP), and is typically used only as a rapid but brief ATP supply. Glycolysis is a common path between anaerobic (non-oxidative) and aerobic (oxidative) metabolism. The end-product of glycolysis, pyruvate, is either channeled into mitochondria for aerobic metabolism or is converted in the cytosol to lactate for anaerobic metabolism.

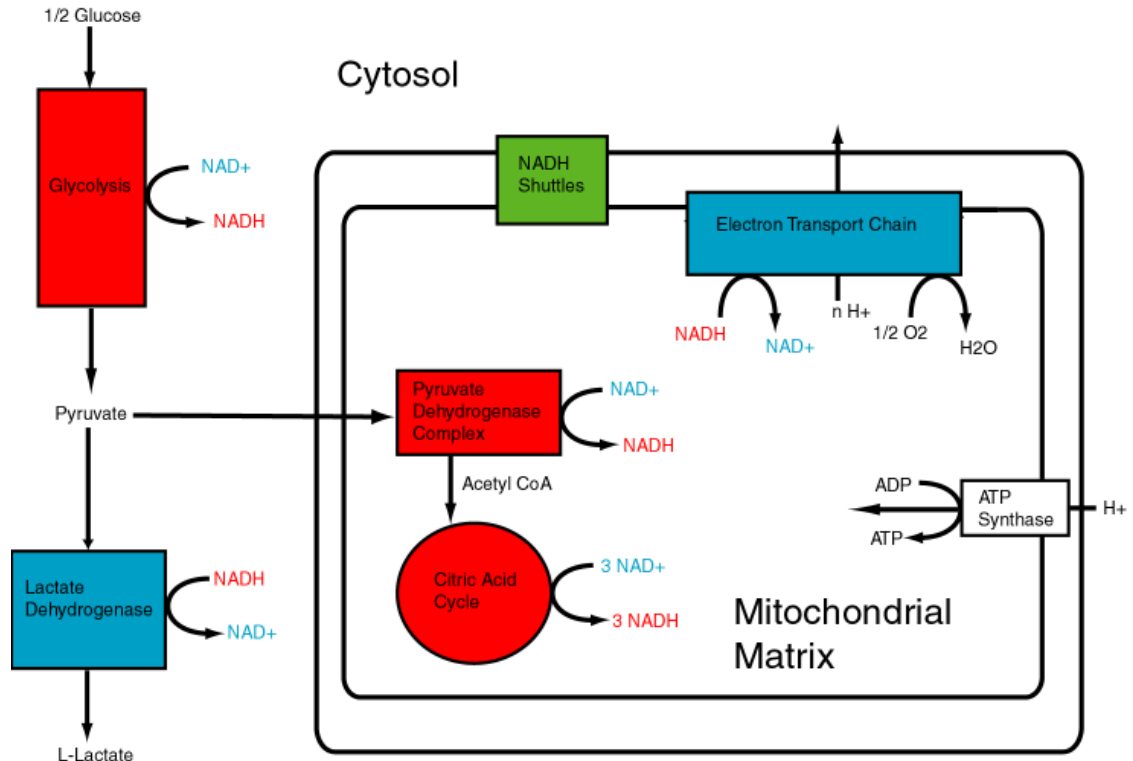
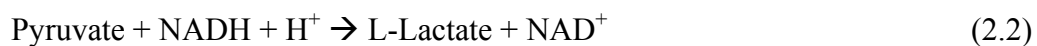


Figure 2.1 Cellular pathways of NADH oxidation and reduction.

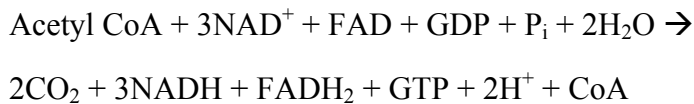
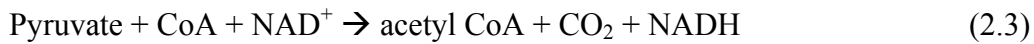
2. Lactate Production (Yield: -2 NADH per molecule glucose)



Lactate production together with glycolysis represents anaerobic respiration. This occurs when oxygen levels are low enough to impair the rate of the mitochondrial electron transport chain. This reaction is catalyzed by lactate dehydrogenase.

Various techniques have demonstrated that the cytosolic $[NADH]/[NAD^+]$ ratio is in equilibrium with the cytosolic and extracellular $[lactate]/[pyruvate]$ ratio (2-4). Thus changes in the cytosolic NADH fluorescence reflect changes in the intracellular $[lactate]/[pyruvate]$ ratio.

3. Pyruvate Dehydrogenase - Citric Acid Cycle (Kreb's Cycle) (Yield: 4 NADH per molecule glucose)



This oxidative decarboxylation of pyruvate is a critical step in metabolism. While pyruvate can be used by the cell for a number of other processes – once it has been converted into acetyl CoA, the only use for it is in the Citric Acid Cycle (Kreb's Cycle) and hence the cell is committed to aerobic respiration. The Kreb's cycle is the principle source of NADH in mitochondria. Kreb's cycle enzyme activities are regulated by effectors such as calcium (Ca^{2+}) influx during activity as a means of regulating mitochondrial metabolism (see Section (2.1.2)).

4. Oxidative Phosphorylation: The Electron Chain (ETC) and ATP Synthase (Yield: -2 NADH per molecule glucose)



The electron transport chain is a sequence of 4 enzyme complexes embedded in the mitochondrial inner membrane that transport a pair of electrons from NADH to O₂. The free energy liberated in this reaction is used by three of these enzyme complexes to pump protons out of the mitochondrial matrix into the cytosol.

The active transport of protons leads to the creation of a chemical and electrical gradient across the mitochondrial membrane and therefore to the creation of a chemical potential:

$$\Delta\mu = F\Delta\Psi - 2.3RT \cdot \Delta pH \quad (2.5)$$

Where $\Delta\Psi$ and ΔpH are the differences in electrical potential and pH across the membrane. Hence the free energy of NADH oxidation is transferred into the chemical potential of the electro-chemical gradient across the mitochondrial membrane. This free energy is then used to create ATP – by coupling the activity of ATP synthase to the flow of H⁺ ions back into the mitochondrial matrix.

2.1.2 Mitochondrial NADH level

Much of the work presented here will entail perturbing mitochondrial metabolism and monitoring the resulting change in NADH fluorescence. It is therefore useful to develop a qualitative, intuitive picture of the factors affecting mitochondrial NADH levels. This immediate discussion is not intended to be quantitative, as quantification will be introduced throughout the text as it becomes possible. The simple picture of mitochondrial metabolism is schematically depicted in Figure (2.2).

The NADH level in the mitochondrial matrix is determined by the balance of two reactions: the reduction NAD⁺ to NADH in the Krebs's cycle and the oxidation of NADH to NAD⁺ by the electron transport chain.

- $v_K = k_K[\text{NAD}^+]$ is the rate of reduction of NAD⁺ to NADH by the Krebs's cycle. The rate constant k_K is actually a collective term that is a function of the

activities and substrate levels of several of the Kreb's cycle enzymes (e.g. isocitrate dehydrogenase, α -ketoglutarate dehydrogenase, malate dehydrogenase). We define it only to separate the effect of the NAD^+ concentration from all other factors on the forward velocity of the Kreb's cycle. The 'rate constant' is only a constant for a given metabolic state – metabolic perturbations effect substrate levels and enzyme activities, thereby altering the value of this parameter.

- $v_E = k_E[\text{NADH}]$ is the rate of oxidation of NADH by the electron transport chain (ETC). The rate constant k_E is again a complex function of ETC enzyme activities, substrate levels, mitochondrial membrane potential, etc.

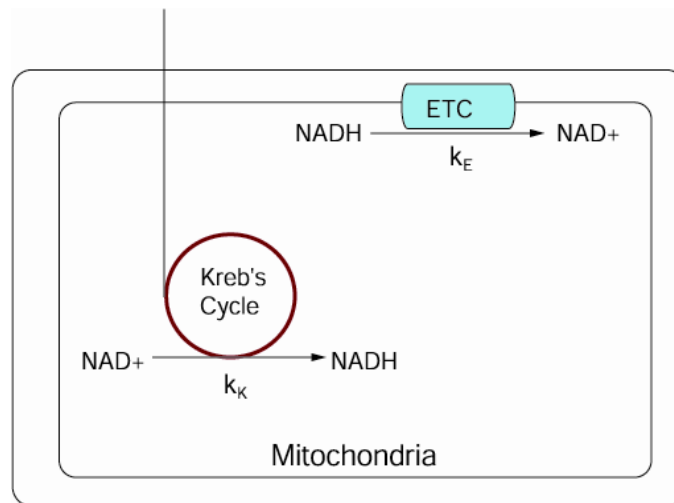


Figure 2.2 Regulation of mitochondrial $[\text{NADH}]/[\text{NAD}^+]$ level

In essence, the rate constants k_E and k_K represent the 'conductance' of their respective chemical pathways. To follow the analogy, the chemical concentration ($[X]$) corresponds to the driving 'potential' – and the reaction velocity is therefore the 'current'.

The two reactions, i.e. NADH source and sink, are treated here as irreversible reactions. This is a simplification made for the purpose of a qualitative understanding and is not strictly true. However, the standard free energy change $\Delta G^{0'}$ for the NADH oxidation by the ETC is so highly negative ((Eqn(2.4), -105.2 kcal/mol) (1) that the standard equilibrium constant K'_{eq} (from Eqn.(2.4)) is $\sim 2 \times 10^{77} \text{ M}^{-1}$. The high negative value of $\Delta G^{0'}$ is indicative of an irreversible reaction – likely receiving the dominant contribution to the free energy change from a decrease in entropy. The $\Delta G^{0'}$ for the net reaction of the Kreb's cycle is not quite so dramatically negative (-9.8 kcal/mol). Nonetheless, its K'_{eq} (from Eqn.(2.1)) is still $\sim 1.6 \times 10^7 \text{ M}^3$, indicating that while the reaction may be reversible, it is very forward biased and hence it is not a bad approximation to take the reaction as irreversible.

At a given steady state level of NADH, the source and sink velocities of NADH must be equal: $v_K = v_E$.

$$\Rightarrow k_K[NAD^+] = k_E[NADH]$$

$$\therefore \frac{[NADH]}{[NAD^+]} = \frac{k_K}{k_E} \quad (2.6)$$

Control of respiration by the cell itself or by external pharmacological agents is exerted by influencing the rate constants k_K and k_E . This can be done by modulating the activity of a particular enzyme (e.g. with Ca^{2+} or CN) or by affecting a substrate level (e.g. with hypoxia). It is the change in the rate constants that changes the $[NADH]/[NAD^+]$ level. This simplistic model expressed by Eqn.(2.6) can explain the effects of various drugs or metabolic processes on the mitochondrial NADH level. These effects are summarized in Table 2.1.

Cyanide (CN): CN competitively binds to the oxygen binding site on complex IV of the electron transport chain(5,6). This can be interpreted as effectively reducing the substrate (O_2) concentration available to the ETC, or reducing the activity of

complex 4 of the ETC. In either case, the rate constant k_E is reduced while the Krebs's cycle rate constant is not directly affected. This leads to an increase in $[NADH]/[NAD^+]$ by Eqn. (2.6).

Hypoxia: Reducing O_2 concentration has the same effect as introducing CN, i.e. ETC substrate limitation reduces the ETC rate constant k_E without a direct affect on the Krebs's cycle(7). This leads to an increase in $[NADH]/[NAD^+]$.

FCCP: FCCP (carbonylcyanide-p-trifluoromethoxyphenyl-hydrazone) is known as an uncoupler as it uncouples the oxidation of NADH from the production of ATP(8). FCCP is a weak lipophilic acid that transports protons across the mitochondrial membrane and thereby collapses its membrane potential. The collapse of the membrane potential enhances k_E without immediately affecting the Krebs's cycle. This leads to a decrease in $[NADH]/[NAD^+]$.

Table 2.1 Mechanisms of effectors of mitochondrial NADH

Effector	k_K	k_E	$[NADH] / [NAD^+] = k_K / k_E$
CN (inhibition)	Constant	↓	↑
Hypoxia (inhibition)	Constant	↓	↑
FCCP (uncoupling)	Constant	↑	↓
Ca²⁺ Influx (load)	↑	Constant	↑

Calcium Influx: Ca^{2+} is used by many cell types as a signaling molecule during enhanced metabolic load to upregulate mitochondrial activity by enhancing the

activity of three dehydrogenases in the Krebs'c cycle (for review, see (9-12). This increase in k_K with constant k_E increases the mitochondrial $[NADH]/[NAD^+]$ (8). The elevated mitochondrial NADH then increases flux through the ETC and thereby increases ATP production. There has been some evidence recently however that the NADH response in neurons responding to elevated activity is not Ca^{2+} dependent (13) – leaving the precise mechanism of the upregulation of mitochondrial metabolism in response to elevated demand somewhat uncertain.

Even with a simple model of mitochondrial metabolism, we can already see the essential features of the NADH response to effectors emerge. It is noteworthy that both uncouplers (e.g. FCCP) and elevated metabolic load (Ca^{2+} influx) increase the ETC velocity (v_E) and therefore the O_2 consumption rate. However, they produce opposite effects on the NADH level – uncouplers like FCCP reduce $[NADH]$, while elevated Ca^{2+} causes an increase in $[NADH]$. This apparent disparity is readily explained by the differential effects of these molecules on the Krebs's cycle and the ETC.

Models of mitochondrial or neuronal metabolism, as have been developed by several theorists (7,11,14,15), are complex and take into account the pathways associated with glycolysis, lactate dehydrogenase, mitochondrial membrane shuttles, the phosphocreatine buffer system, Ca^{2+} regulation, NADH-NADPH transhydrogenase, etc. However under normal conditions, many of these pathways yield only second order effects on the NADH level in cells – and consideration of only a relatively small number of NADH influencing pathways (in this case 2) is sufficient to gain a qualitative understanding of NADH effectors.

2.2 Two-photon fluorescence microscopy

Microscopy was done on either an upright or an inverted two-photon microscope, both schematically represented in Fig. (2.3). The particular microscope was selected based on the application. Inverted microscopes use coverslip corrected objectives that have numerical apertures (NA) as high as 1.3. The high NA yields better spatial resolution, and excitation and collection efficiencies. However they have small working distances ($\sim 200\mu\text{m}$) and require a coverslip between the objective and the sample. These microscopes are well-suited for imaging cell cultures in which cells naturally form a thin ($<20\mu\text{m}$) layer on a coverslip. They can also be used in experiments on brain slices where no direct access to the imaging plane is required by other hardware such as electrophysiology electrodes.

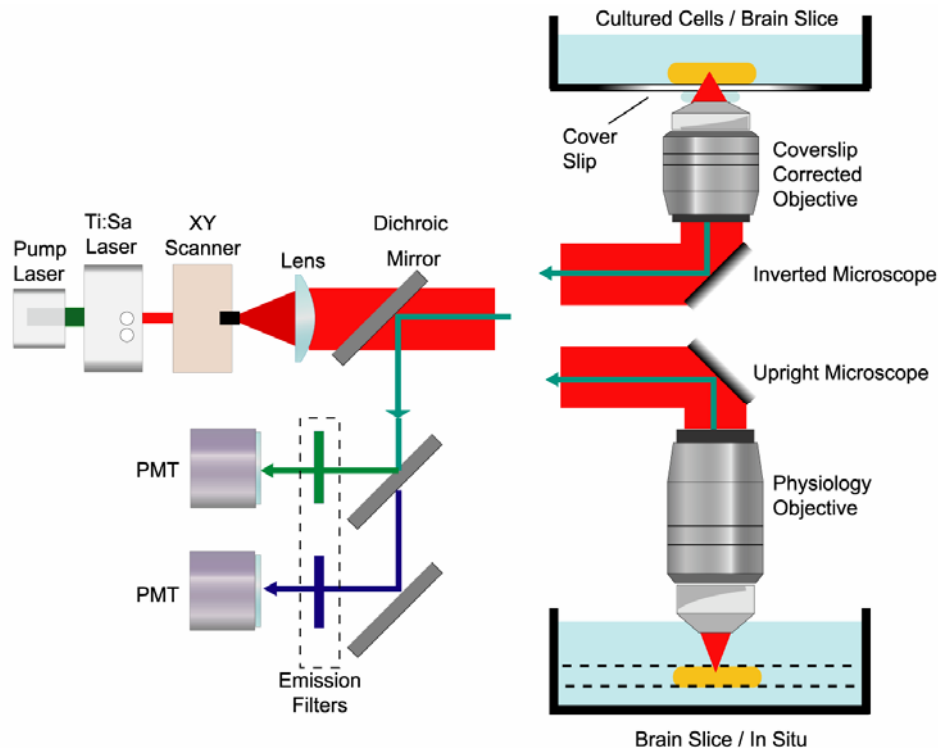


Figure 2.3 Generic two-photon laser scanning microscope

In contrast, upright microscopes use physiology objectives – i.e. objectives with large working distances (<3.3mm) designed to be immersed in water with no cover slip between the objective and the sample. These objectives compromise NA (<1), but due to their large working distance, are ideal for experiments in which hardware access is required to the imaging plane (e.g. electrophysiology) or using a cover slip is not possible (e.g. *in situ* brain imaging). More recently – Olympus has developed a series of objectives to be used with upright microscopes that have large working distances, high NA (0.95) and are available in both a coverslip corrected version and a physiology version.

For high-resolution imaging of cultured neurons, a Zeiss F-Fluar, 40x NA 1.3, oil immersion objective was used. For brain slice imaging on the inverted microscope, the Zeiss C-Apochromat 10x NA 0.45 Water and the Olympus U-Apo/340 40x NA 1.15 Water were used. For slice imaging in the upright microscope, the objectives used were either an Olympus LUMPlanFl 40x NA 0.8 water immersion or an Olympus 20x 0.95 water immersion. Slice imaging in the small volume, airtight chamber required long working distance and cover slip correction - hence a Zeiss C-Apochromat 10x NA 0.45 Water or an Olympus 20x 0.95 coverslip corrected physiology objective were used.

The inverted microscope was a Zeiss Axiovert 135TV mounted with a Biorad MRC1024 multi-photon imaging system. The upright microscope was an Olympus BX50WI mounted with a Biorad MRC600 multi-photon imaging system. A solid state pumped Ti:Sapphire pulse laser (Spectra Physics Millennia-Tsunami combination) provided the excitation at 737 nm with a pulse-width of ~100 fs and a repetition rate of 80 MHz. The 2P-fluorescence was filtered from the excitation beam using a 670 nm long pass dichroic mirror (Chroma). Appropriate filters were chosen to detect the wavelength range 350-500 nm for the intrinsic fluorescence. The fluorescence was

detected by photomultiplier tubes (350-500nm: Hamamatsu HC125-02, 510-650nm: Hamamatsu HC125-01). Images (512x512 pixels) were typically acquired within ~1 second.

2.3 Steady State (Wavelength Resolved) Fluorescence Spectroscopy

2.3.1 Solution steady state fluorescence spectroscopy

One-photon excited wavelength resolved steady state spectra of aqueous solutions were measured in commercial instruments. The samples were held in 3x3 mm quartz cells (Starna Cells Inc.). Absorption spectra (2 nm resolution) were measured with a single beam diode array spectrophotometer (8451A, Hewlett Packard). Fluorescence emission spectra were recorded using a PTI-QM-1 fluorimeter (Photon Technology Int.) with 1 nm resolution. NADH (Sigma) samples were dissolved in either PBS (pH 7.4) or in HPLC water buffered with Trizma Hydrochloride (Sigma) at pH 7.4. Unless otherwise specified, NADH fluorescence spectra were measured at 340 nm excitation and excitation spectra were measured at 460 nm detection.

To characterize the effect of enzyme binding on NADH fluorescence, NADH (10 μ M) was titrated with 0-50 μ M mitochondrial malate dehydrogenase (mMDH, Roche Applied Science) in water buffered with Trizma Hydrochloride (pH 7.0). The fluorescence was normalized to the signal from unbound NADH. Assuming a simple reversible binding reaction, the dissociation constant (K_d) was calculated from the measured NADH fluorescence signal F as a function of mMDH concentration using $F = (1 + \Phi[mMDH]/K_d) / (1 + [mMDH]/K_d)$. The factor Φ is the fluorescence enhancement upon binding to mMDH.

2.3.2 *In vivo* fluorescence spectroscopy: scanning stage technique

Time or wavelength resolved fluorescence spectra of the cellular intrinsic fluorescence were acquired on a modified inverted microscope, described in detail below (Fig. (2.4)), using a scanning stage technique. In order to maximize fluorescence collection efficiency, the excitation beam was maintained stationary with respect to the microscope and the sample was scanned using a computer controlled x-y stage (SCAN IM, Merzhäuser). This ensured that the collected fluorescence was also stationary with respect to the microscope and could therefore be easily coupled to an optical fiber (for wavelength resolved spectroscopy) or focused on to a small surface area ($<1\text{cm}^2$) fluorescence lifetime detector.

The sample stage was scanned in such a way as to effectively raster scan the excitation beam in a $100\times 100\ \mu\text{m}$ square in the stratum radiatum or in a $100\times 50\ \mu\text{m}$ rectangle in the stratum pyramidale. This stage scanning was not done to spatially map the fluorescence, but rather, simply to distribute the two-photon excitation dose over an area of tissue $\sim 10^4$ times larger than the area of the focused beam. This enabled long integration times of the collected fluorescence without damaging the tissue. All spectra were acquired from 70-100 μm within the slice.

2.3.3 *In vivo* fluorescence spectroscopy: wavelength resolved spectroscopy

Fluorescence was excited in the sample using the scanning stage technique described above. The collected fluorescence was coupled to 550 μm multimode fiber with high transmission in the UV and visible wavelengths (Oz Optics) and then imaged onto the entrance slit of a spectrometer (270M, SPEX) equipped with a liquid nitrogen cooled CCD camera. An image of the sample was first recorded and the intracellular region of interest was selected. The acquisition of a cellular spectrum required a dwell time of about $30\ \text{ms}/\mu\text{m}^2$ using an average excitation power of ~ 15

mW (cultured cells) or ~20 mW (brain slices) measured after the objective at 737 nm. This dwell time is substantially greater than the $\sim 1 \mu\text{s}/\mu\text{m}^2$ dwell time characteristic of laser scanning microscopy, which raises concerns of photodamage to the cells. However, no morphological photodamage or fluorescence changes were observed during the acquisition time.

The spectral response of both the two-photon microscope and the spectrometer, combined, were calibrated using an Oriel Quartz Tungsten Halogen 63358 calibration lamp or alternatively by using solutions such as fluorescein or aqueous NADH whose emission spectra were measured on the commercial fluorimeter specified above for measuring fluorescence in aqueous solutions. The wavelength calibration of the system was carried out using lines from a calibration standard mercury lamp (Ocean Optics HG-1).

2.4 Time-resolved fluorescence spectroscopy

2.4.1 Definition of Fluorescence and Anisotropy Decay

The fluorescence emitted by a sample is the vector sum of parallel ($I_{\parallel}(t)$) and perpendicular ($I_{\perp}(t)$) polarization components. These orthogonal directions are defined with respect to the polarization of the excitation light. In the experiments described throughout this work, these two fluorescence components are typically measured sequentially, rotating an analyzer before the photo-detector and integrating the fluorescence signal for equal times. Having measured these two fluorescence decay curves, we can calculate the total fluorescence decay curve ($I_{\text{tot}}(t)$, also known as the magic angle fluorescence decay) and the rotational anisotropy decay curve ($r(t)$), defined by equations (2.7) and (2.8) respectively.

$$I_{\text{tot}}(t) = I_{\parallel}(t) + 2GI_{\perp}(t) \quad (2.7)$$

$$r(t) = \frac{I_{\parallel}(t) - GI_{\perp}(t)}{I_{\parallel}(t) + 2GI_{\perp}(t)} \quad (2.8)$$

Here, G , known simply as the G factor, is the degree to which the optical detection path preferentially transmits one polarization over the other. The total fluorescence decay is a measure of the population of the excited state. The anisotropy of the fluorescence is the degree to which molecular orientation polarizes the emitted fluorescence. The anisotropy is initially non-zero because the excitation beam polarization selectively excites a particular orientation of molecules. The value of the initial anisotropy depends on the angle between the excitation and emission dipoles. The decay of the anisotropy measures the decay of the net molecular orientation due to rotational diffusive motion (see Section (2.4.4)). The characteristic decay time, known as the rotational diffusion time, characterizes the timescale of this diffusive motion.

2.4.2 Experimental Set-Up

Fluorescence was excited in the sample using the scanning stage technique described earlier. The fluorescence decay of NADH in solution or in tissue was measured using time-correlated single photon counting on a modified inverted Zeiss IM-35 microscope as shown in Fig. (2.4)(16). The 740nm, ~100fs laser pulses (80 MHz repetition rate) were pulse picked down to 10Mhz with a Pockel Cell (Conoptics, Danbury, CT). The beam was then directed through the light-inlet port the microscope. A small fraction (~1%) of the beam was split off by a coverslip (CS) and focused onto a photodiode (PD) to provide a trigger signal for the time resolved acquisition electronics. The epi-fluorescence from the sample was filtered from the excitation light using a dichroic mirror (M1) and an emission filter (F). The polarization component of the fluorescence was selected using a Glan-Thompson prism (P) mounted at the top-exit port of the microscope before being detected using a

microchannel plate photomultiplier (MCP) (Hamamatsu MCP-PMT R3809U-50). The total fluorescence decay is measured using magic angle (54.7°) polarization, while anisotropy measurements entail separately and sequentially measuring the parallel and perpendicular component fluorescence decays as described above.

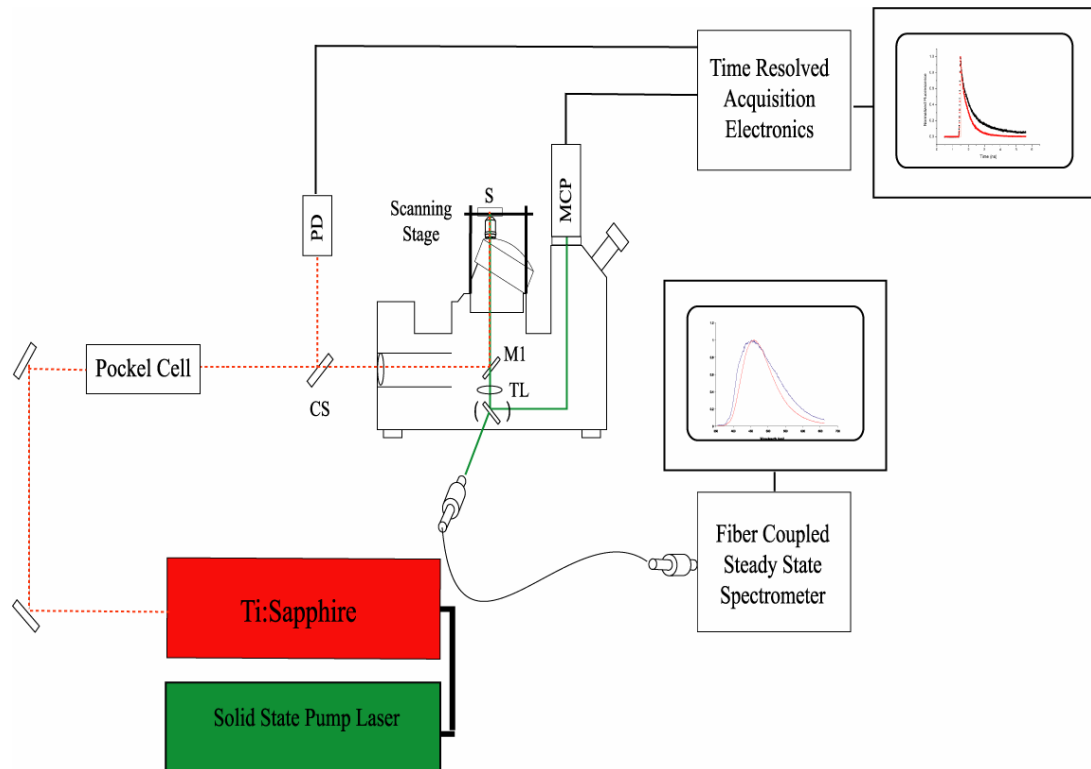


Figure 2.4 Two-photon scanning stage spectroscopy apparatus

Under our experimental conditions, the optical depolarization due to the microscope objective (40x, 1.15 NA, with an underfilled back aperture) was negligible (17).

2.4.3 Functional form of fluorescence decay

The total fluorescence decay was calculated from the recorded parallel and perpendicular fluorescence decays according to Eqn.(2.7). The total fluorescence decay ($I_{\text{tot}}(t)$) was then fit using either the commercial Becker & Hickl SPCImage 2.4 fitting program, or custom written fitting routines in Matlab. These programs utilize non-linear least-squares fitting algorithms to fit the fluorescence decay with the functional form:

$$I(t) = \left(I_{\text{baseline}} + I_0 \left(a_0 \delta(t-t_0) + \sum_{i=1}^n a_i \cdot \exp(-(t-t_0)/\tau_i) \right) \right) \otimes R(t) \quad (2.9)$$

Terms in Fitting Equation:

1. Decay kinetics: The sum of exponential terms in this expression represents the excited state dynamics of the fluorescence. Each individual exponential term ($a_i \exp(-t/\tau_i)$) represents the decay of the excited state via a particular pathway. These different pathways can be associated with different fluorophores, different conformations of a fluorophore, or simply different excited to ground state transitions in a fluorophore. For the purpose of general discussion, we will simply refer to the physical sources of these exponential decay components as species, since a more precise physical identification is case-specific. The amplitude (a_i) of an individual decay component is equal to the fractional population of the species associated with it. Hence it follows that the sum of the fractional populations must be unity ($\sum_{i=1}^n a_i = 1$). The lifetime of a decay component is equal to the inverse of the total rate of transition from the excited state to the ground state, i.e.

$$\tau = \frac{1}{k_r + k_{nr}} \quad (2.10)$$

Where k_r is the radiative rate – the rate of relaxation from the excited to the ground state involving the emission of a fluorescence photon - and k_{nr} is the total non-radiative rate, the net rate of transition to the ground state not involving the emission of a fluorescence photon. The fluorescence quantum yield is by definition the fraction of those transitions back to the ground state which involve emitting a fluorescence photon.

$$\phi_f = \frac{k_r}{k_r + k_{nr}} = k_r \tau \quad (2.11)$$

2. Scattered excitation light: The delta function term ($a_0 \delta(t - t_0)$) in Eqn.(2.9) represents backscattered excitation light. Since the excitation pulse is ~ 100 fs in duration, the backscattered light will also be comparable in duration, with some temporal stretching due to the variability in pathlength of backscattered photons reaching the detector. The duration of this backscattered pulse is far below the temporal resolution of our detector (~ 10 ps) and hence we can approximate it with a delta function. While this term can be excluded for measurements in solution, it is necessary in highly scattering tissue such as brain slices.

3. Amplitudes and Offsets: I_{baseline} in Eqn.(2.9) is the baseline or background signal, approximated as constant for all times. This background is largely from ambient light (e.g. computer monitors), and not from fluorescence. While other fluorophores are present in brain tissue, we will show in Section (3.1) that under our excitation and emission filtering conditions, only NADH and NADPH are significantly detected. I_0 is the peak fluorescence at time t_0 , where t_0 is the temporal offset of the fluorescence decay from the start of the acquisition window.

4. Response function: $R(t)$ is the measured temporal response function of the system, recorded using second harmonic generation from crystals of KDP* or rat tail collagen. This response function is convolved ($f(t) \otimes R(t) = \int_{-\infty}^{\infty} R(t')f(t-t')dt'$) with the guess fit function and then compared to the observed decay.

Derived Quantities

Once the total intensity decay fit parameters have been obtained by the fitting program, we can calculate a number of useful derived quantities:

1. The average lifetime $\langle \tau \rangle$ of the fluorescence.

$$\langle \tau \rangle = \frac{\sum_{i=1}^n a_i \tau_i}{\sum_{i=1}^n a_i} \quad (2.12)$$

2. The fraction of the total fluorescence generated by species 'i' is f_i .

$$f_i = \frac{a_i \tau_i}{\sum_{j=1}^n a_j \tau_j} \quad (2.13)$$

3. The change in the concentration of species 'i' upon hypoxia.

$$\frac{C_{i,hypoxia}}{C_{i,normoxia}} = \frac{a_{i,hypoxia}}{a_{i,normoxia}} \frac{I_{0,hypoxia}}{I_{0,normoxia}}$$

$$\Delta C_i = \frac{C_{i,hypoxia} - C_{i,normoxia}}{C_{i,normoxia}} = \frac{C_{i,hypoxia}}{C_{i,normoxia}} - 1 \quad (2.14)$$

2.4.4 Functional form of fluorescence anisotropy decay

The fluorescence anisotropy decay of a freely rotating molecule in an isotropic environment is usually described adequately by a single exponential:

$$r(t) = r_0 \exp(-t/\theta) \quad (2.15)$$

Where θ is the rotational diffusion time of the molecule and r_0 is the initial anisotropy. The anisotropy decays of many conventional fluorophores (e.g. fluorescein, coumarin) as well as NADH in solution or NADH fully bound to malate dehydrogenase in solution were found to follow this functional form. The initial anisotropy (r_0) is solely a property of the fluorophore itself, and is related to the angle between the absorption and emission dipoles (δ) by Eqn.(2.16).

$$r_0 = \frac{2\alpha}{2\alpha + 3} \left(\frac{3 \cos^2 \delta - 1}{2} \right). \quad (2.16)$$

Based on the number of photons absorbed (α), the maximum theoretical r_0 -values are 0.4 and 0.57 for 1-photon and 2-photon events respectively (corresponding to collinear dipoles, without depolarizing processes, i.e. $\delta = 0$).

The rotational diffusion time on the other hand, depends not only upon the fluorophore molecule itself, but also upon environmental conditions. This dependence may be summarized by the Stokes-Einstein equation (Eqn.(2.17)).

$$\theta = \frac{1}{6D_{rot}} = \frac{\eta V}{kT} \quad (2.17)$$

Where D_{rot} is the rotational diffusion coefficient, V is the hydrodynamic volume of the molecule, η is the local viscosity of the environment and T is the absolute temperature. This relation approximates the hydrodynamic volume (molecule + hydrodynamic shell) of the molecule to be spherical, which is a reasonable approximation for NADH (18). We use the Stokes-Einstein relation later to estimate the viscosity of the intracellular environment.

While a single exponential anisotropy decay approximates the decay of a free fluorophore, more complicated decays are also possible under certain circumstances.

Of particular relevance here, associated anisotropy is the form of fluorescence anisotropy arising from a mixture of fluorophore species – each fluorophore species having its own distinct fluorescence decay and fluorescence anisotropy decay. The fluorescence anisotropy decay from the mixture is the average of the fluorescence anisotropy decays of the individual species, weighted by their respective fluorescence decays. Fitting the anisotropy decay with the associated anisotropy model associates a distinct rotational diffusion time with each lifetime decay component as described by Eqn.(2.18) (19,20).

$$r(t) = \frac{\sum_{i=1}^n a_i \exp(-t / \tau_i) r_{0i} \exp(-t / \theta_i)}{\sum_{i=1}^n a_i \exp(-t / \tau_i)} \quad (2.18)$$

Where each species ‘i’ has its own set of total intensity decay parameters (a_i , τ_i) and set of anisotropy decay parameters (r_{0i} , θ_i).

2.4.5 Fitting protocol

The analysis of anisotropy decay curves is somewhat more difficult than a simple non-linear least squares fit provided by most commercial data analysis software. Hence, it was necessary to write custom programs to do these fits. The fitting protocol employed during this analysis is a form of global analysis specifically modified for analyzing associated anisotropy decays.

Recall that the actual measured fluorescence decays are the parallel ($I_{\parallel}(t)$) and perpendicular ($I_{\perp}(t)$) polarization components of the fluorescence decay. From these one can calculate the anisotropy decay curve using Eqn.(2.19).

$$r(t) = \frac{I_{\parallel}(t) - GI_{\perp}(t)}{I_{\parallel}(t) + 2GI_{\perp}(t)} = \frac{\sum_{i=1}^n a_i \exp(-t/\tau_i) r_{0i} \exp(-t/\theta_i)}{\sum_{i=1}^n a_i \exp(-t/\tau_i)} \quad (2.19)$$

In practice however, we do not actually calculate $r(t)$, but rather we calculate the numerator and denominator separately. By convention, the numerator is called the difference curve ($D(t)$) and the denominator is called the sum curve ($S(t)$), simply reflecting the operation between the parallel and perpendicular fluorescence components. Both the sum and difference curves are sums of exponentials. Furthermore, in practice, the functional form of each is more complicated than a simple sum of exponential terms. The most general form of both the sum and difference curves is analogous to Eqn(2.9), that is, there are terms to account for baseline, scattered light, temporal offset and detector response.

$$\begin{aligned} S(t) &= I_{\parallel}(t) + 2GI_{\perp}(t) \\ &= \left(I_{baseline,S} + I_{0,S} \left(a_{0,S} \delta(t-t_0) + \sum_{i=1}^n a_i \cdot \exp(-(t-t_0)/\tau_i) \right) \right) \otimes R(t) \end{aligned} \quad (2.20)$$

$$\begin{aligned} D(t) &= I_{\parallel}(t) - GI_{\perp}(t) \\ &= \left(I_{baseline,D} + I_{0,D} \left(a_{0,D} \delta(t-t_0) + \sum_{i=1}^n r_{0i} \cdot \exp(-(t-t_0)/\theta_i) \cdot a_i \cdot \exp(-(t-t_0)/\tau_i) \right) \right) \otimes R(t) \end{aligned} \quad (2.21)$$

To fit these individually with a minimization algorithm, we must define a reduced χ^2 for both these curves.

$$\begin{aligned}
S(t) &= I_{\parallel}(t) + 2GI_{\perp}(t) \\
\sigma_S^2(t) &= I_{\parallel}(t) + 4G^2I_{\perp}(t) \\
\chi_S^2 &= \frac{1}{n - p_S} \sum_{i=1}^n \frac{1}{\sigma_S^2(t_i)} (S(t_i) - S_{fit}(t_i))^2
\end{aligned} \tag{2.22}$$

Where n is the number of data points in the curve, p_S is the number of fitting parameters and S_{fit} is the trial fitting function. An analogous definition can be made for the difference curve $D(t)$, but with a slightly different weighting factor.

$$\begin{aligned}
D(t) &= I_{\parallel}(t) - GI_{\perp}(t) \\
\sigma_D^2(t) &= I_{\parallel}(t) + G^2I_{\perp}(t) \\
\chi_D^2 &= \frac{1}{n - p_D} \sum_{i=1}^n \frac{1}{\sigma_D^2(t_i)} (D(t_i) - D_{fit}(t_i))^2
\end{aligned} \tag{2.23}$$

In order to facilitate the fit, we reduce the number of floating parameters in the functional form of the fitting function. Specifically, in Eqns.(2.20) and (2.21), the baseline intensities ($I_{baseline,S}$, $I_{baseline,D}$), the peak intensities ($I_{0,S}$, $I_{0,D}$) and the temporal offset (t_0) can be calculated trivially from the curves themselves and set as constants while executing the fitting routine.

Furthermore, by examining the functional form of the sum and difference decays (Eqn.(2.20) and (2.21)) we see that there are a set of parameters that the sum and difference curves share in common, namely the amplitudes and time constants of the total fluorescence decay, i.e. the (a_i, τ_i) . Only the parameters characterizing the anisotropy decay (r_{0i}, θ_i) are specific to the difference decay. The parameters that are shared between the sum and difference decays are known as global parameters. The existence of global parameters enables us to employ a fitting protocol known as global analysis (21,22). This technique fits two or more curves simultaneously that have a set of shared parameters and sets of parameters identified with individual curves. A

measure of global goodness of fit must then be defined, known as the global chi-squared (Eqn.(2.24)).

$$\chi_{global}^2 = \frac{1}{2n - (p_S + p_D - p_{global})} \left[\sum_{i=1}^n \frac{1}{\sigma_S^2} (S(t_i) - S_{fit}(t_i))^2 + \sum_{i=1}^n \frac{1}{\sigma_D^2} (D(t_i) - D_{fit}(t_i))^2 \right] \quad (2.24)$$

Where p_{global} is the number of global parameters. The fitting protocol is schematically represented in Fig.(2.5).

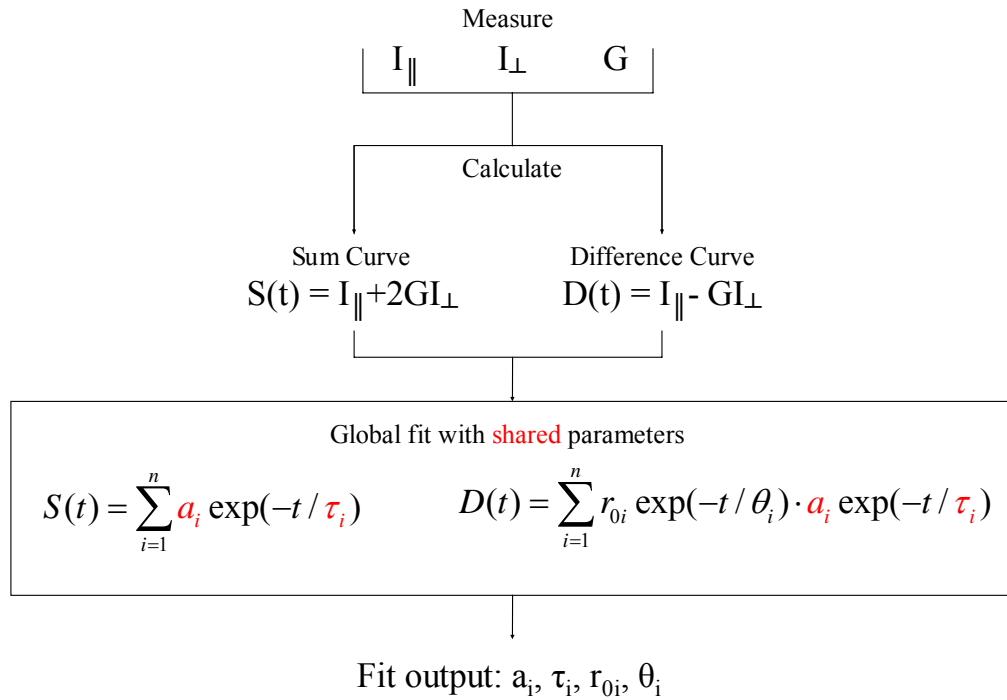


Figure 2.5 Anisotropy and lifetime global analysis fitting algorithm. Simultaneous fitting of sum and difference curves allows the simultaneous extraction of lifetime and anisotropy parameters that.

Thus, by performing a global fit, we can simultaneously fit $S(t)$ and $D(t)$ and automatically satisfy the constraint that certain shared parameters must have the same

values in both fits. The global fit then provides us with both the total intensity decay parameters (a_i, τ_i) and the anisotropy decay parameters (r_{0i}, θ_i) in a single minimization operation with an improved resolution on the shared parameters.

2.4.6 G factor determination

The G factor describes the extent to which the detection system is preferentially sensitive to one polarization over the other due, e.g, to polarization sensitivity in the transmittance/reflectivity of the detection optics. The G factor is measured by using a technique called ‘tail matching’ (23). A calibration dye is selected whose fluorescence lifetime (τ) is significantly longer than its rotational diffusion time (θ) and whose emission wavelength is similar to the samples that are being measured. Fluorescence emitted at times much greater than the rotational diffusion time is fully depolarized as any net orientation of excited molecules has decayed away. The ratio of the parallel and perpendicular fluorescence components at these long times then gives the relative sensitivity of the detection system to parallel and perpendicular light.

Intrinsic fluorescence has an emission peak in the range of 440-460nm and so we choose coumarin, which has an emission peak at 440nm, as our calibration dye. Coumarin has a fluorescence lifetime (~ 2.2 ns) (Fig.2.6a) which is significantly longer than its rotational diffusion time (~ 120 ps) (Fig.2.6b), hence a significant amount of fluorescence is emitted by the fluorophore that is depolarized.

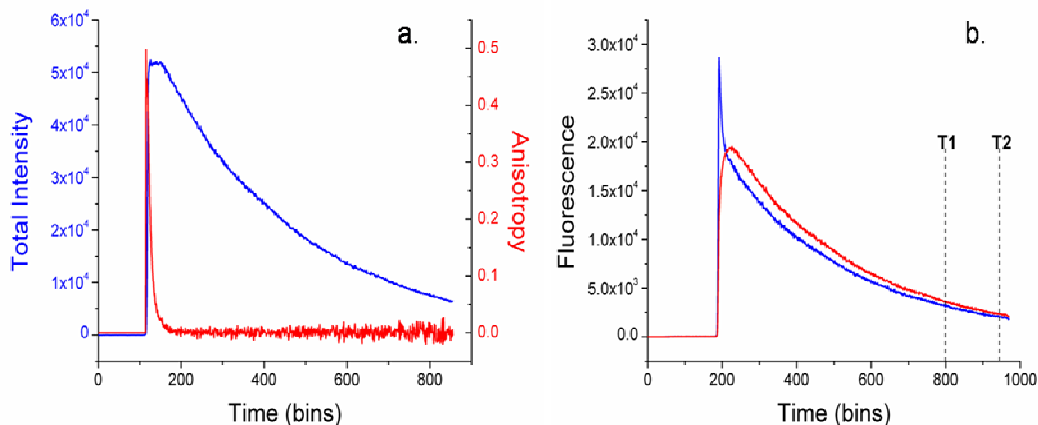


Figure 2.6. G Factor determination using coumarin as a fluorescence standard. (a) Coumarin total fluorescence intensity decay (blue) and rotational anisotropy decay (red). (b) Parallel component (blue) and perpendicular component (red) of the total fluorescence decay. The time range taken for tail matching is indicated by T1 and T2.

The parallel and perpendicular fluorescence decay components are recorded (Fig.2.6 c and d) and a time window (T1 \rightarrow T2) is selected near the end (tail) of the fluorescence decay over which the G factor is then calculated according to Eqn.(2.25). While the G factor is measured for each data measurement run, the typical value of the G factor ranges between 0.8 and 1.1.

$$G = \frac{\int_{T1}^{T2} I_{\parallel}(t) dt}{\int_{T1}^{T2} I_{\perp}(t) dt} \quad T2 > T1 > \tau \gg \theta \quad (2.25)$$

2.4.7 Number of decay components

The number of exponential decay components used in a fit of lifetime decay is an area of some contention. If an *a priori* knowledge of the excited state dynamics gives reason to expect a specific number of decay components, then one can fix the

number of components. Often however, as in the case of tissue, there is no reason to expect a specific number of components. In such a case, the rule of thumb is to fit the decay with the minimum number of components that provides a good χ^2 ($\chi^2 < 1.3$ (23)) and only marginal improvement in χ^2 (< 0.2 (23)) with an additional fit component. Additionally, we can also use the residuals and the autocorrelation of the residuals to determine goodness of fit – both should appear as random fluctuations about 0 for a good fit.

2.5 The hippocampal brain slice

The hippocampal slice has served for many years as a model *ex vivo* system for a variety of studies on activity dependent and metabolic phenomena. The well defined neural circuits make the hippocampus a convenient system for studying activity dependent phenomena. Furthermore, the susceptibility of the hippocampus to neurological diseases linked with dysfunctional energy metabolism provides further motivation for their study in *ex vivo* preparations of this system.

2.5.1 Hippocampal slice architecture

The transverse hippocampal slice has a well defined structure (Fig. 2.7) consisting of three distinct cell layers, known as the CA1, CA3 and the dentate gyrus (DG). The cell bodies of these layers are indicated by the dashed white line. There are two axonal bundles (red): the mossy fibers which originate from the DG and synapse on the dendrites (yellow) of the CA3 layer, and the Schaeffer collaterals which connect the CA3 to the CA1 layer.

In our experiments utilizing electrophysiology on transverse hippocampal slices, stimulation across the Schaeffer collaterals provides a convenient spatial separation ($\sim 1\text{mm}$) between the site of stimulation and that of the consequent synaptic

activity. This separation can be particularly valuable in optical recording of activity associated NADH fluorescence changes, where the stimulation electrode can be placed entirely outside the field of view.

Most of the metabolic imaging presented here is done in the CA1 layer. The CA1 and CA3 layer in turn have multiple regions or strata. The stratum oriens (SO) consists of axons that leave the cell layer to form synapses with other cell layers. CA3 axons synapse with CA1 dendrites and CA1 axons leave the hippocampus entirely. The stratum pyramidale (SP) is a layer of neuronal cell bodies. The stratum radiatum (SR) and stratum lacunosum-moleculare (SLM) consist of axo-dendritic network with numerous synapses and scattered astrocytes. In the CA3, there is an additional layer, not obvious in Fig.(2.7) known as the stratum lucidum (SL) which consists of both dendrites and the mossy fibers entering the CA3 region.

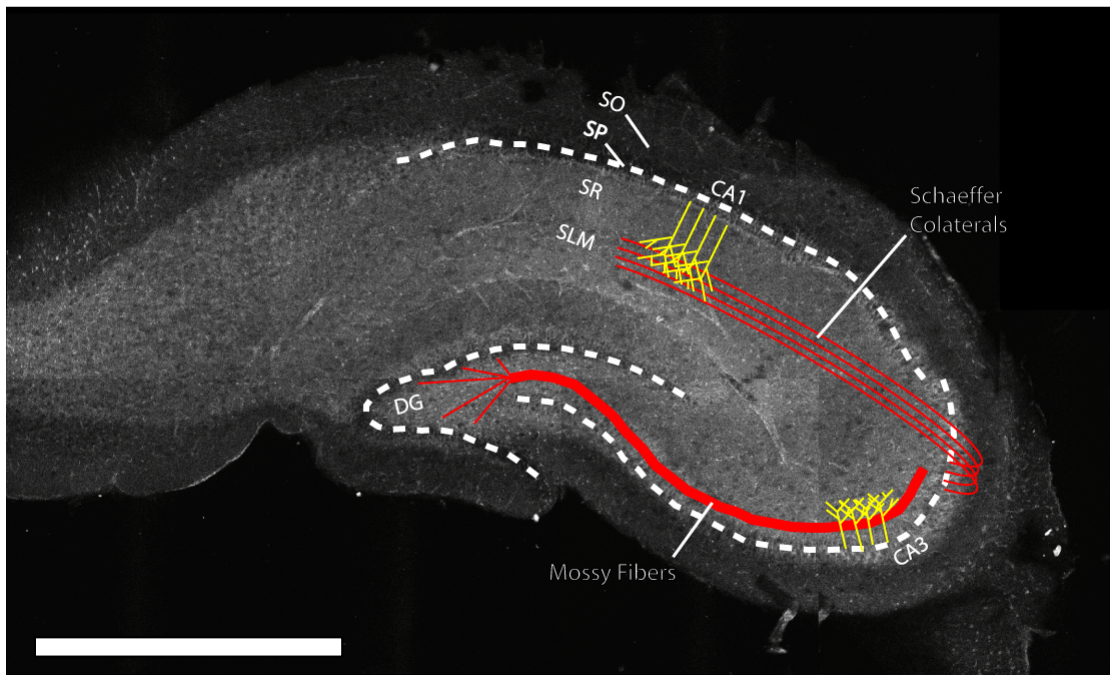


Figure 2.7 Architecture of the hippocampal slice. Scale bar is 1mm.

2.5.2 Sample Preparation

2.5.2.1 Primary dissociated neuronal cultures

The hippocampi from neonate Sprague-Dawley rat pups were dissected in ice-cold dissection buffer and removed and transferred into warmed (37 °C) Papain solution kept at 95% O₂ and 5% CO₂. The hippocampi were cut into thin slices and digested for 60 to 75 minutes by adding Papain enzyme. After digestion cells were washed, centrifuged, counted and diluted, dropped into appropriate dishes and placed in an incubator. The cells were cultured in phenol-red free growth media (Neurobasal A media, Gibco BRL). The media exhibited a significant (40% intensity of the intrinsic fluorescence in neurons) and broad fluorescence from 450 to 570 nm. On the first day ARA-C (5 μm) was applied to suppress cell division. From then on cells were fed twice a week by replacing half the media. The cells were grown on special dishes for imaging through a cover slip (Glass No. 1.5, thickness 0.17 mm, MatTek Corp.). For imaging the Neurobasal A media was replaced by Tyrode's buffer (NaCl 135 mM, KCl 5 mM, MgCl₂ 1 mM, CaCl₂ 1.8 mM, Hepes 20 mM, BSA 0.5% ,and Glucose 10 mM). The temperature of the culture dishes under the microscope was kept at 36°C by using an objective heater (Bioptechs Inc.) and heating the perfusate. For colocalization studies, the cells were stained with rhodamine123 100 nM (Molecular Probes) for 30 min.

2.5.2.2 Acute Hippocampal Slices

Transverse hippocampal slices were prepared from Sprague-Dawley rats (day 14 to day 20) using a McIlwain tissue chopper or a Cambridge Vibratome according to the protocol described by Wang & Kass (24). The slices were incubated in artificial cerebrospinal fluid (ACSF) for 30 min to 1 h in a static bath chamber prior to imaging. The ingredients used for ACSF are NaCl 118 mM, KCl 3.0 mM, KH₂PO₄ 1.0 mM,

MgSO₄ 1.0 mM, Glucose 20 mM, CaCl₂ 1.5 mM and NaHCO₃ 25 mM. Normoxic ACSF was oxygenated by constantly bubbling it with a gas mixture containing 95% O₂ and 5% CO₂. Hypoxic ACSF was similarly deoxygenated with a gas mixture containing 95% N₂ and 5% CO₂. ACSF solutions were kept in a static water bath at 35°C from which they could be perfused into the slice chamber.

Slices were transferred into one of two tissue perfusion chambers depending upon the experiment to be performed (see below). The temperature in the chamber was controlled by a feed-back loop and maintained at 32-34 °C. A solution Heater SH-27A (Warner Instruments Inc.) was used to warm ACSF as it flowed to the chamber. For colocalization studies, the slices were stained with rhodamine123 (200 nM) for 30 min. For inducing of tissue hypoxia, the slices were perfused with hypoxic ACSF.

2.5.3 Slice Maintenance: Perfusion Chambers

Different slice perfusion chambers were used depending on the specific requirements of the experiment.

2.5.3.1 Open chamber

The open perfusion chamber (RC-27L, Warner Instruments Inc.) (Fig.(2.8)) was used for all experiments in which a precisely defined perfusate oxygen concentration was not required. These included imaging experiments dealing with electrophysiology or introduction of pharmacological agents such as CN or FCCP.

The perfusate PO₂ cannot be precisely controlled in this chamber as the top surface of the fluid in the chamber is exposed to the air – allowing free exchange of oxygen with the perfusate. The equilibration with atmospheric PO₂ is not complete however. Typically, normoxic ACSF (95% O₂ + 5%CO₂) is perfused into one end of the chamber, and decreases in PO₂ from 0.95 atm to >~0.6 atm (450mmHg) by the

time it gets to the slice. Hypoxic ACSF (95% N₂ + 5%CO₂) on the other hand increases its PO₂ from ~0 to <~0.2 atm (150mmHg) (Fig.2.9, blue curve).

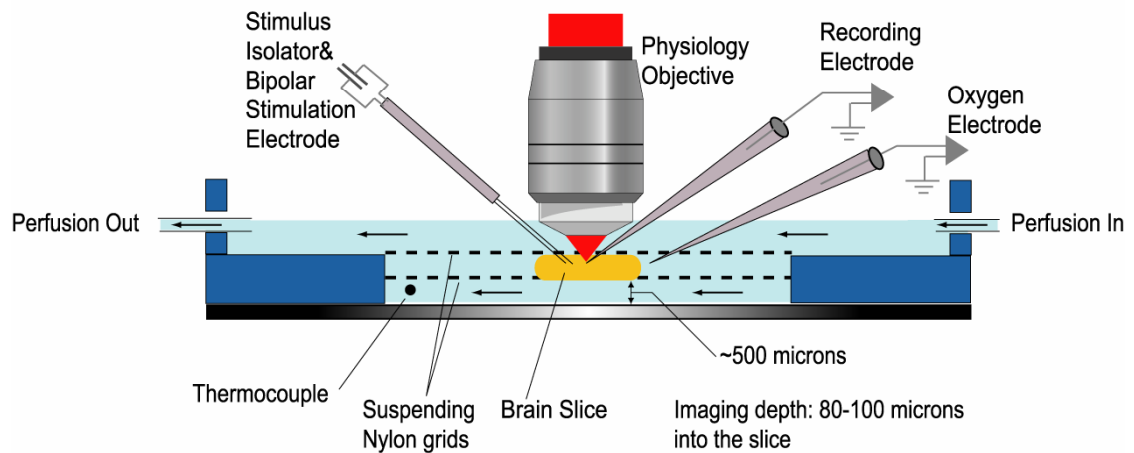


Figure 2.8 Open slice perfusion chamber. This chamber is often used for experiments involving electrophysiology.

While a PO₂ much lower than the 0.2 atm provided by hypoxic ACSF is required to induce the normoxic-hypoxic transition in mitochondria – this transition is still observable due to the PO₂ decrease as a function of depth into the slice (see Section 2.6). A significant response to hypoxia is observed at typical imaging depths (50-100µm) (Fig.2.9) – causing a ~15% increase in the NADH fluorescence and a collapse of the stimulation induced electrical activity (EPSP amplitude). The fluorescence increase on the lower surface of the slice is greater (~35-50%) due to less equilibration of the perfusate PO₂ with air.

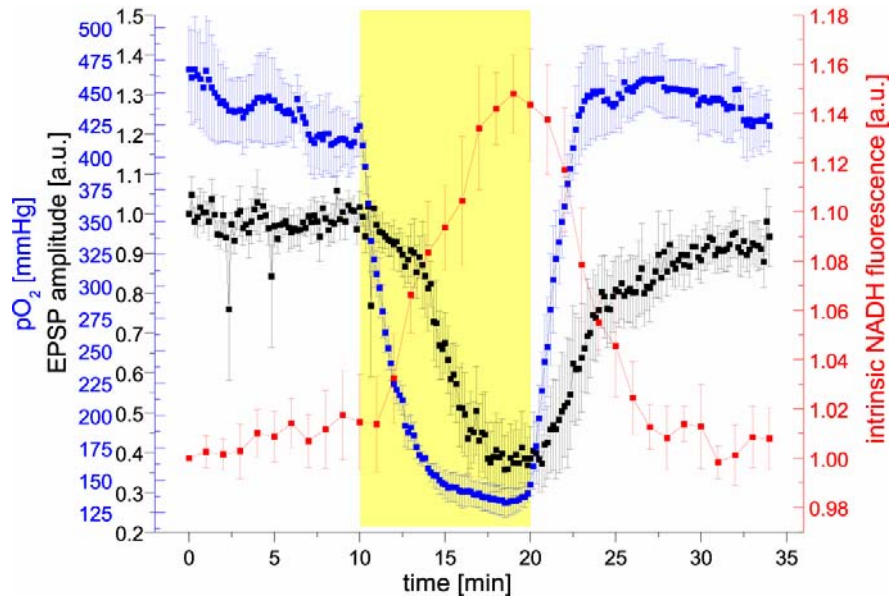


Figure 2.9 Hypoxia induced metabolic inhibition is possible even in an open slice chamber. Reducing the perfusate PO₂, combined with the natural oxygen gradient in tissue enables a hypoxic response in deep tissue.

2.5.3.2 Closed chamber

The closed chamber (Fig. 2.10) was designed for experiments in which the PO₂ of the perfusate must be well defined (e.g. Section 2.6). Both normoxic and hypoxic ACSF are bubbled until the desired PO₂ is reached. They are then loaded into airtight glass syringes (Gastight 100ml, Hamilton) from which they are perfused into the chamber by programmable pumps (Pump 22, Harvard Apparatus) through oxygen impermeable Saran tubing. The PO₂ in the chamber is set by the relative flow rates of the normoxic and hypoxic ACSF. The small volume (~0.18 ml) of the slice chamber ensures a fast solution exchange time (<10s) and therefore enables rapid changes in the chamber PO₂. For example, during the normoxic to hypoxic transition, the chamber PO₂ falls from 0.95 atm to <0.05atm in ~30s.

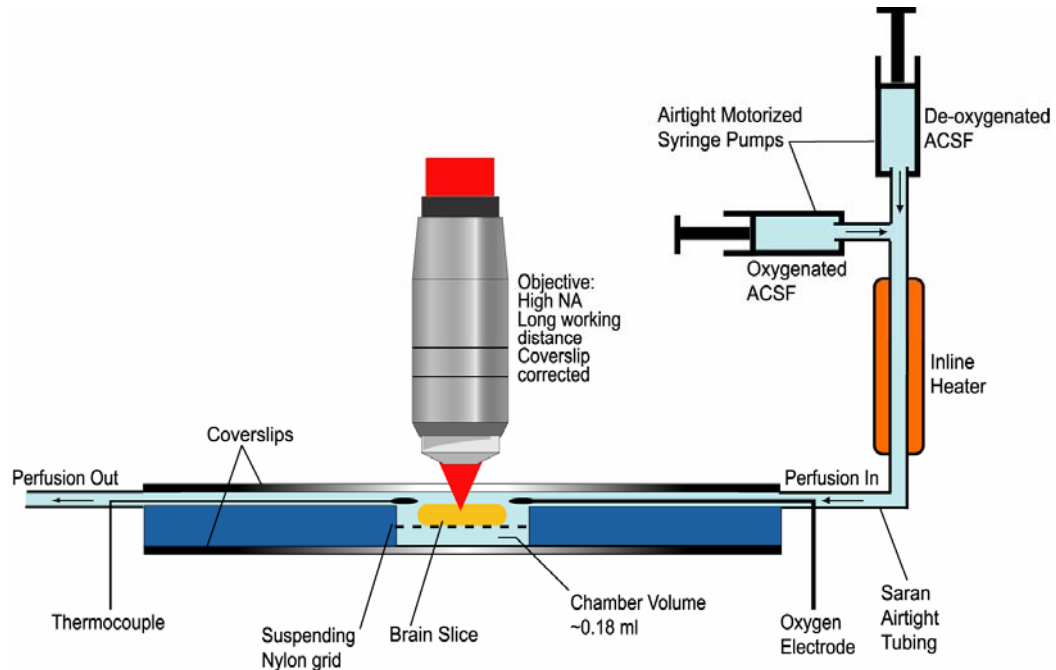


Figure 2.10 Closed slice perfusion chamber. This chamber enables a more precise control of perfusate PO_2 while also allowing fast exchange times.

Being able to step the PO_2 rapidly ensures that any temporal dynamics of the NADH response to changing PO_2 are solely biological in nature and do not reflect a slow solution exchange time. Furthermore, the rapid exchange time ensures that the entire slice experiences a change in PO_2 essentially simultaneously – and hence there are no spatial heterogeneities of the NADH response due to diffusion of the perfusate.

2.5.4 Surface damage due to preparation

During the process of slice preparation it is inevitable that neurons near the surface of the slice will be physically damaged. Slicing through the dendritic network of cells results in a catastrophic loss of homeostasis and cell death in a time and depth dependent manner (25). In order to do valid functional imaging in brain slices, it is therefore necessary to image deeper than this superficial damage. Wide field

fluorescence detection in the brain slice preparation is problematic as the detected fluorescence is dominated (due to low penetration of the excitation light) by the fluorescence of superficial tissue, which is damaged.

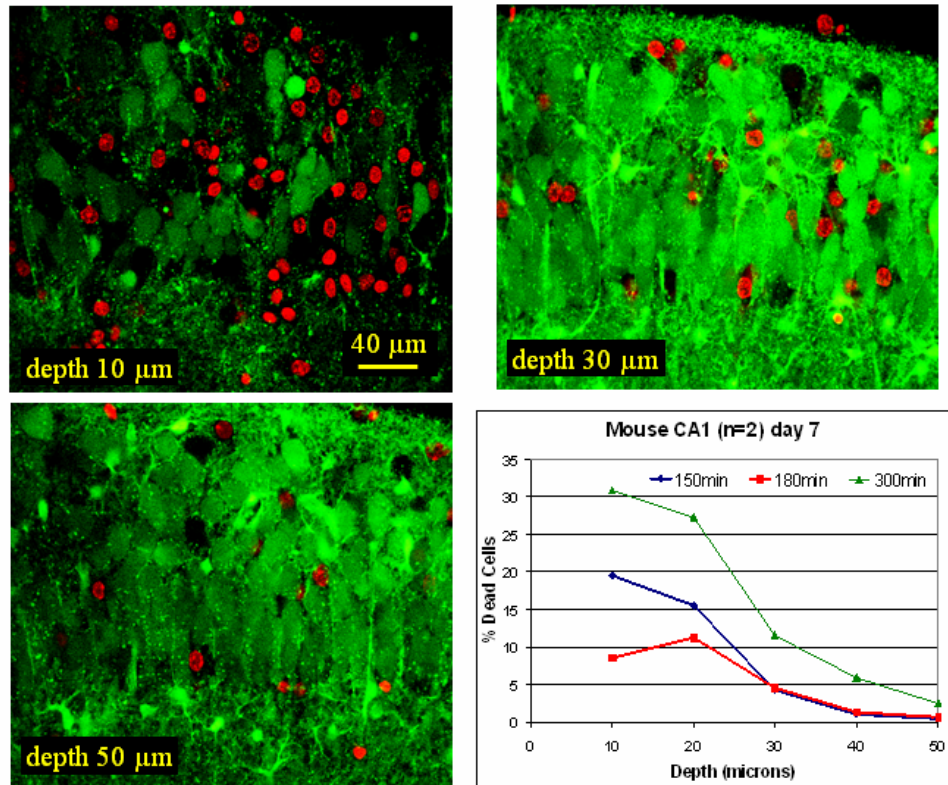


Figure 2.11 Live-Dead assay of depth dependent cell viability. The Live-Dead stain reveals that at a depth greater than ~30 microns, there is >90% cell survival for up to ~5 hours.

To assess the extent of the superficial damage, we used a commercial viability assay (Live/Dead Cell Viability Kit, Molecular Probes) (Fig. 2.11) in which Ethidium bromide (red) stains the nuclei of dead cells, and Calcein AM (green) stains the cell bodies of healthy cells. As expected, we found that the fraction of dead cells decreased with depth into the slice, while the number of dead cells at all depths increased with time. In general, imaging deeper than 30μm ensures a >90% cell viability for up to

~5hours. All imaging in this work was therefore done deeper than 30 μ m and slices were typically used within 4-5 hours of preparation.

2.5.6 Photobleaching & Photodamage

Intrinsic NADH undergoes photobleaching upon excitation. The bulk of the photobleaching product is simply the non-fluorescent NAD⁺, while a small fraction consists of irreversibly generated non-fluorescent dimers and trimers of NADH (26). The photooxidation of NADH can be thought of as a perturbation of the cellular metabolic state, which is a function of the NADH/NAD⁺ ratio. For low excitation doses, this bleaching is generally reversible as the cell naturally reestablishes its normal metabolic state. At higher excitation doses, the bleaching can become irreversible, both due to the irreversible accumulation of the dimers and trimers, as well as the excessive perturbation of the cellular metabolic state beyond its ability to recover. Balaban et al (26) have shown in cardiac myocytes that bleaching the intrinsic fluorescence to less than 70% of its baseline level leads to an incomplete recovery of the baseline fluorescence, indicating the significant production of irreversibly bleached products.

Under each of our imaging protocols, control exposures were done to assess the bleaching. In all imaging protocols, the intrinsic fluorescence signal underwent a slow decrease of less than 10% over the duration of our measurement (10-20 min.). Changes in morphology and induced broad autofluorescence characteristic of severe photodamage were not observed (see Section 3.1.5). The response of intrinsic fluorescence to changes in the metabolic state was both reversible and repeatable, indicating that our experiments did not cause irreversible short term damage.

2.6 Diffusion of oxygen into tissue

2.6.1 The reaction diffusion equation

Oxygen diffusion into tissue is generally described by the “reaction-diffusion equation”

$$DS\nabla^2 P(\vec{r}) - M = S \frac{\partial P(\vec{r})}{\partial t} \quad (2.26)$$

Where D is the diffusion coefficient of oxygen in tissue, $P(\mathbf{r})$ is the partial pressure of oxygen at a point \mathbf{r} , M is the rate of an irreversible chemical reaction in which oxygen is consumed and S is the solubility coefficient of oxygen in tissue ($\sim 1.12 \mu\text{mol}/\text{cm}^3 \text{ atm}$). The solubility coefficient relates the partial pressure of oxygen to its concentration ($C=SP$). The product DS is often referred to in the literature as the “Krogh diffusion constant”(27) and is taken to be a constant for a given tissue. We will also make this approximation, however, it has been suggested that there is considerable heterogeneity of diffusion in tissue (28), with more rapid diffusion through intracellular pathways of greater oxygen solubility. These pathways are thought to have higher lipid fractions e.g. regions of greater mitochondrial population. The experiments done here are largely performed in the stratum radiatum of the CA1 hippocampal layer. This region has a homogenous distribution of mitochondria, indicating that the assumption of a spatially invariant solubility is a reasonable approximation in our system.

There are a number of different models of tissue oxygen diffusion which differ in their functional form of the oxygen consumption rate (M). The four most commonly used models of oxygen consumption in tissue are the following.

1. Zero order kinetics (27,29,30)

$$\begin{aligned} M &= M_0 \text{ (constant) for } P > 0 \\ M &= 0 \text{ for } P = 0 \end{aligned} \quad (2.27)$$

2. First order kinetics

$$M = kP$$

$$k = \text{constant} \quad (2.28)$$

3. Mixed zero and first order kinetics

$$M = 0 \text{ for } P = 0$$

$$M = kP \text{ for } 0 < P < M_0/k$$

$$M = M_0 \text{ for } P > M_0/k \quad (2.29)$$

4. Michaelis-Menten kinetics (31)

$$M = M_0 \frac{P}{P + P_m} \quad (2.30)$$

Buerk and Saidel (29) have tested all four of these models on actual measurements of oxygen profiles in both brain and liver tissue slices and found the best fit to be from the Michaelis-Menten model. Their goodness of fit parameters for these four models are summarized in Table 2.2.

Table 2.2 Accuracy of models of oxygen consumption kinetics

Model	# free Parameters	χ^2 (Brain)	χ^2 (Liver)
Zeroth Order	1	0.4638	0.2901
First Order	2	9.997×10^{-2}	4.326×10^{-2}
Mixed	3	3.475×10^{-3}	1.033×10^{-2}
Michaelis-Menten	3	3.253×10^{-3}	5.178×10^{-3}

Historically, it is common to see mention of a “critical PO_2 ” as well as of a P_m . The “critical PO_2 ” is defined in the context of the mixed kinetic model – it is that PO_2 at which the rate of O_2 consumption switches from first order to zeroth order. P_m is

used in more recent literature, and is defined in the context of the Michaelis-Menten model as that PO_2 at which the rate of oxygen consumption drops to $\frac{1}{2}$ of its maximum. Depending on the experiment, the values of the critical PO_2 or P_m typically lie between 0.01 and 2 torr (29,32).

The exact equation for the O_2 consumption rate by the mitochondrial electron transport chain was derived by Wilson et al(7).

$$v = \frac{(1 - k_{-2} / K[c^{2+}])k_2[O_2][a_{3T}]}{\beta + \alpha[O_2]} \quad (2.31)$$

Where k_2 , k_{-2} , K , α and β are various enzyme constants of the electron transport chain and $[c^{2+}]$ and $[a_{3T}]$ are the concentrations of reduced cytochrome oxidase and cytochrome a_3 . What is important here is that this equation for oxygen consumption is indeed of the Michaelis-Menten functional form (Eqn.(2.30)).

2.6.2 Approximations to the reaction diffusion equation

The tissue perfusion chambers maintain an oxygen gradient in tissue slices by maintaining a constant oxygen concentration in the surrounding perfusate. To estimate this gradient therefore, entails solving the steady state reaction diffusion equation, i.e. setting $\partial P / \partial t = 0$ in Eqn.(2.26). Furthermore, a hippocampal slice is typically 2mm x 3mm in cross sectional area but only 300 μ m thick. The area that we most frequently image – the CA1 stratum radiatum - is a dendritic network near the center of the hippocampal slice. In this area, since our imaging depth is much smaller than the cross-sectional area, we can approximate the hippocampal slice as a semi-infinite slab of tissue. This reduces the dimensionality of the reaction diffusion equation. The resulting one dimensional steady state reaction diffusion equation with Michaelis-Menten consumption kinetics is then given by:

$$DS \frac{\partial^2 P(z)}{\partial z^2} - M_0 \frac{P(z)}{P(z) + P_m} = 0 \quad (2.32)$$

Furthermore, while the reaction diffusion equation with Michaelis-Menten kinetics is not analytically solvable, it can be analytically solved in two regimes of approximation:

1. $P \ll P_m$; The reaction-diffusion equation reduces to first order kinetics.

$$DS \frac{\partial^2 P(z)}{\partial z^2} - \frac{M_0}{P_m} P(z) = 0 \quad (2.33)$$

2. $P \gg P_m$; The reaction-diffusion equation reduces to zero order kinetics.

$$DS \frac{\partial^2 P(z)}{\partial z^2} - M_0 = 0 \quad (2.34)$$

As we have stated above, P_m is typically very low (0.01-2 torr). Imaging and spectroscopy done throughout this work are done at depths of 30-100 μ m. Tissue oxygen measurements made with oxygen electrodes (27,30), suggest the PO_2 values typical of our imaging depths in brain slices in a normoxic perfusate (10-100 torr) are substantially larger than this P_m . Hence for depths pertinent to imaging, we can approximate $P \gg P_m$ and the reaction diffusion equation reduces to zero order kinetics (Eqn.(2.34)).

2.6.3 Steady state oxygen profile in a brain slice

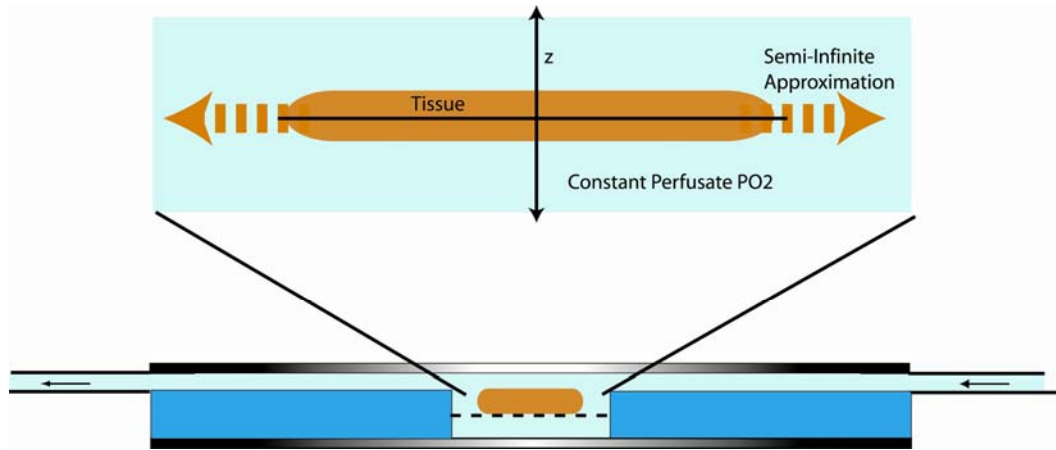


Figure 2.12 Semi-infinite approximation of a brain slice to calculate the oxygen gradient. To calculate the oxygen gradient in a slice, we approximate it as a semi-infinite slab, surrounded by perfusate with a well define oxygen level.

We approximate a typical brain slice as a semi-infinite slice ($x, y: \text{infinite}; -L/2 \leq z \leq L/2$), of thickness $L=300\mu\text{m}$, whose top and bottom are open to the perfusate (Fig.(2.12)). The perfusate PO_2 (P_p) is maintained constant at a value depending on the desired metabolic state and the perfusion chamber. In the open slice chamber, the normoxic PO_2 is ~ 0.6 atm and the hypoxic PO_2 is ~ 0.2 atm. In the closed slice chamber, the normoxic PO_2 is ~ 0.8 atm while the hypoxic PO_2 is ~ 0.05 atm. Under these conditions, the oxygen profile is then defined by:

$$\begin{aligned}
 DS \frac{\partial^2 P(z)}{\partial z^2} - M_0 &= 0 \text{ for } P(z) > 0 \\
 DS \frac{\partial^2 P(z)}{\partial z^2} &= 0 \text{ for } P(z) \leq 0 \\
 P(-L/2) &= P(L/2) = P_p
 \end{aligned} \tag{2.35}$$

Where M_0 has been measured to be $4.4 \mu\text{mol O}_2/\text{min cm}^3$ (29) and DS is $\sim 0.6 \times 10^{-3} \mu\text{mol O}_2/\text{min cm atm}$. The solution to Eqn.(2.35) is:

$$P(z) = \frac{M_0}{2DS} z^2 + \left(P_p - \frac{M_0 L^2}{8DS} \right) \text{ for } P(z) > 0 \quad (2.36)$$

$$P(z) = 0 \text{ for } P(z) \leq 0$$

This solution is plotted as a function of depth and perfusate PO_2 in Fig.(2.13).

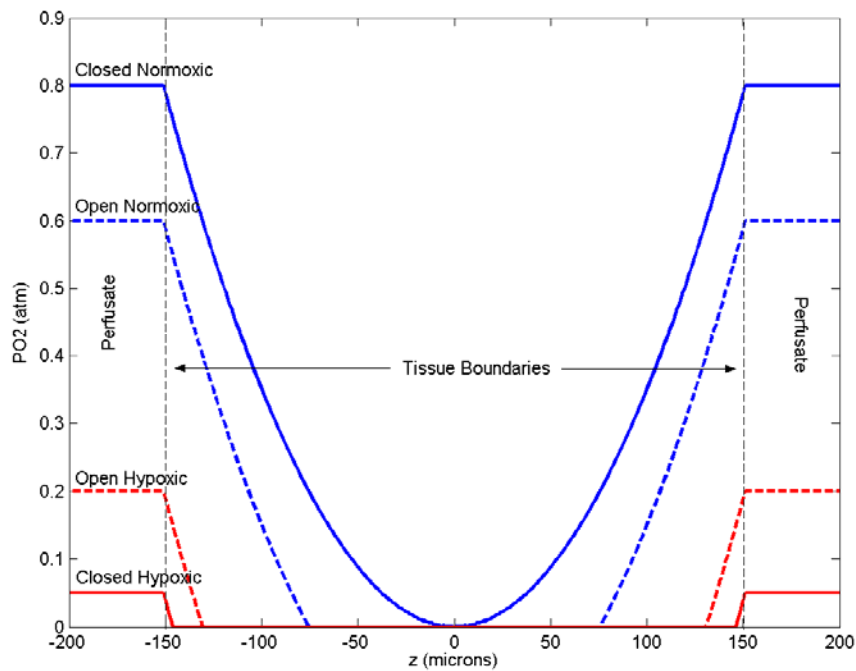


Figure 2.13 Oxygen profile in a brain slice. The oxygen profile in a living brain slice depends on the aerobic consumption rate of the tissue and the perfusate PO_2 . Curves are shown for open and closed perfusion chambers (see above) with normoxic and hypoxic buffers.

In the normoxic open chamber, the oxygen level reaches 0 by $\sim 75 \mu\text{m}$ into the slice. During hypoxia, the oxygen level reaches 0 by $\sim 20 \mu\text{m}$ into the slice. Hence imaging at depths of $40\text{-}70 \mu\text{m}$ is well suited to monitoring fluorescence changes associated with the normoxic to hypoxic metabolic transition. In the closed chamber,

at maximal bath PO_2 , the slice is nearly completely normoxic – the oxygen drops to the critical point briefly near the center of the slice. In the hypoxic closed chamber, the oxygen drops to 0 within a few microns. It should be remarked that the PO_2 does not actually reach zero since at the critical PO_2 of about 0.001 atm, the oxygen consumption switches to first order kinetics and the PO_2 decays as an exponential.

References

1. Stryer, L. (1998) *Biochemistry*, 4th Ed., W.H. Freeman and Company, New York
2. Williams.Dh, Lund, P., and Krebs, H. A. (1967) *Biochemical Journal* **103**, 514-&
3. Bucher, T., Brauser, B., Sies, H., Langguth, O., Conze, A., and Klein, F. (1972) *European Journal of Biochemistry* **27**, 301-&
4. Merrill, D. K., and Guynn, R. W. (1976) *Journal of Neurochemistry* **27**, 459-464
5. Panda, M., and Robinson, N. C. (1995) *Biochemistry* **34**, 10009-10018
6. Wilson, M. T., Antonini, G., Malatesta, F., Sarti, P., and Brunori, M. (1994) *Journal of Biological Chemistry* **269**, 24114-24119
7. Wilson, D. F., Owen, C. S., and Erecinska, M. (1979) *Archives of Biochemistry and Biophysics* **195**, 494-504
8. Benz, R., and McLaughlin, S. (1983) *Biophysical Journal* **41**, 381-398
9. Brown, G. C. (1992) *Biochemical Journal* **284**, 1-13
10. Jafri, M. S., and Dudycha, S. J. (2001) *Biophysical Journal* **80**, 589A-589A
11. Jafri, M. S., Dudycha, S. J., and O'Rourke, B. (2001) *Annual Review of Biomedical Engineering* **3**, 57-81
12. Nicholls, D. G., and Budd, S. L. (2000) *Physiological Reviews* **80**, 315-360
13. Shuttleworth, C. W., Brennan, A. M., and Connor, J. A. (2003) *Journal of Neuroscience* **23**, 3196-3208
14. Aubert, A., Costalat, R., and Valabregue, R. (2001) *Acta Biotheoretica* **49**, 301-326
15. Korzeniewski, B., and Mazat, J. P. (1996) *Acta Biotheoretica* **44**, 263-269
16. Heikal, A. A., Hess, S. T., and Webb, W. W. (2001) *Chemical Physics* **274**, 37-55
17. Axelrod, D. (1989) *Methods in Cell Biology* **30**, 333-352

18. Couprie, M. E., Merola, F., Tauc, P., Garzella, D., Delboulbe, A., Hara, T., and Billardon, M. (1994) *Review of Scientific Instruments* **65**, 1485-1495
19. Bialik, C. N., Wolf, B., Rachofsky, E. L., Ross, J. B. A., and Laws, W. R. (1998) *Biophysical Journal* **75**, 2564-2573
20. Fisz, J. J. (1996) *Chemical Physics Letters* **259**, 579-587
21. Knutson, J. R., Beechem, J. M., and Brand, L. (1983) *Chemical Physics Letters* **102**, 501-507
22. Lakowicz, J. R. (1999) *Principles of Fluorescence Spectroscopy*, 2 Ed., Kluwer Academic/Plenum Publishers
23. O'Connor, D. V., and Philips, D. (1984) *Time correlated single photon counting*, Academic Press, London
24. Wang, T., and Kass, I. S. in *Methods in Molecular Biology 72: Neurotransmitter Methods* (Rayne, R. C., ed) Vol. 72, pp. 1-14, Humana Press, Totowa, NJ
25. Kasischke, K., Buchner, M., Ludolph, A. C., and Riepe, M. W. (2001) *Acta Neuropathologica* **101**, 483-490
26. Joubert, F., Fales, H. M., Wen, H., Combs, C. A., and Balaban, R. S. (2004) *Biophysical Journal* **86**, 629-645
27. Ganfield, R. A., Nair, P., and Whalen, W. J. (1970) *American Journal of Physiology* **219**, 814-&
28. Dutta, A., and Popel, A. S. (1995) *Journal of Theoretical Biology* **176**, 433-445
29. Buerk, D. G., and Saidel, G. M. (1978) *Microvascular Research* **16**, 391-405
30. Bingmann, D., and Kolde, G. (1982) *Experimental Brain Research* **48**, 89-96
31. Popel, A. S. (1979) *Journal of Theoretical Biology* **80**, 325-332
32. Sugano, T., Oshino, N., and Chance, B. (1974) *Biochimica Et Biophysica Acta* **347**, 340-358

Chapter Three

Intrinsic Fluorescence in Brain Tissue

3.1 Sources of intrinsic signals (other than NADH)

There are a number of known sources of fluorescence and second harmonic signals that are found intrinsically present in native, unstained tissues. These intrinsic fluorophores are typically very weak and hence fluorescence imaging of externally applied dyes or genetically targeted fluorescent proteins observe this intrinsic fluorescence as a weak background signal. However, since our work specifically deals with intrinsic NADH fluorescence, we must consider the other possible intrinsic sources. The discussion below considers the more common known fluorophores associated with neural tissue and demonstrates that under specific excitation and emission conditions, the intrinsic fluorescence is predominately due to NAD(P)H.

3.1.1 Amino acids

Many proteins are intrinsically fluorescent due to the presence of tryptophan, tyrosine and/or phenylalanine residues. These molecules typically absorb in the far UV (240-300nm) and emit in the near UV (250-400nm) (Table 3.1) (1).

Table 3.1 Fluorescent amino acids

	Excitation (nm)	Emission (nm)
Phenylalanine	260	282
Tyrosine	275	304
Tryptophan	295	353

Two-photon excitation spectra of both tryptophan and tyrosine are somewhat different from their one-photon counterparts – this effect is more pronounced in the case of tryptophan. Both excitation spectra are however negligible by ~620nm (2). Hence, two-photon excited fluorescence of proteins is not significant at wavelengths typically used for two-photon imaging (700-1000nm).

3.1.2 Retinoids

Retinoids are vitamin A derivatives that are known to play roles in the development and maintenance of several tissues. In the brain, the primary retinoid is retinoic acid (RA), which binds to a family of nuclear retinoic acid receptors (RARs) to regulate transcription. Retinoic acid is known to play a role in neurogenesis and differentiation in the developing and adult central nervous system (3). RA also plays a role in synaptic plasticity and neurogenesis in the adult rat hippocampus (4,5). In fact,

the hippocampus not only uses retinoids, but has also been shown to synthesize retinoids – primarily in the dentate gyrus, but also in the layers CA1-3 (5).

The two-photon action cross section of retinol (vitamin A alcohol) peaks near 700nm at 0.07GM (6) – comparable to that of NADH (~0.09GM at 700nm) (7). The emission peak is ~480nm – also very similar to NADH. All-trans retinoic acid excites at 365nm and emits in the range of 370nm-600nm with a peak at ~400nm (the 2P action cross section has not been measured). Upon binding to RAR-gamma, the peak is red-shifted to ~430nm and the emission is enhanced by ~2-3X (8). The absolute concentrations of retinoids in the brain have not been measured. However, the retinol and RA concentrations in the liver (believed to have relatively high retinoid levels) have been measured to be on the order of ~10nmol/g and 1nmol/g wet weight respectively. Assuming the tissue density to be approximately that of water, these concentrations correspond to 10 μ M for retinol and 1 μ M for RA. If the concentration of retinol and/or retinoic acid in brain is even comparable to that in liver, then retinoids would be present in the hippocampus at much lower concentrations than NADH (~100 μ M). Taken together with the fact that the two-photon action cross sections of retinol and NADH are comparable, the much lower retinoid concentration would make retinoids a small component of the total intrinsic neuronal fluorescence.

Furthermore, since RA is a nuclear transcription regulator, its presence should be revealed by a nuclear fluorescence in the cell layers of the hippocampus. In our observations, the hippocampal nuclear fluorescence has been exceedingly weak - typically on the level of background noise – indicating that the RA contribution to the intrinsic fluorescence is minimal.

3.1.3 Lipofuscin

Lipofuscin is a yellowish-brown pigment that accumulates slowly with age into small, dense granules about 1-5 μ m in diameter (9). This substance is thought to be a product of lipid peroxidation in post-mitotic cells, initiated by reactive oxide species and followed by non-specific decomposition of the products into fluorescent compounds. The final composition of lipofuscin, and therefore its spectral properties, is not well defined. Typically however, lipofuscin granules excite with UV light (~360nm) and have emission spectra that can range from blue to yellow (9).

In the rat brain, the hippocampus is among the first structures to begin showing lipofuscin accumulation as a function of age and accumulates it at the highest rate of any brain structure. However, this accumulation does not begin until about 8 weeks of age (10). Given that our experiments were done on rats of 2-3 weeks of age, lipofuscin is not a likely contributor to our fluorescence signal.

3.1.4 Microtubules

Microtubules are sources of non-linear scattering at exactly half the excitation wavelength – known as second harmonic generation (SHG). There is sufficient parallel alignment of microtubules in the axons of neurons that a significant SHG signal can be detected (11). In the hippocampus, there is a strong SHG signal generated from the axon bundles that run between the dentate gyrus and the CA3 layer, known as the mossy fibers (Fig. (3.1)). A much weaker signal is also detectable from the Schaeffer collaterals – the bundle of axons running between the CA3 and CA1 layers. While the intensity of the SHG signal in the mossy fibers is comparable to that of the intrinsic fluorescence of the surrounding neuropil under 740nm excitation, the SHG is directed almost entirely (>90%) in the forward direction. Since our fluorescence detection path is in the backwards direction, neither our images nor

wavelength resolved spectroscopy have shown a significant contribution from microtubule SHG.

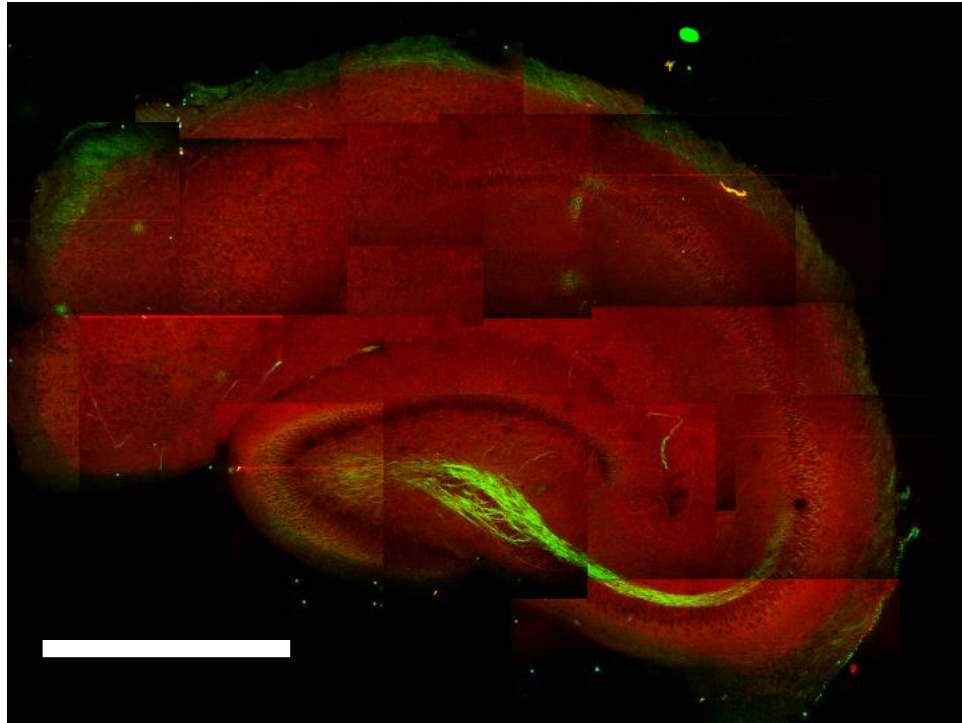


Figure 3.1 SHG from aligned microtubules in axons. Image of the intrinsic fluorescence (red) and SHG (green) arising from aligned microtubules in axons. Scale bar is 1mm.

3.1.5 Induced autofluorescence

Overexposure of tissue to exciting radiation can lead to photodamage. At low to moderate excitation doses, this damage is manifest as a simple photobleaching of the intrinsic fluorescence. In the case of NADH, the majority of the bleaching product is simply the non-fluorescent oxidized dinucleotide: NAD^+ (12).

At a sufficiently high excitation dose, it is possible to induce new fluorescence in tissue. Although there has been little work to establish the composition of these

autofluorescent compounds, it is generally believed that they are created by the cross-linking of photo-excited molecules (e.g. proteins). Spots of photodamage induced autofluorescence tend to appear as blebs with an ill defined structure (Fig.3.2) and emission spectrum.

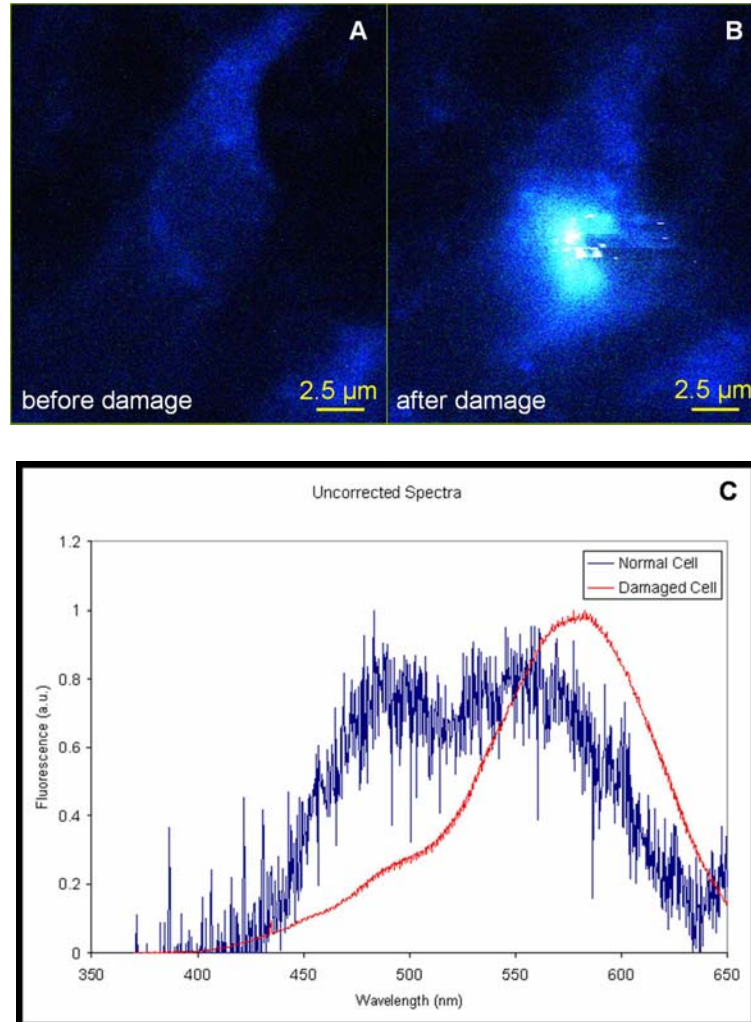


Figure 3.2 Induced autofluorescence due to severe photodamage. Induced autofluorescent blebs are (B) morphologically and (C) spectrally ill defined. The excitation beam (~45mW) was parked on a hippocampal neuron for >10s. The signal cut off at >650nm is due to a cut off in the transmission of the detection optics.

This type of damage can generally be avoided by using the minimum excitation power required for acceptable image quality. Under imaging conditions typical of our time series studies in the hippocampus, we observe a ~10% bleach in the NADH intensity throughout the course of the time series, and no induced autofluorescence

3.1.6 NADPH

Nicotinamide adenine dinucleotide phosphate is virtually identical in structure to NADH with the exception of an extra phosphate group in the bridge between the nicotinamide and adenine rings. Like NADH, the fluorescent NADPH also forms a redox pair with its non-fluorescent oxidized form NADP^+ . NADH and NADPH are distinct in their biochemical roles: NADH being largely restricted to energy metabolism and NADPH largely to reductive biosynthesis (13). However, there is no known photophysical means of discriminating NADH and NADPH either in solution (14) or in biological samples (15). Therefore, it is a common practice to assign intrinsic blue tissue fluorescence to “NAD(P)H” without considering the relative contributions of the two reduced pyridine nucleotides.

The concentrations of pyridine nucleotides have been measured by HPLC in mouse hippocampus (15). It was found that the total concentration of diphosphopyridine nucleotides (NADH and NAD^+) is greater than that of triphosphopyridine nucleotides (NADPH and NADP^+) by a factor of ~10. The concentration of the reduced fluorescent species NADH was found to be ~5 times greater than that of the fluorescent NADPH. Furthermore, the enhancement of mitochondrial NADH quantum yield due to environmental effects was estimated to be a factor of 1.25-2.5 greater than that of NADPH (16). This implies that the

contribution of NADPH to the intrinsic fluorescence, while not insignificant, represents a small fraction of the NADH contribution.

Furthermore, tissue analyses of pyridine nucleotide content in heart and liver have confirmed that the fluorescence changes during the normoxic-anoxic transition are dominated by changes in NADH with only a minor (~10%) contribution of NADPH (17). Hence, NADPH represents a minor fluorescence background that is roughly constant with respect to metabolic perturbations.

3.1.7 Flavins

These are a family of compounds that are derivatives of or contain the flavin mononucleotide (FMN) group. Of particular relevance here flavin adenine dinucleotide (FAD), like NADH, is a fluorescent redox molecule. The oxidized state (FAD^+) is fluorescent, the reduced state (FADH_2) is non-fluorescent and its oxidation state is a function of the metabolic state of the cell (18). The FAD^+ and NADH fluorescence emissions are spectrally distinct. The flavin signal that we observe in the hippocampus has an emission peak (~550nm) significantly higher than the NADH emission peak, and can therefore be easily discriminated from the NADH signal through a judicious choice of emission filter. Flavin detection and filtering is discussed further in Section (3.4) and so we shall not discuss it further here.

3.2 Identification of NADH

A number of intrinsic fluorophores are intrinsically present in neural tissue. However as we have discussed above, given the conditions of our excitation, emission filtering, detection geometry and brain region selection, the only fluorophores that are likely to contribute significantly to our images are NADH, NADPH and flavins. To strengthen the argument that the dominant fluorophore in these studies is NADH, we

provide arguments based on the morphology of the fluorescence, its functional behavior, and its steady state (wavelength resolved) fluorescence spectrum.

3.2.1 Morphology of intrinsic fluorescence

3.2.1.1 Cultured neural cells

The intracellular intrinsic fluorescence under our excitation (720nm) and emission (410-490 nm) conditions in cultured neurons and glial cells exhibits a pattern of bright punctuate organelles scattered throughout the dim cytoplasm (see Fig.3.3).

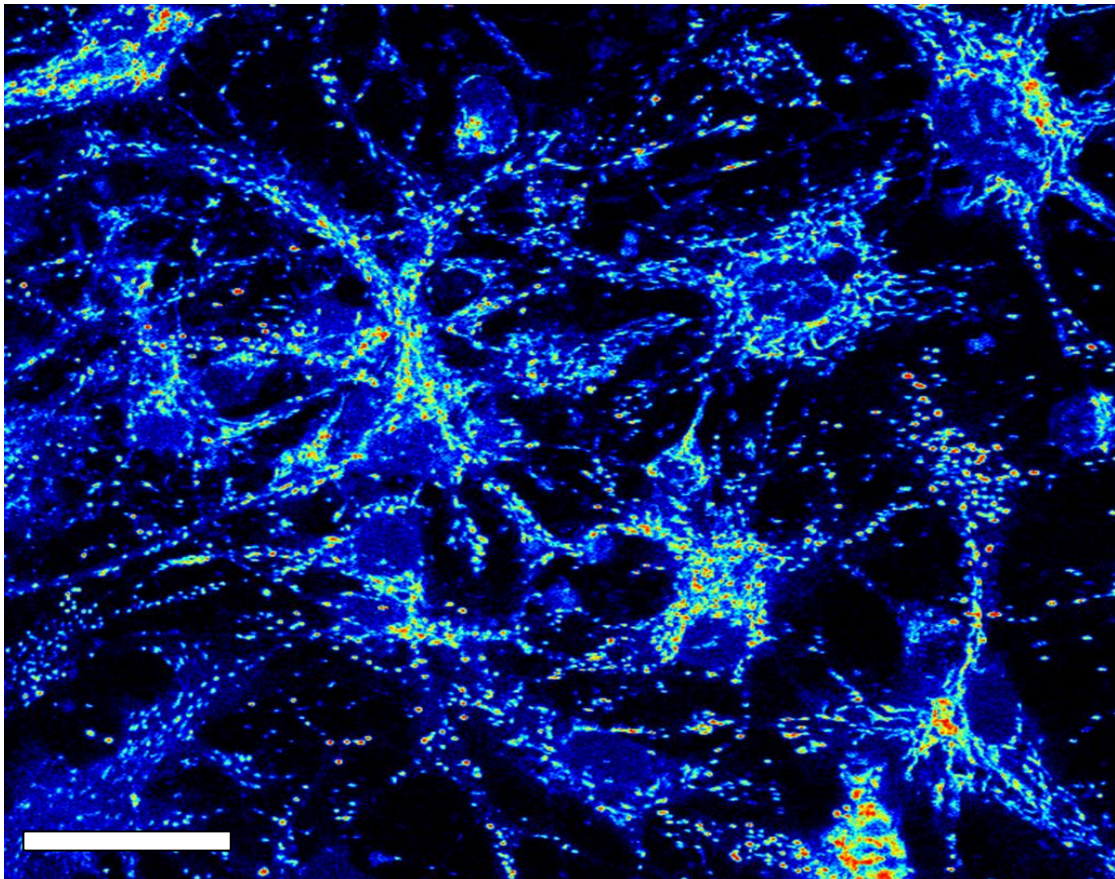


Figure 3.3 Intrinsic fluorescence in cultured neurons and glial cells. Bright punctuate spots are mitochondria, while the cytosol is diffuse and dim. Nuclei appear as dim, large and circular regions. Scale bar is 50 μ m.

These punctuate organelles are typically between 0.5-1 μM in width and vary in their length from being short and approximately spherical to slender and highly elongated. The fluorescence in the rest of the cytoplasm is homogenous and dim. The nuclei can clearly be identified as circular or oval structures with a diameter of $\sim 10 \mu\text{m}$ that exhibit a homogenous fluorescence slightly dimmer than that of the cytoplasm.

The morphology of the bright, punctuate organelles is consistent with that of mitochondria. To test this identification, we have utilized the conventional mitochondrial dye, rhodamine 123 (Rh123; Molecular Probes). Cultures of hippocampal neurons and glial cells were stained with Rh123 ($\sim 100\text{nM}$) and the Rh123 and intrinsic fluorescence were imaged simultaneously (Fig.3.4). Intrinsic fluorescence (red pseudocolor, Fig.(3.4a)) and Rh123 (green pseudocolor, Fig.(3.4b)) images show excellent co-localization (yellow, Fig.(3.4c)), indicating that these punctuate objects of high intrinsic fluorescence are indeed mitochondria. The cross talk between intracellular autofluorescence (peak at $\sim 440 \text{ nm}$) and Rh123 (peak at 530 nm) channels is negligible due to the difference in their fluorescence spectra.

3.2.1.2 Acute hippocampal slices

In hippocampal slices, neurons are organized in a much more compact and interwoven 3-dimensional network than in cultures and hence it is difficult to clearly distinguish punctuate mitochondria and smooth cytoplasm. Nonetheless, the intrinsic and Rh123 fluorescence images (Fig.(3.4d-f)) still exhibit a co-localized granularity similar to that in cultured cells.

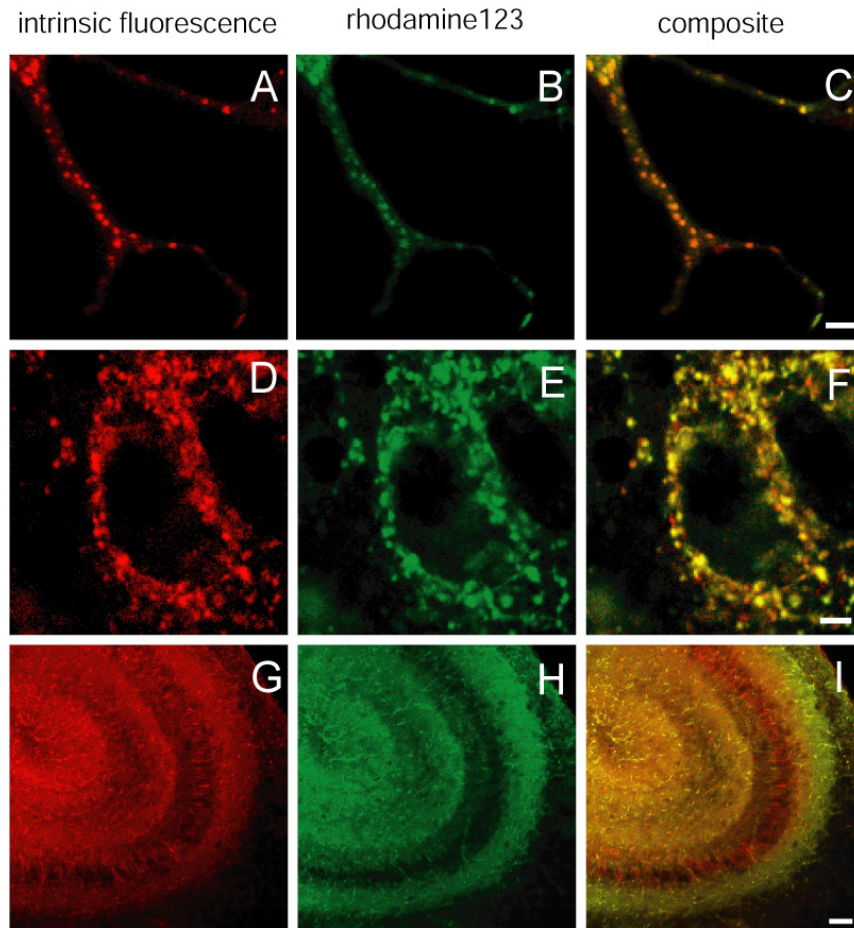


Figure 3.4 Colocalization of NADH and Rh123 in cultured neurons and hippocampal slices. Intrinsic fluorescence (red) and Rh123 (green) show excellent colocalization (yellow) in cultured cells (A-C), single hippocampal neurons (D-F) and macroscopic hippocampal layers (G-I). Scale bars: top row - 5 μ m, middle row - 5 μ m, bottom row - 50 μ m.

The macroscopic pattern of the intrinsic fluorescence in the hippocampus shows a well defined structure. In the region CA1, the fluorescence is brightest in the molecular layer, intermediate in the stratum radiatum, lowest in the stratum pyramidale and intermediate in the stratum oriens. The pattern in the region CA3 (Fig.(3.4g-i)) is quite different. Note the layered pattern, with bright fluorescence in the molecular layer and in the stratum oriens and low fluorescence in the pyramidal

layer and the stratum radiatum. This layer of low fluorescence is in turn divided by a thin layer of intermediate fluorescence that is not present in region CA1. Hence, even though it is more difficult in slices to correlate single Rh123 stained mitochondria with intrinsically fluorescent granules, we can readily see similarity between the macroscopic mitochondrial distribution and the banding pattern of the intrinsic fluorescence.

The morphology of the intrinsic fluorescence establishes a mitochondrial origin for the majority of the intrinsic fluorescence.

3.2.2 Pharmacological response of intrinsic fluorescence

The response of the intracellular NADH level to specific pharmacological manipulations has been well established (see Section 2.1). In mitochondria, the electron transport chain (ETC) is the only oxidizer of NADH, and hence pharmacological manipulation of the flux through the ETC offers a direct and predictable means of altering the mitochondrial NADH/NAD⁺ ratio. Conversely, measuring the response of cellular fluorescence to these specific pharmacological manipulations offers a means to test for the presence of NADH.

Two classes of effects are used here to test for NADH – ETC inhibition and uncoupling of oxidative phosphorylation (see Section 2.1 for underlying biochemical mechanisms). Inhibition of the ETC is done with cyanide or hypoxia and results in an increase in the NADH fluorescence. Uncoupling is done with FCCP – a weak lipophilic acid that collapses the mitochondrial inner membrane potential and leads to a decrease in mitochondrial NADH.

3.2.2.1 Response of cultured neurons and glial cells to inhibition and uncoupling

In cultured neural cells, perfusion with cyanide for 5 minutes leads to a completely reversible increase with no apparent adverse effects (Fig. (3.5)). On the other hand, a 5 minute perfusion with FCCP was not completely reversible which might be explained by the fact that FCCP is a weak lipophilic acid that gets taken up into the mitochondrial membrane and is slow to diffuse out of the membrane.

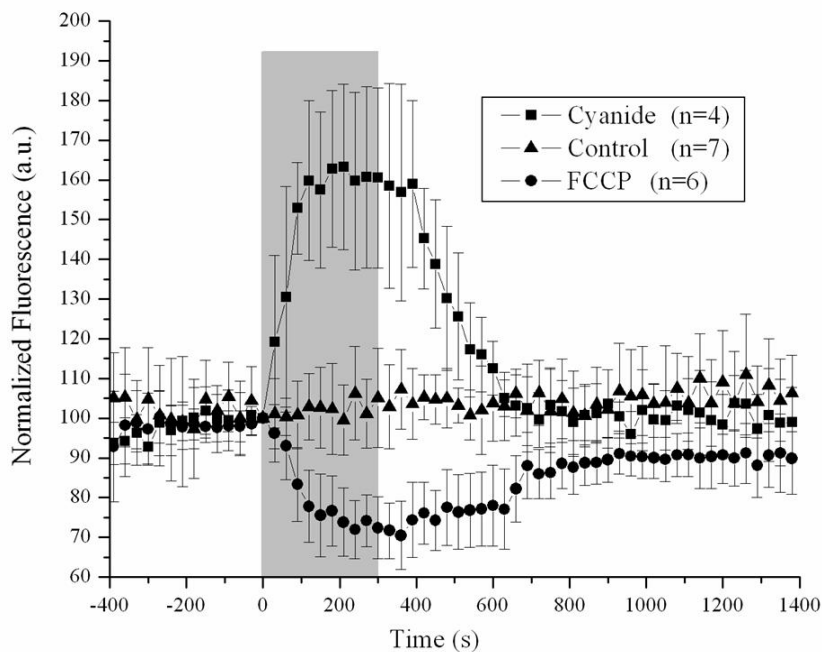


Figure 3.5 Response of intrinsic fluorescence in cultured neurons to inhibition and uncoupling. Metabolic inhibition with cyanide leads to a fluorescence increase while uncoupling with FCCP leads to a fluorescence decrease. This response is consistent with the intrinsic fluorescence arising from NADH.

3.2.2.2 Response of intrinsic fluorescence in brain slices to cyanide

In brain slices, reversible inhibition of the ETC in brain slices was possible with both cyanide and hypoxia. However, it was not practical to use the uncoupler

FCCP as this lipophilic drug is rapidly absorbed into the highly lipid rich neuropil and hence does not penetrate to any significant depth into the tissue.

A known concentration of cyanide is added to the perfusate for a brief period (5 min) in order to induce a reversible inhibition of the ETC. The response of the brain slice is a transient increase in the intrinsic fluorescence in the soma and the processes, while the nuclei remain dark (Fig.(3.6)).

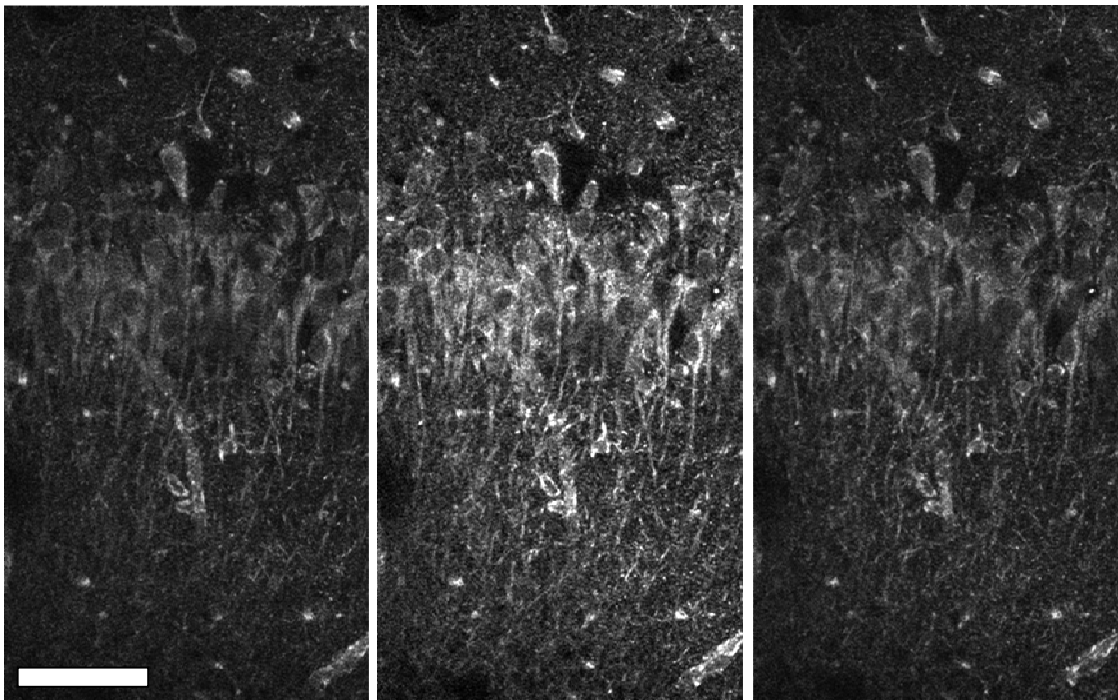


Figure 3.6 Response of hippocampal brain slice to cyanide. Hippocampal neurons (A) undergo a transient fluorescence increase in response to cyanide (B). The fluorescence returns to near baseline levels (C) upon reperfusion. Contrast has been enhanced for clarity of presentation. Scale bar is 50 μ m.

The average fluorescence from the slice is shown in Fig.(3.7) as a function of time for a range of cyanide doses. Each fluorescence response exhibits a rapid increase to its peak upon introduction of cyanide followed by a somewhat slower decay of the fluorescence after washing the cyanide out of the surrounding bath.

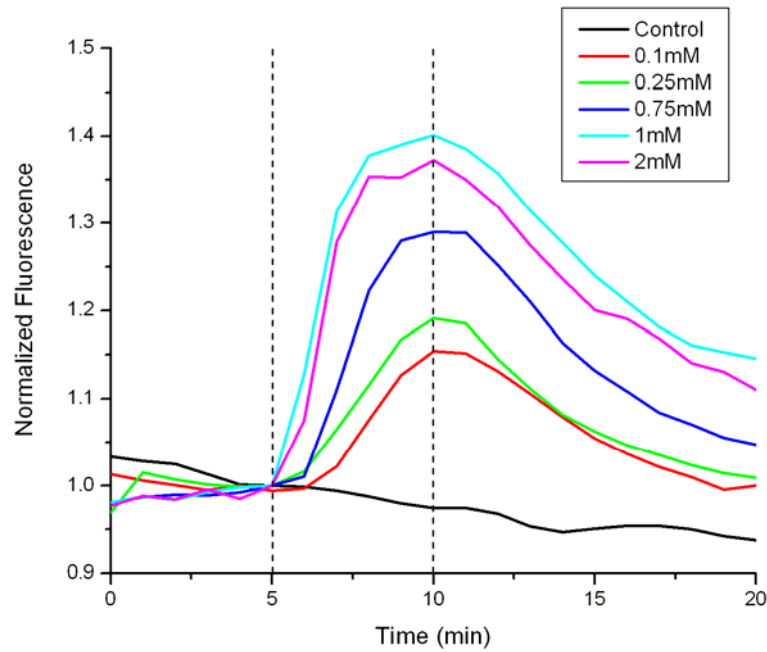


Figure 3.7 Temporal response of brain slice intrinsic fluorescence to cyanide.

The magnitude of the NADH fluorescence response to cyanide was dose dependent. The response peak increases with increasing perfusate cyanide concentration (Fig.(3.8)) with a saturation beginning to occur at $[CN] \sim 1\text{mM}$. This saturation behavior is characteristic of phenomena associated with competitive binding and implies that at this perfusate concentration of cyanide, essentially all oxygen binding sites in complex IV molecules are binding cyanide instead and hence inhibition of the ETC is maximal.

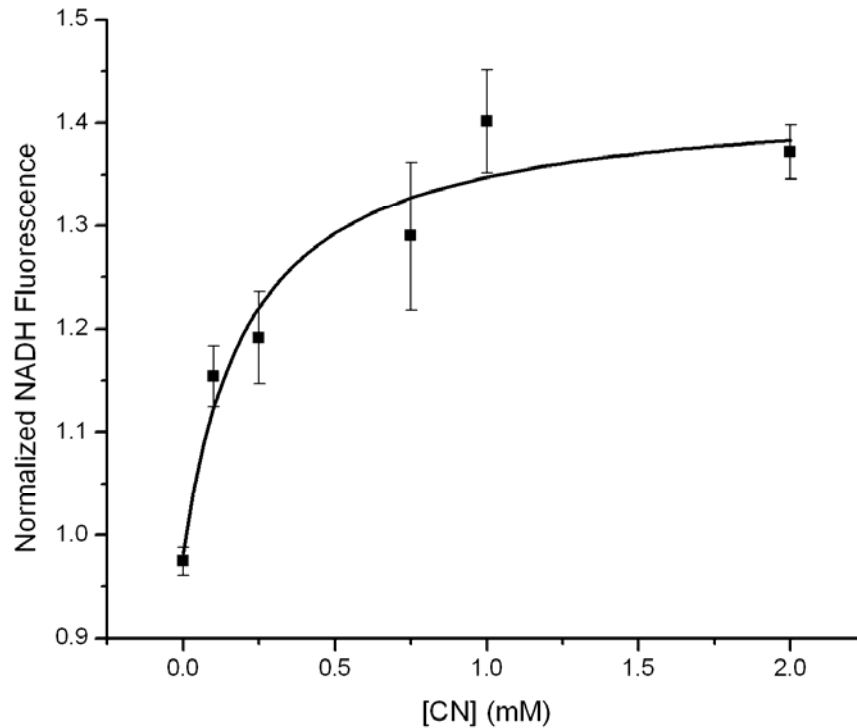


Figure 3.8 Dose dependence of intrinsic fluorescence to cyanide. Saturation of the peak response at high [CN] occurs due to saturation of oxygen binding sites by cyanide.

3.2.2.2 Oxygen dependence of intrinsic fluorescence in brain slices

The oxygen partial pressure (PO_2) of the surrounding perfusate was also varied to test the dependence of the intrinsic fluorescence on oxygen. Images were recorded 40-50 μ m within the brain slice while the oxygen level was recorded in the perfusate surrounding the tissue while. Since actively respiring tissue consumes oxygen, there is some attenuation of the oxygen partial pressure between the level in the perfusate and that at the imaging depth (see Section 2.5). Based on oxygen diffusion gradients measured in brain slices, we estimate the PO_2 at typical imaging depths to be 30-50% lower than the perfusate partial pressure.

The fluorescence of the brain slice in response to a 5 min. episode of hypoxia ($\text{PO}_2 \rightarrow 0$) shows both a rapid rise and rapid return to baseline level (Fig.(3.9)). This rapid response reflects the fact that this process is a simple substrate removal with no more complicated binding kinetics.

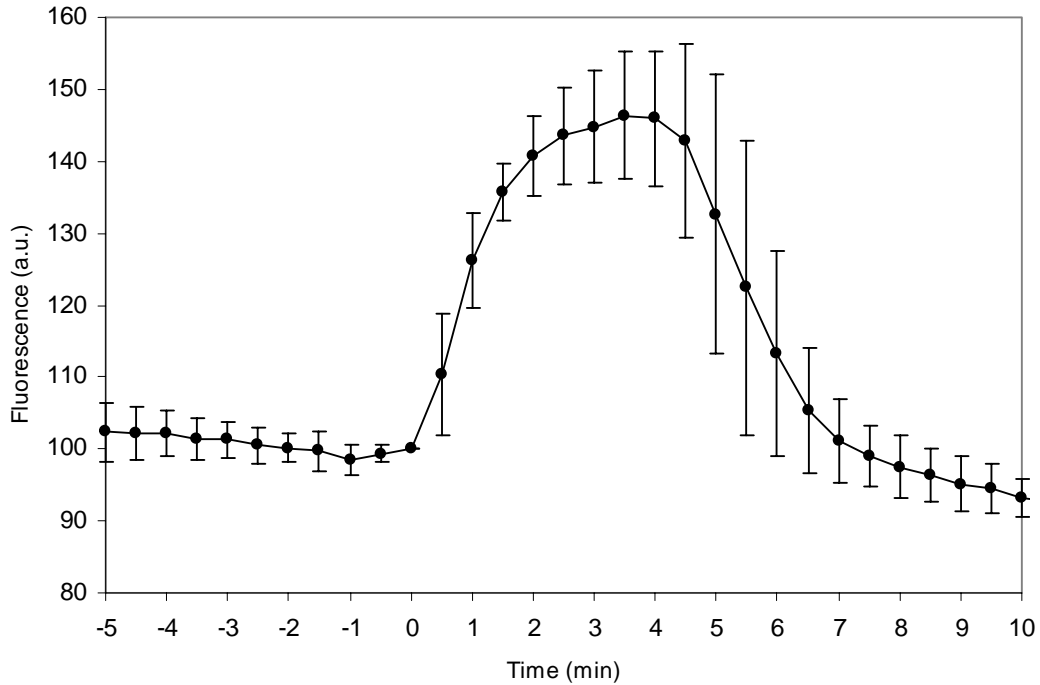


Figure 3.9 Response of brain slice intrinsic fluorescence to transient hypoxia

Reducing the substrate oxygen level in a graded manner (Fig.(3.10a)) shows that the fluorescence level is relatively insensitive to the perfusate oxygen over a large range. Between ~ 0.9 atm and 0.2 atm perfusate PO_2 there is only a $\sim 5\%$ increase in the average fluorescence of the brain slice. A rapid increase in the fluorescence begins only below 0.2 atm perfusate PO_2 . The dependence of NADH fluorescence on PO_2 reveals a saturation effect at high PO_2 (Fig.(3.10b)) – expected from Michaelis-Menten enzyme kinetics.

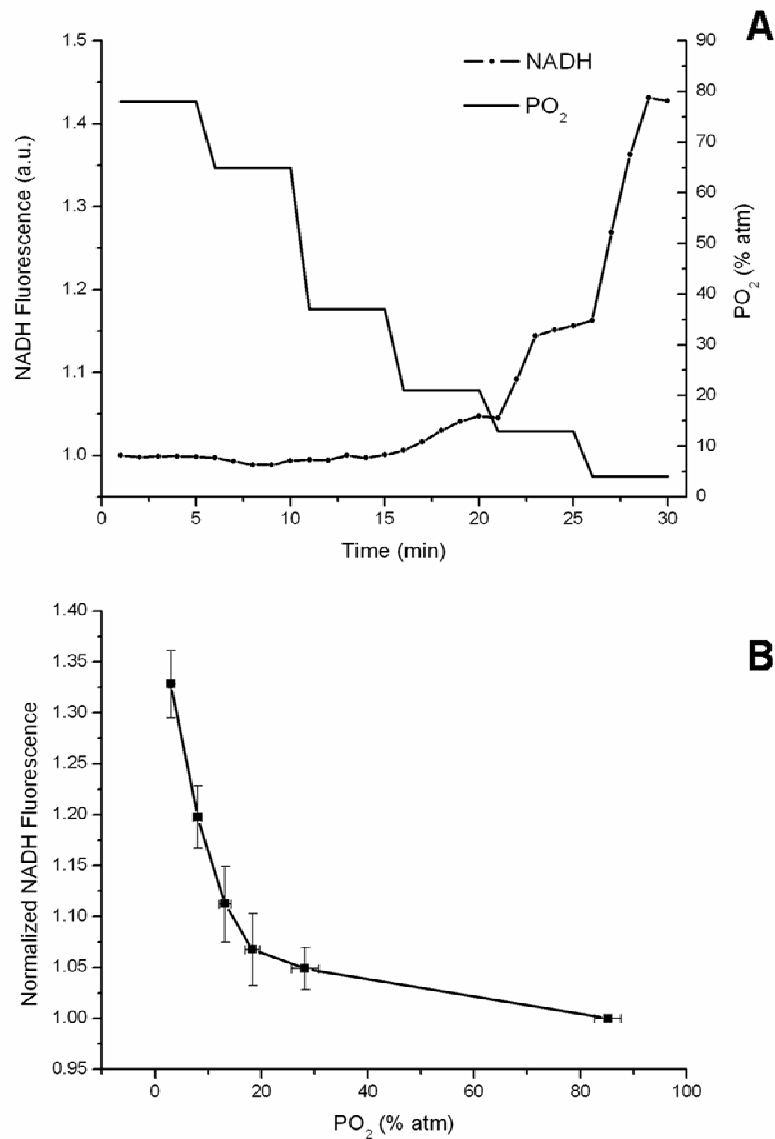


Figure 3.10 Bath oxygen dependence of intrinsic fluorescence. Graded hypoxia (A) reveals an insensitivity of fluorescence to a large range of high bath PO₂. The PO₂ dependence of intrinsic fluorescence (B) reveals saturation at high PO₂.

3.2.3 Steady state (wavelength resolved) spectroscopy of intrinsic fluorescence

We have confirmed that the observed emission in brain slices is 2P-fluorescence by measuring its quadratic dependence on the excitation power (Fig.(3.11)). The quadratic dependence implies that both saturation and

photobleaching of the intrinsic intracellular fluorophore do not occur under our imaging conditions. Deviation from the I^2 dependence due to fluorophore excitation saturation effects does occur at higher excitation powers. This saturation regime can easily be avoided by using the lowest power possible with acceptable signal to noise.

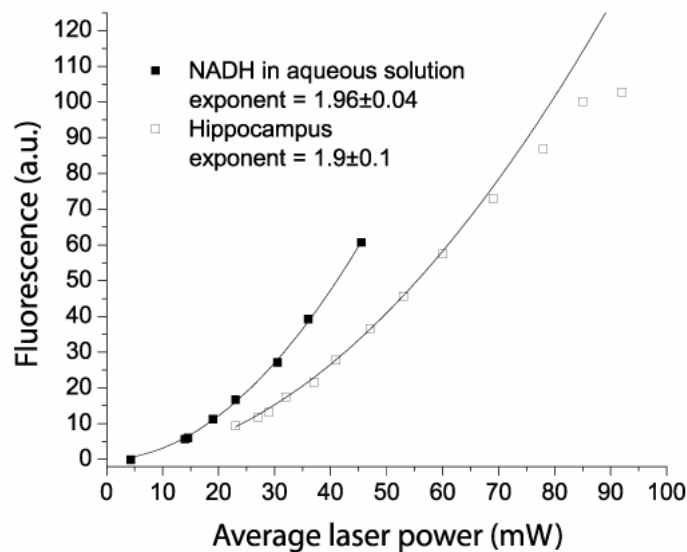


Figure 3.11 Power dependence of aqueous NADH fluorescence and intrinsic fluorescence. The quadratic dependence on excitation power of the fluorescence of aqueous NADH and the intrinsic hippocampal fluorescence reveal a two-photon excitation process. Deviation due to saturation effects does occur at high power however.

Two-photon emission spectra of the intrinsic fluorescence from the CA1 stratum radiatum were compared to the emission spectrum of aqueous NADH (Fig.3.12). The 2P-emission maximum of aqueous NADH is ~ 460 nm at pH 7.4 while the tissue spectrum consists of two distinct peaks. The blue peak, which dominates ($\sim 90\%$) the tissue fluorescence, is blue shifted (by ~ 8 nm) with respect to aqueous

NADH. The yellow peak (at 560-570nm) is likely due to flavins (19,20). Upon hypoxia, we found that the blue peak was enhanced by ~44% while the yellow peak actually decreased in amplitude by ~34% (Fig.3.13).

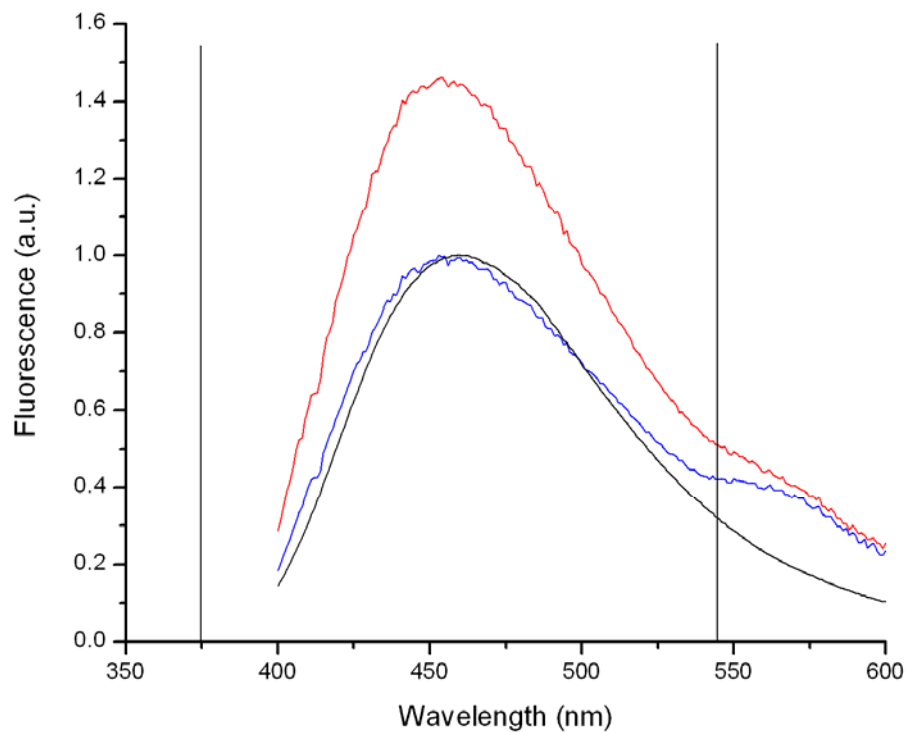


Figure 3.12 Spectroscopic identification of intrinsic NADH. Steady state wavelength resolved fluorescence spectra from normoxic (blue) and hypoxic (red) brain slices strongly resemble the spectrum from aqueous NADH (black). There is, however a slight blue shift of the tissue spectrum and a yellow flavin peak. The vertical lines are the bounds of our emission filter to select the blue peak.

This is consistent with the known inverse behavior of flavin and NADH fluorescence signals in response to hypoxia (18,21). FAD^+ (fluorescent) in complex 1 of the ETC accepts reducing equivalents ($\text{H}^+ + 2\text{e}^-$) from mitochondrial NADH, generating FADH_2 (non-fluorescent) and in turn passing those reducing equivalents

down the ETC - ultimately to oxygen. With the withdrawal of oxygen, there is an accumulation of the non-fluorescent FADH_2 and hence the flavin fluorescence is reduced. In practice, we select our emission filters to reduce the flavin contribution to the integrated fluorescence to $<4\%$ in the normoxic state and $<1\%$ in the hypoxic state.

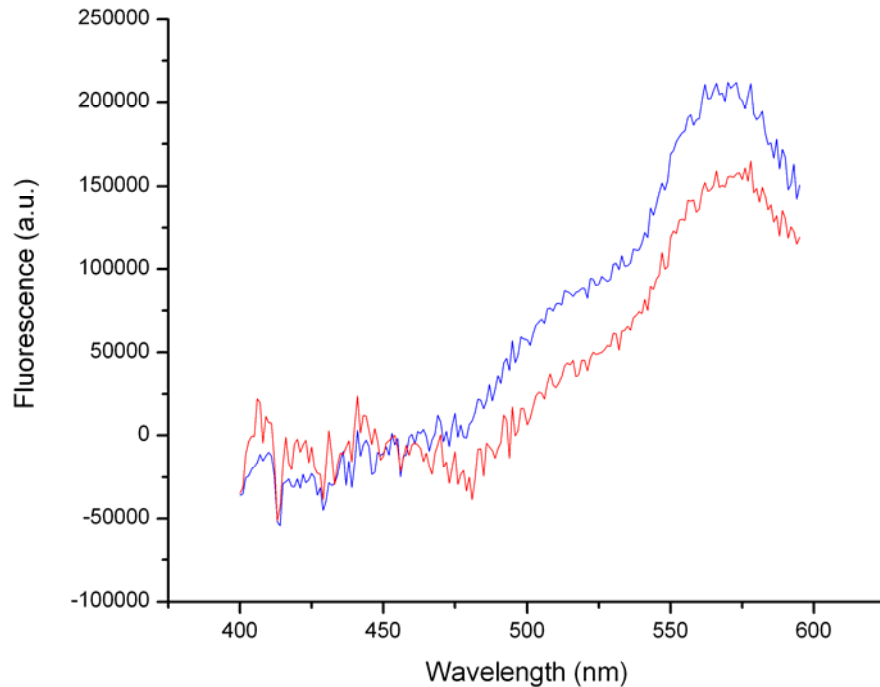


Figure 3.13 Response of the yellow tissue fluorescence to hypoxia. The normoxic yellow fluorescence peak (blue) from a brain slice decreases upon hypoxia (red). This behavior and its emission peak are consistent with this component arising from flavins.

The blue peak of the intrinsic fluorescence spectrum is blue shifted with respect to aqueous NADH. This can be explained by the effect of enzyme-binding on NADH fluorescence. Enzyme binding has the effect of enhancing and blue shifting the fluorescence of NADH. To demonstrate the effect of enzyme binding on NADH fluorescence, we titrated NADH against mitochondrial malate dehydrogenase

(mMDH) – a mitochondrial NADH binding enzyme. The titration of NADH (10 μ M) with increasing concentrations of mMDH resulted in a 2.2 fold fluorescence enhancement, accompanied by a 13 nm blue shift of the emission peak (Fig.(3.14), solid squares).

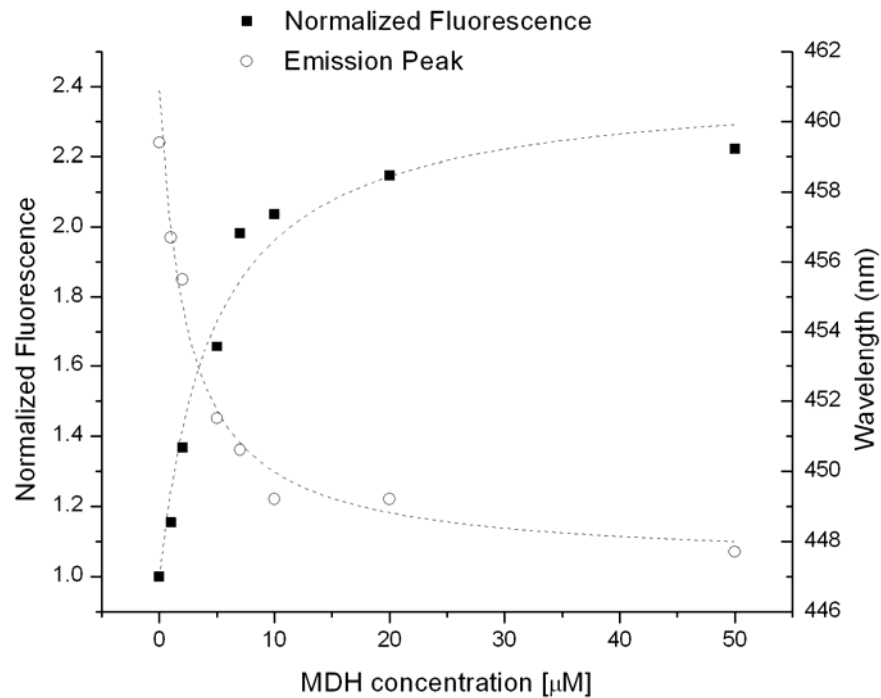


Figure 3.14 Effect of enzyme binding on NADH fluorescence. Binding to mitochondrial malate dehydrogenase causes an enhancement and a blue shift of NADH fluorescence.

The titration also yields a dissociation constant of $\sim 4.7 \mu\text{M}$ at pH 7, in reasonable agreement with an earlier report ($\sim 3.8 \mu\text{M}$ at pH 7.5) (22). There are many intracellular NADH binding dehydrogenases and each produces its own specific fluorescence enhancement (up to 10x) and blue shift (up to $\sim 30\text{nm}$, (19)) due to specific interactions between the fluorescent nicotinamide ring and neighboring groups in the binding site. The measurement summarized in Fig.(3.14) shows that the

~8nm blue shift of the intracellular fluorescence spectrum with respect to the aqueous NADH spectrum can be readily accounted for by the enzyme binding of intracellular NADH.

The exact fraction of intracellular NADH that is bound to enzymes is a question of some uncertainty. While others have estimated that intracellular NADH is almost completely bound to enzymes (23), we will present evidence in Chapter 5 that the fraction of free NADH is indeed significant. However, there is general agreement that, due to the large fluorescence enhancement caused by enzyme binding, the majority of cellular NADH fluorescence is from NADH bound to cytosolic and mitochondrial dehydrogenases.

3.3 Intrinsic fluorescence in astrocytes versus neuropil

3.3.1 Glial cells in the hippocampus

There are roughly twice as many glial cells in the central nervous system as there are neurons, and their distribution amongst the different regions of the brain is highly heterogeneous. Glial cells are morphologically and functionally distinct from neurons. In the hippocampus, the primary glial types are astrocytes and microglia. Microglia act as the brain's immune system and are not of particular interest in this work. Astrocytes on the other hand are intimately involved with mediating the flow of metabolites from capillaries to neurons and with bearing the metabolic cost of neural activity. In light of the particular importance of astrocytes to neurometabolic coupling, it is worthwhile to explore the ability to distinguish them by their intrinsic fluorescence.

Images of the intrinsic fluorescence in the hippocampus reveal astrocytes as bright, stellate cells with cell bodies much smaller (~10 μ m) than those of neurons (Fig.3.15).

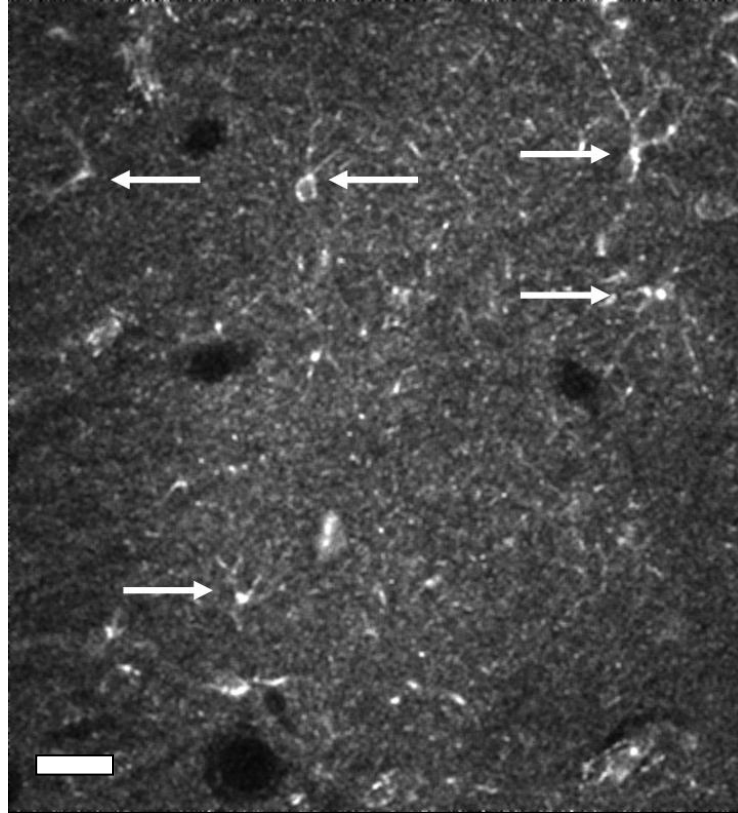


Figure 3.15 Intrinsic fluorescence image showing glia in the neuropil. Bright, small, stellate astrocytes are indicated by arrows in the SR of the hippocampal CA1 layer. Scale bar is 40 μ m.

Typically, only the astrocyte body and its proximal processes are discernible from the surrounding neuropil, while the finer processes cannot be distinguished. These cells appear scattered rather sparsely throughout the neuropil. Walz & Lang used immunolabelling of astrocytes to estimate their numerical density in the CA1 stratum radiatum to be $43.3 \times 10^3 \text{ mm}^{-3}$ (24). This numerical density corresponds to ~ 1 astrocyte per $100 \times 100 \mu\text{m}$ image region (assuming $\sim 2 \mu\text{m}$ depth of focus), in good agreement with our NADH images. Astrocyte numerical densities are region specific within the hippocampus and vary by a factor of ~ 2 in the CA1 layer, with the highest

density being in the dendritic arbor (stratum lacunosum-moleculare) and the lowest being in the cell layer itself (stratum pyramidale) (25).

3.3.2 NADH fluorescence in GFAP-GFP labeled astrocytes

Glial fibrillary acidic protein (GFAP) is a type of intermediate filament unique to astrocytes – however not staining all astrocytes. Based on co-staining with other astrocyte specific molecules Ogata & Kosaka (25) estimated that ~80% of identifiable astrocytes in the CA1 are GFAP(+). Furthermore, comparing GFAP stained astrocytes to golgi-stains revealed that GFAP poorly stains the rather extensive astrocytic arbor. A transgenic strain of mice expressing green fluorescent protein (GFP) under the control of a GFAP (26) promoter (Jasckson Labs, Strain: FVB/N-Tg(GFAPGFP)14Mes/J) enables the identification of astrocytes in living, unfixed tissue by their GFP fluorescence. By imaging both the GFP and NADH fluorescence, we can characterize the NADH fluorescence of identifiable astrocytes in comparison to the surrounding neuropil. Figure (3.16) shows the GFP fluorescence within a hippocampal slice from a GFAP-GFP transgenic mouse. The astrocyte bodies are scattered sparsely throughout the neuropil, with each body having a diffuse ‘halo’ of GFP fluorescence around it. This diffuse region represents the fine, sub-resolution arbors of the astrocytes. These arbors are known to divide the stratum radiatum into domains that overlap only slightly (25).

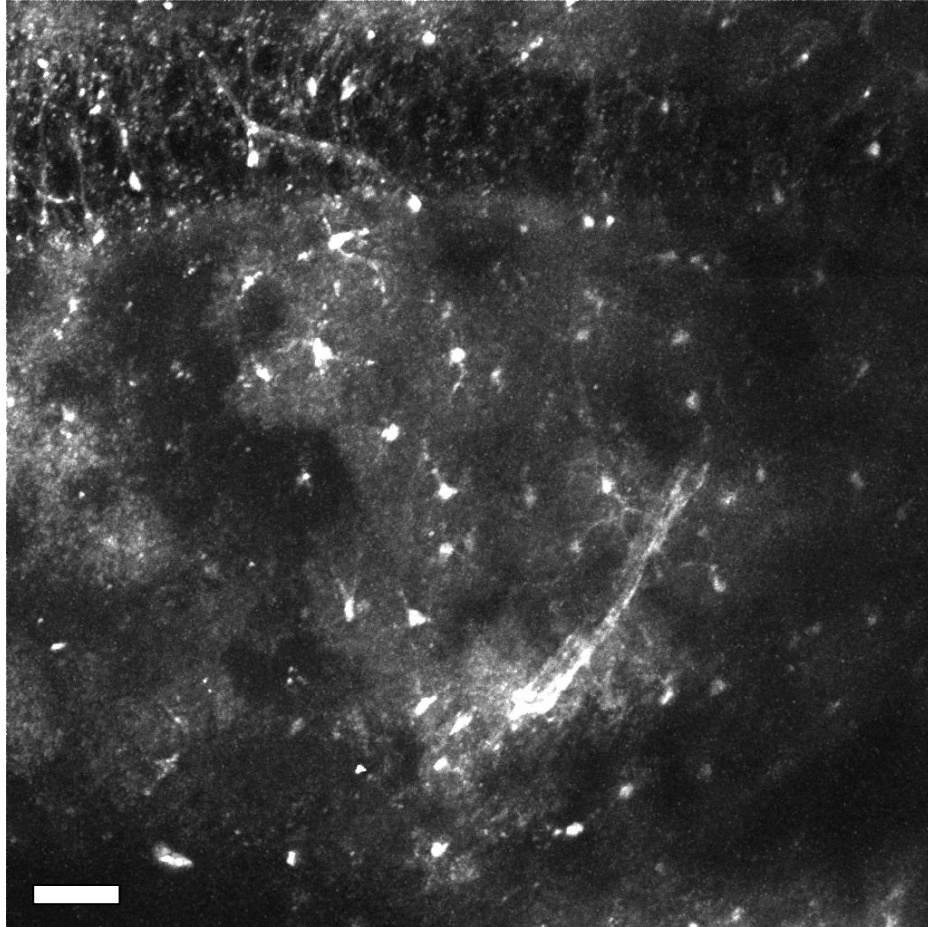


Figure 3.16 GFP labeled astrocytes in a transgenic mouse hippocampus. This z-projection shows GFP labeled astrocytes in the hippocampal CA1-CA3 are sparsely scattered and tend to divide the neuropil into regions of influence or domains. Scale bar is 50 μ m.

Images of both the NADH and GFAP-GFP signal from such a slice reveal that astrocytes that are easy or moderately easy to identify by their NADH fluorescence and morphology are also revealed by the GFAP-GFP signal (Figs.(3.17A-B,D-E). However there are also astrocytes revealed by GFAP-GFP that are indistinguishable from the surrounding neuropil by their NADH signal (Fig.(3.17C,F)). It is also clear from Figs.(3.17A and B) that while the NADH fluorescence may reveal the bodies and proximal processes of astrocytes, the somewhat finer distal processes revealed by the

GFAP-GFP image are impossible to distinguish from the surrounding neuropil based on the NADH fluorescence. This is likely due to the exceedingly small width of the distal processes.

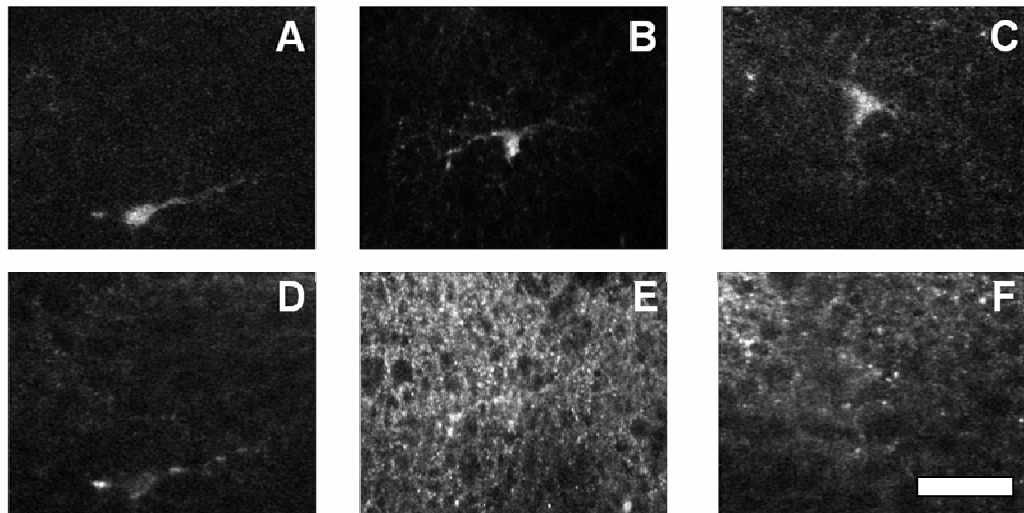


Figure 3.17 Identification of astrocytes by GFAP-GFP and NADH. Images of astrocytes using GFAP-GFP fluorescence (top row) and the corresponding NADH fluorescence (bottom row, arranged under corresponding GFAP-GFP image). Some astrocytes are easy to identify by their NADH fluorescence (D), some are moderately difficult (E) and some are very difficult (F). Scale bar is 40 μ m.

A fixed tissue slice immunostained with GFAP (astrocytes), cytochrome oxidase (mitochondria) and DAPI (nuclei) (7) reveals (via GFAP) that astrocytes have fine distal processes (<1 μ m) that are at the limit of the spatial resolution (Fig.3.18).

Recall also that GFAP is not a good indicator of the smallest processes in the astrocytic arbor, there is in fact a substantial arbor of fine processes surrounding the astrocytic soma that are at or below our spatial resolution (25). This implies that the neuropil is a combination of neuronal axo-dendritic network and astrocytic processes that cannot be morphologically differentiated by their NADH fluorescence. The exception is the astrocytic somata and proximal processes.

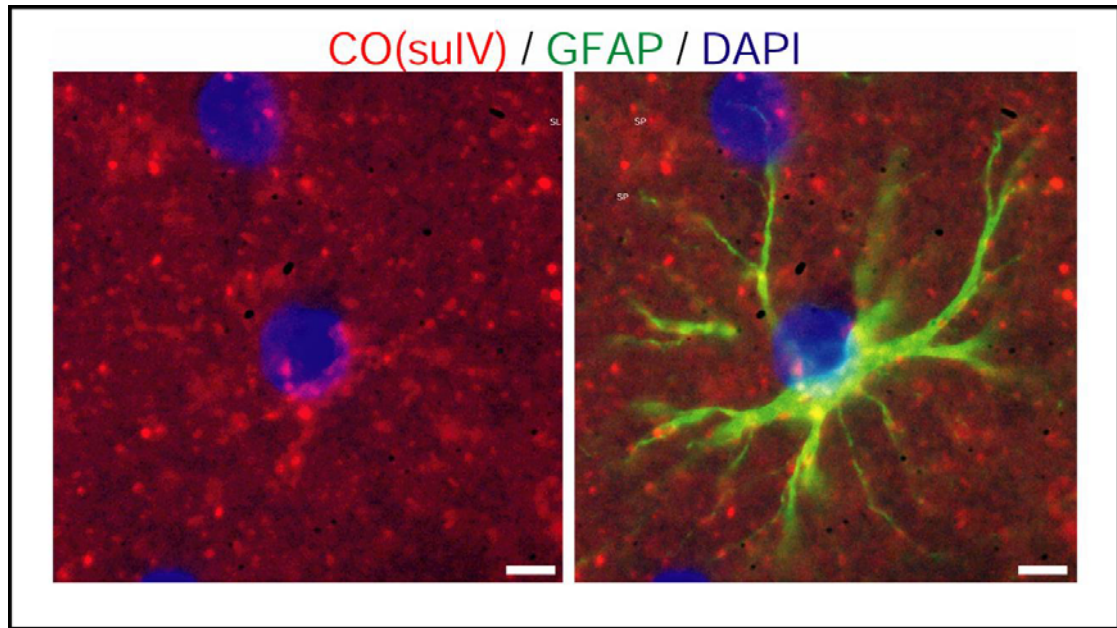


Figure 3.18 Immunostain for GFAP in fixed brain tissue. Immunostain for GFAP (green) marks astrocytes, cytochrome oxidase (CO, red) marks mitochondria and DAPI (blue) marks nuclei. The GFAP stain reveals very fine astrocytic processes. Scale bar is 10 μ m.

The average intrinsic fluorescence intensity of astrocytes is somewhat higher than the neuropil surrounding it. Fig.(3.19) shows a two-dimensional histogram (or scatter density plot) of the pixel intensities of an NADH image the corresponding GFAP-GFP image (in this case Fig.(3.17A)).

There is a clear correlation between GFAP-GFP and NADH intensity. Pixels with a high GFAP-GFP intensity (astrocytes) have a more intense NADH intensity. However, the distributions of NADH intensity associated with low and high GFAP-GFP intensities are wide and overlap significantly. This is a reflection of the fact that high GFAP-GFP regions (astrocytes) have a high NADH intensity in the cell bodies/proximal processes and a lower NADH intensity in the distal processes. Very low GFAP-GFP intensity pixels (neuropil) contain both mitochondria and cytosol – giving high and low NADH intensity respectively.

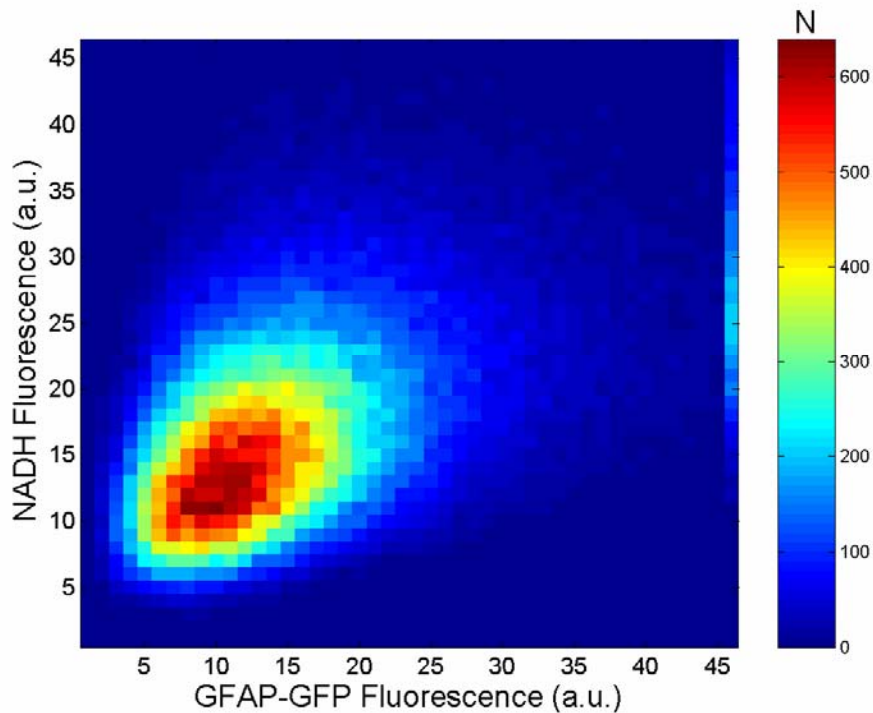


Figure 3.19 NADH fluorescence versus GFAP-GFP fluorescence around a typical astrocyte. While this 2D histogram (or scatter density plot) reveals a definite correlation between GFAP-GFP and NADH intensity around an astrocyte, this correlation is loose due to distal astrocytic processes with low NADH intensity.

In summary, astrocyte cell bodies and proximal processes can be identified by their morphology and elevated NADH intensity. The surrounding neuropil however contains distal astrocytic processes that are at or below our spatial resolution and that cannot be distinguished from the surrounding neuropil.

3.4 Conclusions

Biological tissues contain a number of intrinsic fluorophores. It is possible to select an excitation wavelength and emission filter to selectively excite and detect NADH. Under these conditions, pharmacological, morphological and spectroscopic evidence identifies the intrinsic fluorescence from the hippocampal brain slice as

predominately NADH. This intrinsic fluorescence does potentially contain contaminating signals from NADPH and retinoids that cannot be spectrally excluded. These molecules however are not only present at much lower concentrations than NADH, but they also represent a largely metabolically inert background that does not significantly contribute to metabolism linked fluorescence changes.

The morphology of the intrinsic fluorescence in the hippocampus allows a clear, unambiguous recognition of neuronal and astrocytic somata and proximal processes. The bright, small, roughly circular spots present throughout the hippocampus in varying densities are shown by Rh123 stains to be largely mitochondria. Furthermore, GFAP-GFP images reveal that astrocytes in the neuropil also have a high NADH fluorescence in their bodies and proximal processes. While the bright mitochondrial and astrocytic fluorescence is comparable in intensity, these compartments are easily distinguished by their morphology. On the other hand, the dim distal processes of astrocytes are sub-resolution and cannot be distinguished from the surrounding neuropil. With the fluorescence and morphological characteristics of these cellular and sub-cellular compartments in mind, we are in a good position to begin imaging neuro-metabolic dynamics in response to metabolic effectors.

References

1. Lakowicz, J. R. (1999) *Principles of Fluorescence Spectroscopy*, 2 Ed., Kluwer Academic/Plenum Publishers
2. Kierdaszuk, B., Gryczynski, I., Modrakwojcik, A., Bzowska, A., Shugar, D., and Lakowicz, J. R. (1995) *Photochemistry and Photobiology* **61**, 319-324
3. Zetterstrom, R. H., Lindqvist, E., de Urquiza, A. M., Tomac, A., Eriksson, U., Perlmann, T., and Olson, L. (1999) *European Journal of Neuroscience* **11**, 407-416
4. Takahashi, J., Palmer, T. D., and Gage, F. H. (1999) *Journal of Neurobiology* **38**, 65-81
5. Misner, D. L., Jacobs, S., Shimizu, Y., de Urquiza, A. M., Solomin, L., Perlmann, T., De Luca, L. M., Stevens, C. F., and Evans, R. M. (2001) *Proceedings of the National Academy of Sciences of the United States of America* **98**, 11714-11719
6. Zipfel, W. R., Williams, R. M., Christie, R., Nikitin, A. Y., Hyman, B. T., and Webb, W. W. (2003) *Proceedings of the National Academy of Sciences of the United States of America* **100**, 7075-7080
7. Kasischke, K. A., Vishwasrao, H. D., Fisher, P. J., Zipfel, W. R., and Webb, W. W. (2004) *Science* **305**, 99-103
8. Morjani, H., Beljebbar, A., Sockalingum, G. D., Mattioli, T. A., Bonnier, D., Gronemeyer, H., and Manfait, M. (1998) *Biospectroscopy* **4**, 297-302
9. Yin, D. Z. (1996) *Free Radical Biology and Medicine* **21**, 871-888
10. Oenzil, F., Kishikawa, M., Mizuno, T., and Nakano, M. (1994) *Mechanisms of Ageing and Development* **76**, 157-163
11. Dombeck, D. A., Kasischke, K. A., Vishwasrao, H. D., Ingelsson, M., Hyman, B. T., and Webb, W. W. (2003) *Proceedings of the National Academy of Sciences of the United States of America* **100**, 7081-7086
12. Joubert, F., Fales, H. M., Wen, H., Combs, C. A., and Balaban, R. S. (2004) *Biophysical Journal* **86**, 629-645
13. Klingenberg, M., and Bucher, T. (1960) *Annual Review of Biochemistry* **29**, 669-708
14. Visser, A., and Vanhoek, A. (1981) *Photochemistry and Photobiology* **33**, 35-40

15. Klaidman, L. K., Leung, A. C., and Adams, J. D. (1995) *Analytical Biochemistry* **228**, 312-317
16. Avidor, Y., Doherty, M. D., Olson, J. M., and Kaplan, N. O. (1962) *Journal of Biological Chemistry* **237**, 2377-&
17. Chance, B., Williams.Jr, Jamieson, D., and Schoener, B. (1965) *Biochemische Zeitschrift* **341**, 357-&
18. Scholz, R., Thurman, R. G., Williams.Jr, Chance, B., and Bucher, T. (1969) *Journal of Biological Chemistry* **244**, 2317-&
19. Velick, S. F. (1961) in *A Symposium on Light and Life* (McElroy, W. D., and Glass, B., eds), pp. 108-143, The Johns Hopkins Press, Baltimore, MD
20. Benson, R. C., Meyer, R. A., Zaruba, M. E., and McKhann, G. M. (1979) *Journal of Histochemistry & Cytochemistry* **27**, 44-48
21. Franke, H., Barlow, C. H., and Chance, B. (1979) *International Journal of Biochemistry* **10**, R2-R2
22. Shore, J. D., Evans, S. A., Holbrook, J. J., and Parker, D. M. (1979) *Journal of Biological Chemistry* **254**, 9059-9062
23. Chance, B., and Baltscheffsky, H. (1958) *Journal of Biological Chemistry* **233**, 736-739
24. Walz, W., and Lang, M. K. (1998) *Neuroscience Letters* **257**, 127-130
25. Ogata, K., and Kosaka, T. (2002) *Neuroscience* **113**, 221-233
26. Zhuo, L., Sun, B., Zhang, C. L., Fine, A., Chiu, S. Y., and Messing, A. (1997) *Developmental Biology* **187**, 36-42

Chapter Four

Imaging In Vivo NADH Dynamics

4.1 Motion correction

Two-photon fluorescence microscopy offers a high spatial resolution in both the axial and lateral directions. Imaging with this resolution offers the opportunity to study NADH dynamics in sub-cellular compartments that are not accessible in living tissue with other fluorescence techniques. The NADH response in tissue to a particular influence e.g metabolic inhibition or metabolic load, is measured by acquiring a time series of fluorescence images during which that influence is brought to bear. Monitoring the spatial heterogeneity of the response of the tissue is then simply a matter of monitoring the intensity change of each pixel separately.

However, following the intensity of a particular pixel through the time series, and interpreting the intensity change in a biologically meaningful way assumes that pixel corresponds to the same region of the tissue in each time frame. This is not true if the position of the tissue changes between subsequent images. For example pixel (100,100) may correspond to a mitochondrion in one image, and in the next image

correspond to a cytosolic region due to physical motion of the slice. In this case, the change in the intensity of pixel (100,100) is misleading, as it is simply an artifact of motion and not a genuine change in the NADH level of a sub-cellular compartment. Clearly it is desirable to do a pixel-by-pixel analysis of an image time series as this takes advantage of the spatial resolution of TPM to resolve differences in the responses of different tissue regions. Doing so however requires a means to correct for the motion of the sample.

Motion elimination is a two step process. The first step is hardware based: brain slices in perfusion chambers are usually suspended between nylon meshes, as has been previously discussed in Section (2.5.3). While these meshes prevent large motions of the tissue, small jitters and drifts are inevitable due to turbulence in the perfusate flowing through the chamber. The second step is a software based correction for small jitters and drifts of the slice that is applied as part of the post-processing. The software correction is presented below.

4.1.1 Strategy for motion correction

The general algorithm for motion correction is outlined in Figure (4.1). Consider a sequence of N images ($I(\mathbf{r},t)$, $t=1$ to N) of an object that is moving such that its motion between any two given images is small ($\Delta x, \Delta y \leq 10$ pixels), and its total range of motion is smaller than the total x-y size of an image. The process of correcting for its motion begins by considering each sequential pair of images, $I(\mathbf{r},n)$ and $I(\mathbf{r},n+1)$. $I(\mathbf{r},n+1)$ is offset in the x and y directions ($I(\mathbf{r},n+1) \rightarrow I(\mathbf{r}+\Delta\mathbf{r},n+1)$) until its similarity to $I(\mathbf{r},n)$ is maximized. The similarity of two images can be measured in a number of different ways, and these will be considered in the next section. The offset that maximizes similarity is known as the shift vector ($\Delta\mathbf{r}_{n+1,n}$) for that pair of images and gives us the number of pixels in x and y that the sample has shifted between image

n and image $n+1$. Correcting for this shift simply involves offsetting image $n+1$ by the negative of the shift vector. By correcting each image with respect to the one preceding it, we can motion correct the entire image series.

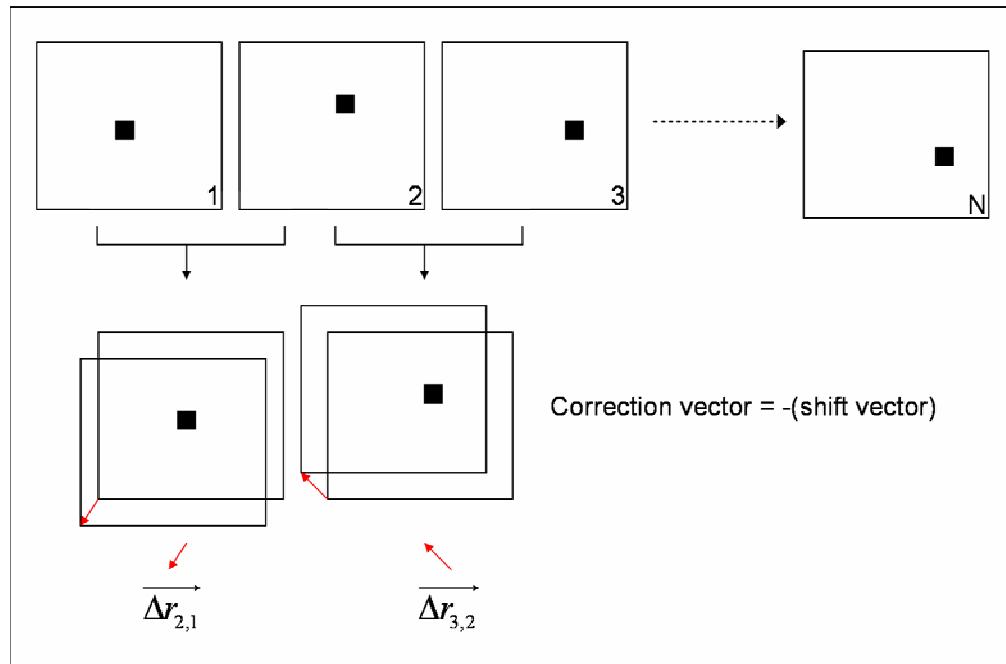


Figure 4.1 Strategy for motion correction. Motion correction is done by a pairwise comparison of images in the time series. Each sequential pair is relatively shifted by some ‘shift vector’ until the similarity is maximized.

4.1.2 Measures of image similarity

The similarity between two successive images in a series can be measured with a number of quantities. We used the linear correlation coefficient, the chi-squared and the overlap integral as parameters of varying robustness and computational complexity. One of the most common parameters used to measure image similarity is the correlation coefficient (Eqn.(4.1)).

$$r(t) = \frac{\sum_x \sum_y (I(\mathbf{r}, t) - \overline{I(\mathbf{r}, t)})(I(\mathbf{r}, t+1) - \overline{I(\mathbf{r}, t+1)})}{\sqrt{\left(\sum_x \sum_y (I(\mathbf{r}, t) - \overline{I(\mathbf{r}, t)})^2 \right) \left(\sum_x \sum_y (I(\mathbf{r}, t+1) - \overline{I(\mathbf{r}, t+1)})^2 \right)}} \quad (4.1)$$

Where $\overline{I(\mathbf{r}, t)}$ is the average value of $I(\mathbf{r}, t)$.

This function has higher values for more correlated images, with a maximum value of 1 for identical images, hence maximizing similarity entails maximizing the correlation coefficient. While this is a robust measure of similarity, correcting the relative offset of two images using this measure was found to take a long time due to the complexity of the calculation. For example, a typical pair of 200x200 pixel images, required more than 10s to motion correct.

Another parameter to estimate similarity that is somewhat simpler in the number of separate calculations required, is the chi-squared, defined by Eqn.(4.2).

$$\chi^2(t) = \sum_x \sum_y \frac{(I(\mathbf{r}, t) - I(\mathbf{r}, t+1))^2}{I(\mathbf{r}, t) + I(\mathbf{r}, t+1)} \quad (4.2)$$

The chi-squared, as usual, requires minimization to give maximum similarity. This parameter required some degree of thresholding to be effective for motion correction, i.e. very low intensity pixels were not included in the calculation of the parameter since they exhibit large fractional changes in their intensity (shot noise). However, only the ~20% lowest intensity pixels needed to be excluded, and adjusting the threshold beyond that had little effect. The chi-squared, being computationally more simple than the correlation, required only ~5s to correct a 200x200 pixel image pair for motion.

The final parameter – the overlap integral – is the least computationally complex parameter and therefore is the fastest to execute. There are objects in a brain

slice such as astrocytes, astrocytic mitochondria and blood vessels that are always bright (with respect to the average of the slice) regardless of the metabolic condition of the surrounding slice. The overlap integral method uses a threshold to isolate these bright structures and uses them as landmarks whose motion is an indicator of the motion of the slice. This protocol is illustrated in Fig.(4.2) on a typical pair of images from a time series.

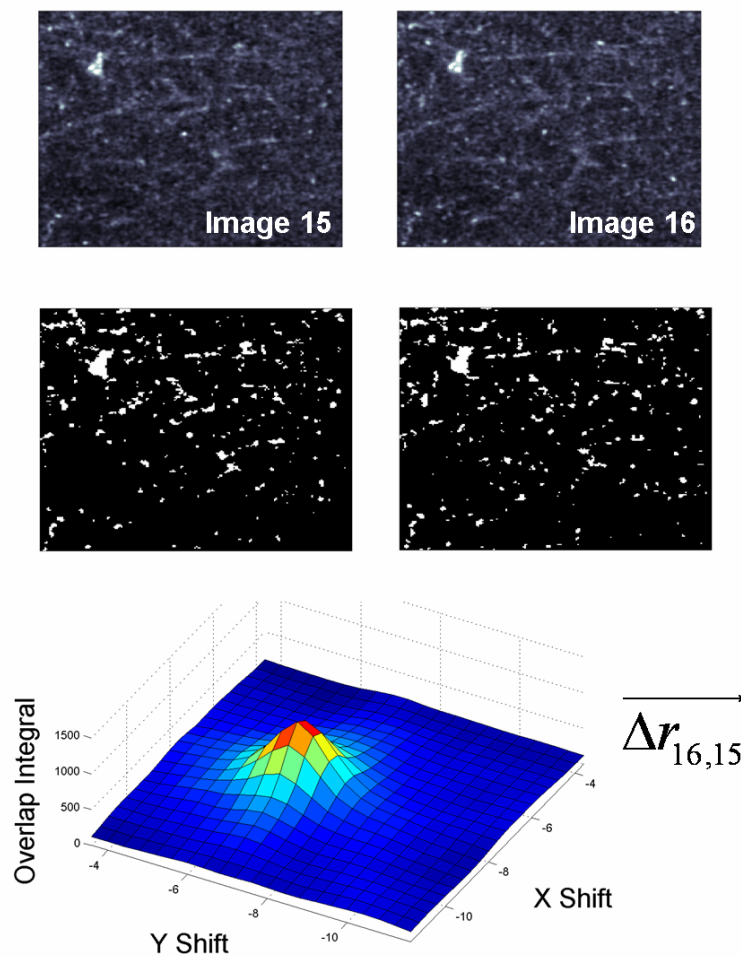


Figure 4.2 Pairwise calculation of relative shift vector. A pair of consecutive images (top row) are thresholded to generate binary masks (second row, red = 1, blue=0). The overlap integral (bottom row) of the masks is calculated as a function of x shift and y shift, and its maximum is taken as the shift vector Δr .

For both images $I(\mathbf{r},t)$ and $I(\mathbf{r},t+1)$, threshold masks $M(\mathbf{r},t)$ and $M(\mathbf{r},t+1)$ are generated. The threshold mask is an array of size equal to the image. Each pixel of the threshold mask has a value depending on the value of the corresponding pixel of the image. If the image pixel value is greater than the specified threshold (T), then the corresponding mask pixel is set to 1, otherwise it is set to 0. That is: $M(\mathbf{r},t) = 1$ if $I(\mathbf{r},t) > T$, $M(\mathbf{r},t) = 0$ if $I(\mathbf{r},t) \leq T$. The threshold for each image is chosen so that only the most intense pixels ($\sim 1-5\%$ of the total pixel number) are represented in the mask.

Once the masks are generated, these masks are used in place of the images to do the maximization of similarity and thereby get the shift vectors. Since the masks are logical arrays of 1s and 0s, we can define a simple overlap integral (Eqn.(4.3)) to measure their similarity. The overlap integral essentially counts the number of 1s that overlap between the two masks.

$$O(t) = \sum_x \sum_y M(\mathbf{r},t) \cdot M(\mathbf{r},t+1)$$

or

$$O(t) = \sum_x \sum_y M(\mathbf{r},t) \wedge M(\mathbf{r},t+1) \tag{4.3}$$

(\wedge is the AND operator)

This process is a simple threshold discrimination followed by an AND operation and an integration, and is therefore not only the fastest means of motion correction considered here (time per pair $\sim 3s$) but is also potentially easily adapted to real-time motion correction as level discrimination, logical operations and integration are very rapidly executed by hardware. It should be noted that all the process times quoted here are specific to program execution in Matlab, and are expected to be substantially shorter if compiled into an executable program.

Since the overlap integral method actually uses the threshold masks to get the shift vectors, its efficacy is very sensitive to the threshold level and structure of the image. This method provides the best results when there are obvious small, bright regions in the tissue – which is the case for most high resolution brain slice images. When a high intensity threshold is applied to such an image, the result is a sparse field of small spots which are easily tracked from one image to the next. Images which are more homogenous in appearance (e.g. low magnification, or low resolution) are better dealt with using the chi-squared method. However, given the structure of brain tissue, the overlap integral is our method of choice for motion correction in high resolution image series.

Table 4.1 Summary of measures of image similarity.

Measure	Advantage	Disadvantage
Correlation	Requires no threshold to be accurate.	Long calculation time (>10s per image pair)
Chi Squared	Accuracy not very sensitive to threshold.	Better calculation time, but still long (~5s per pair)
Overlap Integral	Fastest calculation time (~3s per pair)	Accuracy sensitive to threshold. Requires defining a mask. Works best in presence of small punctate bright spots.

4.1.3 Extrapolating motion correction from an image pair to an image series

Motion correction is done only between two sequential images, as opposed to correcting each image with respect to a baseline image early in the time series. We do this as images later on in the time series may have undergone significant physiological changes as a result of metabolic manipulations during the time series. Because of these

changes, a late image may be sufficiently different from an early one that it is difficult to compare them to get an exact measure of the relative shift. In contrast, there are usually only slight changes between sequential images, and hence they can more readily be compared to correct for motion between them.

The shift vector ($\Delta\mathbf{r}$) for every sequential image pair in the series provides the position of every image with respect to its immediate predecessor. Hence the position of image n (\mathbf{r}_n) with respect to the first image (taken as $(0,0)$) is the cumulative sum of shift vectors up to that image (Eqn.(4.4)).

$$\mathbf{r}_n = \sum_{i=1}^{n-1} \Delta\mathbf{r}_i \quad (4.4)$$

Each image is then moved by the negative of its position vector with respect to the first image. In effect, this is tantamount to transferring the motion of the specimen to the motion of the frame; causing the physical structures in the specimen to remain in the same place while the frame moves around.

4.1.4 Reduction of motion artifact

While the overlap integral is a fast and practical means of motion correction, we return to the more robust correlation coefficient to study the effect of motion and motion correction as a function of the time difference between images (ΔT ; expressed as frames, each frame = 5-60s depending on the experiment). In general, for a motion corrected sample, the amplitude of the correlation decay (at $\Delta T=1$) is a function of spontaneous intensity fluctuations (shot noise). Since there is little motion between immediately successive images, variations in pixel intensities are dominated by noise, which is reflected in the initial amplitude of the correlation decay. On the other hand, if each pixel only randomly fluctuated about its own constant mean value, then the

correlation would not decay with time. The decay of the correlation is due to residual motion (x, y and z) of the sample that could not be corrected for, and represents a limiting factor on the length of a time for which a given pixel can be said to be monitoring the same physical structure.

A typical uncorrected time series shows a correlation coefficient that drops rapidly from a peak value of ~ 0.68 to ~ 0.3 within 12 frames (Fig.(4.3a), blue). After motion correction (red curve), the correlation has a higher peak value (0.75) and drops much more slowly, leveling off at a value of ~ 0.55 after 17 frames. The slower decay indicates that significant overlap between images is maintained for much longer than in the uncorrected time series.

The motion correction in this case was done using the overlap integral method. Instead, if we use the chi-squared method, we obtain a correlation decay which is virtually identical to that obtained with the overlap integral method (Fig.(4.3b)). Hence we see that using the chi-squared parameter to quantify image similarity does not necessarily yield a better motion correction and takes more time to do the correction.

The overall amplitude of the correlation is reduced by spontaneous temporal fluctuations in pixel intensities (shot noise). These fluctuations can be reduced by smoothing each pixel with a temporal Gaussian 3 filter – which performs a weighted average of the value of each pixel in an image with its value in the image immediately prior and immediately following the image. It is important that motion correction be done prior to temporal smoothing, since before motion correction, the same pixel in sequential images can correspond to different physical structures. Temporal smoothing reduces shot noise and therefore shifts the entire correlation decay curve up (Fig.4.3c), yielding a peak value of ~ 0.93 (recall the theoretical maximum is 1). This exceedingly

high correlation for $\Delta T=1$ indicates that immediately sequential images are, on average, essentially identical.

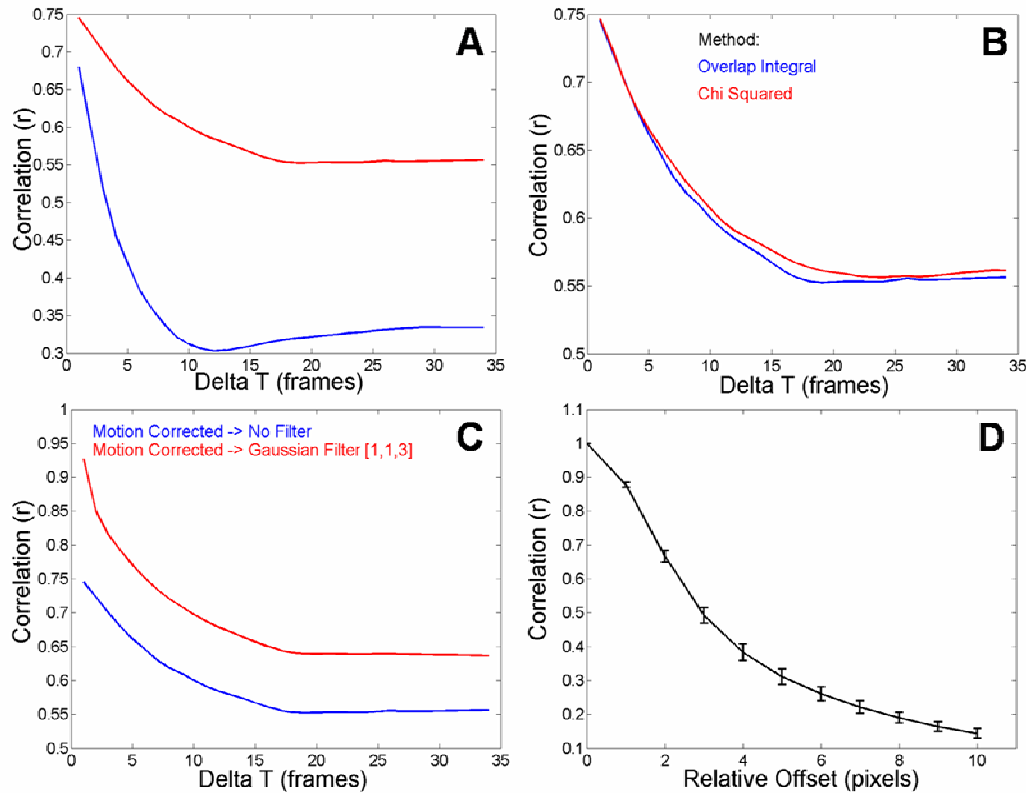


Figure 4.3 Correlation decays show motion correction reduces motion artifact. (A) Image series temporal correlation decay before motion correction (blue) and after (red). (B) The post-correction correlation is not greatly affected by the choice of image similarity parameter. (C) Temporal smoothing increases the correlation amplitude but not the decay time. (D) Spatial autocorrelation reveals the spatial shift corresponding to a particular value of correlation.

To understand the effect of motion on the correlation decay, we correlate an image with itself offset by a certain number of pixels – a spatial auto-correlation. Fig.(4.3d) shows the averaged spatial auto-correlations for all the images in the time series being considered in this case study. Since an auto-correlation correlates each image with itself, there are no changes in pixel intensity due to shot noise and therefore the correlation amplitude at zero relative offset is unity and the decay is

strictly due to spatial offset. In contrast, sequential images, even if perfectly motion corrected still exhibit shot noise and hence do not give unit correlation amplitude at zero relative offset. The auto-correlation is observed to decay rapidly within only a few pixels of relative offset. We know that mitochondria are on the order of 1-2 microns in width, and hence we would like to restrict our pixel-by-pixel analysis of time series to sections that have less than 0.5-1 micron of motion. In this particular image series, the pixel size is about 0.43 microns, hence a motion of 1.5 microns (a mitochondrion) corresponds to ~ 3.5 pixels. We would like to restrict our consideration to image series that have less than half that motion, i.e. 1.7 pixels, which corresponds to a decrease in the correlation of ~ 0.75 from Fig.(4.3d). From Fig.(4.3c) we see that the correlation is greater than 0.75 up to about $\Delta T=6$, implying that we can take sections of the image series up to 7 ($\Delta T + 1$) frames long and expect that they are correlated to better than half a mitochondrion worth of motion.

4.1.5 Post motion correction artifact in intensity based region of interest selection: difference-intensity anti-correlation

Once motion correction is done, it is possible to follow the intensity changes in pixel sub-populations of the image, known as regions of interest (ROIs). Assigning physical significance to intensity changes assumes that their baseline changes are zero on average. However, if we calculate the pixel-by-pixel difference between a typical consecutive image pair ($D(x,y,t) = I(x,y,t+1) - I(x,y,t)$) that are part of the baseline phase of the time series, we find that while the average difference ($\langle D(x,y,t) \rangle$) is in fact approximately zero, a scatter plot of the difference versus the initial intensity (Fig.(4.4a)) reveals a negative correlation between the two. Low intensity pixels tend to increase in intensity while high intensity pixels tend to decrease in intensity.

Averaging the differences over ranges of initial intensities (Fig.(4.4b)) better elucidates this difference-intensity anti-correlation.

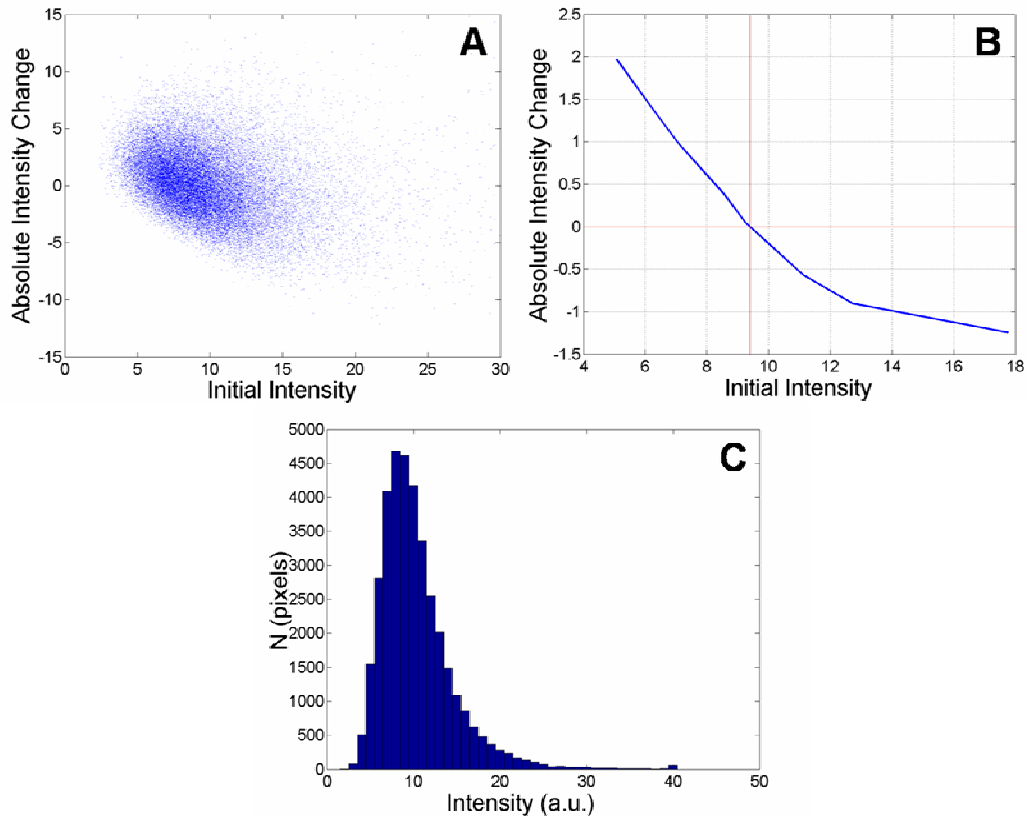


Figure 4.4 Difference-intensity anti-correlation. (A) Scatter plot of the initial intensities of baseline phase pixels versus their intensity changes. (B) Averaging the scatter in (A) into intensity bins elucidates the dependence. (C) The intensity histogram of the initial image which gave rise to the spontaneous changes plotted in (A and B).

This particular effect is a consequence of the shape of the intensity histogram of the image. When pixels of a specific intensity range – call this the i^{th} intensity bin – are selected in an image, there are actually three populations of pixels that are selected:

1. n_i pixels with a mean intensity within the i^{th} intensity bin whose current value also lies within the i^{th} bin.

2. n_{i+1} pixels with a mean intensity in the next higher $(i+1)^{\text{th}}$ bin but whose intensity at this time point happens to lie in the i^{th} bin due to spontaneous fluctuations.
3. n_{i-1} pixels with a mean intensity in the next lower bin $(i-1)^{\text{th}}$ bin but whose intensity at this time point happens to lie in the i^{th} bin due to spontaneous fluctuations.

The integrated intensity of the selected pixels at time t is then:

$$\int I_i(t) = n_i I_i + n_{i+1} I_i + n_{i-1} I_i \quad (4.5)$$

In the next time frame $(t+1)$, those n_i pixels with a mean intensity in the i^{th} bin will on average have an intensity I_i . Those n_{i+1} pixels that were selected during a spontaneous downward fluctuation will now, on average, fluctuate upwards to their mean intensity of I_{i+1} . Similarly, those n_{i-1} pixels that were selected during a spontaneous upward fluctuation will now, on average, have an intensity of I_{i-1} . The integrated intensity of the selected pixels is then:

$$\int I_i(t+1) = n_i I_i + n_{i+1} I_{i+1} + n_{i-1} I_{i-1} \quad (4.6)$$

The change in the integrated intensity of the selected pixels is:

$$\begin{aligned} & \int I_i(t+1) - \int I_i(t) \\ &= n_{i+1}(I_{i+1} - I_i) - n_{i-1}(I_i - I_{i-1}) \\ &= (n_{i+1} - n_{i-1})\Delta I \\ &= (N_{i+1} - N_{i-1})c\Delta I \end{aligned} \quad (4.7)$$

Here ΔI is the inter-bin intensity interval, and we assume that $n_{i\pm 1}$ are proportional to the total pixel populations of the respective bins $N_{i\pm 1}$ with c being the constant of proportionality. The shape of the image intensity histogram (Fig.(4.4c)) is such that for low intensities, the histogram has a positive slope up to the intensity of the histogram

peak (I_{peak}). For intensities higher than I_{peak} , the slope of the histogram is negative. In other words:

$$\begin{aligned} \text{For } I_i < I_{peak} : \\ N_{i+1} > N_{i-1} &\Rightarrow \int I_i(t+1) - \int I_i(t) > 0 \end{aligned} \quad (4.8)$$

$$\begin{aligned} \text{For } I_i > I_{peak} : \\ N_{i+1} < N_{i-1} &\Rightarrow \int I_i(t+1) - \int I_i(t) < 0 \end{aligned}$$

At the peak of the histogram, $N_{i+1} = N_{i-1}$ and the difference should be zero. This behavior is seen in Fig.(4.4c) where the difference is positive for low intensities, decreases to zero at the intensity of the histogram peak, and becomes negative for higher intensities.

Since the cause of this effect is the spontaneous fluctuation of pixel intensities, reducing fluctuations by applying spatio-temporal smoothing filters should reduce the effect. A number of Gaussian spatio-temporal filters were tried. These filters have binning factors given by $[n_x \ n_y \ n_t]$, e.g. $[3 \ 3 \ 1]$ refers to a 3x3 spatial filtering with no temporal filtering. The result of applying these filters on the difference versus intensity curve is shown in Fig.(4.5a). The Gaussian $[1 \ 1 \ 3]$ filter – a Gaussian 3 temporal smoothing is highly effective and entails no spatial filtering which reduces spatial resolution and is therefore the smoothing we apply for subsequent analysis.

The difference-intensity anti-correlation effect can also be reduced by increasing the width of the intensity bins, or equivalently, reducing the total number of intensity bins. Increasing the intensity bin width reduces the probability that a pixel will fluctuate out of its intensity bin. Unfortunately, increasing bin width compromises the ability to measure differences in the responses of different intensities. As Fig.(4.5b) shows, drastically reducing the total number of intensity bins to 2 is less

effective than a simple Gaussian 3 temporal filter. For a more reasonable number of bins (5-10), there is little advantage obtained by using fewer bins and hence we do not rely on the number of bins, but rather the smoothing filters to reduce the difference-intensity anti-correlation effect. In practice, we use 5-10 intensity bins.

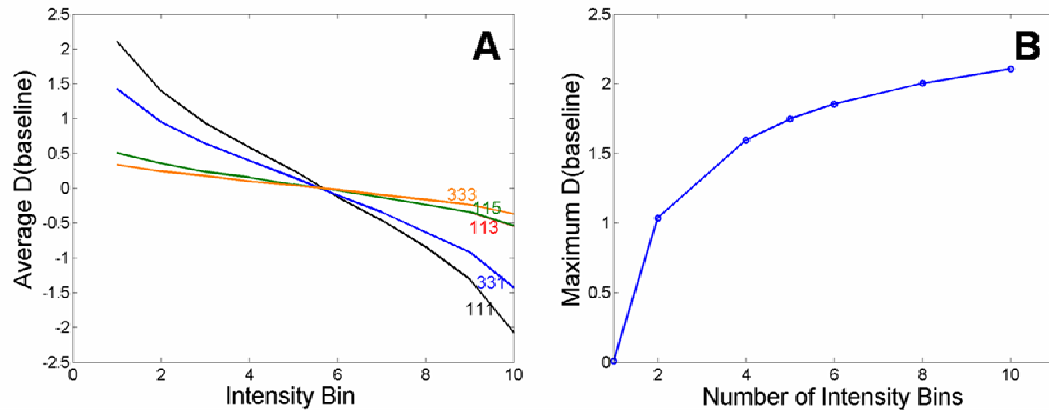


Figure 4.5 Methods of reducing intensity dependent spontaneous intensity changes. (A) Applying Gaussian spatial filters of dimensionality [nx ny nt] smoothes out noise and reduces the magnitude of the intensity dependent intensity change. (B) Alternatively, grouping pixels into of intensity range bins also reduces the artifact.

4.1.6 Limitations of the motion correction protocol

This motion correction program works only for simple x-y linear shifts of the sample. Motions that it cannot accommodate for are: rotation, distortion, z-drift, and morphological alteration. Usually however, for tissue that either rotates or distorts, the tissue image can be divided into smaller regions whose motion can be approximated as linear shifts. In this case, we can consider small regions of the tissue separately and apply this motion correction program to those regions as if they were independent images series. Z-drift correction is not possible at all with this program. In theory, the program could be trivially extended to correct for motion in the z direction – however it would entail acquiring a time series of x-y-z images. This is not currently done in

our experiments. Lastly, it is also possible that genuine morphological changes occur in the tissue during a time series acquisition. Specifically, mitochondria are known to be mobile. This motion is slow and imaging experiments over the course of a few minutes can neglect this motion. Hypoxia experiments however can take 20-30 minutes. During this time it is possible for the mitochondrial distribution to change slightly. This mobility of fluorescent mitochondria represents a changing fluorescence distribution that cannot be corrected. Typically, we deal with this problem by either limiting pixel-by-pixel analyses to time intervals of a couple of minutes, or by measuring average intensity characteristics of large populations of pixels.

4.2 NADH response to hypoxia induced metabolic inhibition

The motion correction protocol presented in the previous section enables us to track tissue intrinsic fluorescence changes on a pixel-by-pixel basis. We now apply this analysis protocol to real time courses of two types of functional fluorescence responses: the response to metabolic inhibition (hypoxia) and to metabolic load (electrical activity). Using the ability of the pixel-by-pixel analysis to resolve fine spatio-temporal heterogeneity in tissue metabolic response, we will demonstrate differences in the metabolic response of cytosol and mitochondria to hypoxia, and neurons and cytosol to electrical stimulation. We begin with the response of resting neurons to metabolic inhibition.

4.2.1 Energy metabolism in resting neurons

The current picture of neuronal metabolism postulates that neurons use oxidative metabolism simply to maintain basal metabolic processes (1,2). There is some controversy regarding the source of the additional energy required by activate neurons. In particular, the balance of anaerobic glycolysis and aerobic oxidative

phosphorylation in fueling neural activity is somewhat controversial. We have contributed evidence towards a resolution of that controversy which will be discussed later in Section (4.3)(3).

Resting neurons use the largest part of their ATP to maintain resting membrane potential (4). Of the ion pumps involved in maintaining ion homeostasis, the Na-K-ATPase consumes the majority (>50%) of cellular ATP. The Na-K-ATPase pump works incessantly to pump K^+ ions into the neuron and Na^+ ions out of the neuron in order to compensate for their leak across the plasma membrane. While the Na-K-ATPase pump is the dominant pump for maintaining membrane potential, there are other ion pumps in the neuronal membrane. However, these are either passive transport pumps, produce a relatively small demand on oxidative metabolism, or begin functioning only during (or shortly after) an action potential, i.e. in an active neuron (4). This dependence of the basic membrane integrity of the neuron on aerobically derived energy makes neurons acutely sensitive to oxygen deprivation.

4.2.2 Effects of hypoxia

Transient hypoxia followed by reperfusion triggers changes in metabolite concentrations, ion gradients, and protein expression that can lead to both long term damage and protection against further hypoxic insults. Some of these changes occur rapidly, on the time scale of our experiments, while others such as changes in protein expression can take many hours or more. We will confine our discussion here to those changes that occur on the time scale of our experiments and that are relevant to the immediate metabolic state.

The most direct effect of removing oxygen from the intracellular environment is the inhibition of mitochondrial metabolism (see Section (2.1)). Without active mitochondria, which are the most efficient source of ATP, the ATP level in the cell

drops precipitously and ADP begins to accumulate (5-8). ADP upregulates glycolytic enzymes, representing an attempt to make up the ATP shortfall through anaerobic metabolism. Glycolysis however is a poor source of ATP and is unable to sustain the normal activity of the Na-K-ATPase, which leads to an almost complete depolarization of the plasma membrane (9). Within ~5 minutes of the onset of anoxia, intracellular Na^+ increases by a factor of ~2 (10) and extracellular K^+ increases by a factor of ~1.4-2 (11).

It is believed that the increased intracellular Na^+ concentration caused by the failure of the Na-K-ATPase pump leads to the activation of the Na-Ca antiporter in the plasma membrane. As Na^+ leaks into the cytosol, this pump begins to shuttle 2Na^+ back out of the cytosol in exchange for Ca^{2+} from the extracellular medium. In this way, there is a Ca^{2+} build up in the neuron (12). The elevated intracellular Ca^{2+} level has a profound influence on many processes. In particular, Ca^{2+} is known to upregulate the activity of metabolic enzymes in the mitochondria (see Section (2.1)). During hypoxia, this has little effect as there is no oxygen to allow the electron transport chain to run. However, upon post-hypoxic reperfusion with normoxic ACSF, the cell is faced with elevated levels of ADP, NADH, Ca^{2+} and a normal level of oxygen. The result is that the flux through the mitochondrial metabolic pathways is higher than normal, bringing the NADH level not simply back to baseline, but in fact causing a hyperoxidation of mitochondrial NADH (13-15).

In oxidative metabolism, pyruvate produced during glycolysis ultimately serves as the initial substrate for mitochondrial metabolism. When the cell switches to anaerobic glycolysis, pyruvate can no longer be used by mitochondria. To prevent product inhibition of glycolysis, this pyruvate is converted into lactate (lactic acid). Tissue lactate rises from ~4mM (16) to 8-15mM (16-18) during hypoxia. This lactate build up is largely responsible for the fall of the intracellular pH from ~7.4 (19-21) to

~6.5-6.7 after 10 min hypoxia (20). While an excessive accumulation of lactate can cause damage due to the decreased pH, the amount accumulated during brief hypoxic intervals plays an important role in the post-hypoxic recovery of normal synaptic activity. Accumulated extracellular lactate is used as the principal source of energy during post-hypoxic recovery, rather than glucose, and is responsible for restoring ~80% of synaptic activity (22,23).

4.2.3 Analysis of hypoxia image time series

4.2.3.1 Structure of time series

A time series consists of a sequence of N images acquired with an inter-image interval Δt . Throughout the time series, the sample is being constantly perfused with artificial cerebro-spinal fluid, and the metabolic state of the slice is controlled by the oxygen concentration of this perfusate. For studies of metabolic dynamics in hippocampal brain slices, the time series has three phases:

1. Baseline: This is a series of 10 images taken 30 seconds apart, acquired while the slice is maintained in its normal, resting state. The surrounding perfusate has a high partial pressure of oxygen (0.6-0.8 atm depending on perfusion chamber). The purpose of this series is to record the spatial distribution and spontaneous intensity fluctuations (noise) of the intrinsic fluorescence in an unperturbed, resting metabolic state.

2. Response (or Early Response): During this middle phase of 10 images, the perfusate is switched to a solution with no oxygen, leading to metabolic inhibition. The time scale of the change in oxygen concentration in the actual perfusion chamber depends on the geometry and flow speed. In the open perfusion chambers, oxygen level reaches a minimum in ~ 2 minutes and in the fast flow closed chambers, this takes <10

seconds. The effect of this metabolic perturbation on the intrinsic fluorescence is imaged for another 10 images, allowing the response to complete and the fluorescence to stabilize at some new value.

3. Recovery (or Late Response): During this last phase of 15 images, the external conditions are returned to their normal, baseline values, i.e. the high oxygen perfusate is returned to the chamber. The tissue is then imaged as it recovers and re-establishes its baseline metabolic state. While this phase consists of 15 images in our experiments, we will show later that this duration was ultimately insufficient for the tissue to recover all of its baseline fluorescence characteristics.

4.2.3.2 Motion correction and sub-series definition

Each image in the slice was first smoothed with a Gaussian 3x3 spatial filter in order to reduce noise. After smoothing, motion correction of the slice was done according to the protocol described in Section (4.1). Typically, using only the brightest 1% of all pixels for motion correction, and splitting the image into 100x100 to 200x200 pixel sub-images was found to be most effective in eliminating motion. After motion correction, a further Gaussian 3 temporal filter was applied to reduce post-motion correction difference intensity anti-correlation (see Section (4.1)).

The temporal correlation curve for each image series ($r(t)$) was calculated to yield a measure of the residual uncorrectable motion of the sample (see Section (4.1)). This determined how far a given region of interest could be followed in time before the correlation decay indicated that an unacceptable amount of motion had accumulated. In all cases, we defined an unacceptable amount of motion as >0.75 micron – chosen as it corresponds to about half the width of a mitochondria. Based on this criterion, in a typical image series of 35 images (10 baseline + 10 response + 15

recovery), a given region of interest could only be followed for $\sim 4-7$ images. Nonetheless, many of the interesting changes that occur in hypoxia response and recovery occur within about 3-4 image frames. Hence by selecting sub-series of 4-7 images at critical time points within the main image series, it is still possible to perform pixel-by-pixel measurements on interesting metabolic dynamics.

There are four time sub-series that we define for the purpose of pixel-by-pixel analysis which correspond to physiologically distinct events. The time intervals bounding these four sub-series are shown in Figure (4.6) on a plot of the mean fluorescence intensity.

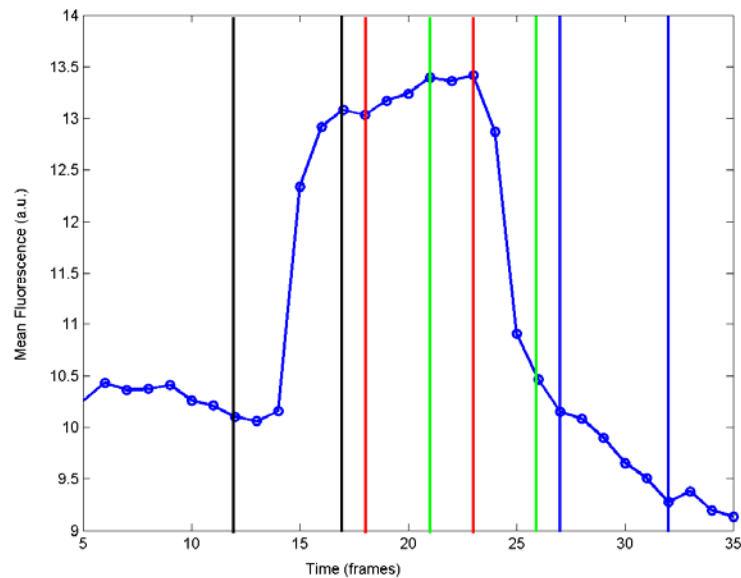


Figure 4.6 Mean intensity of intrinsic fluorescence during transient hypoxia. The phases indicated by the vertical lines are: normoxia-hypoxia transition (black), sustained hypoxia (red), hypoxia-normoxia transition (green), post-hypoxic recovery (blue).

These sub-series intervals are:

Normoxia to Hypoxia Transition.

Sustained Hypoxia

Hypoxia to Normoxia Transition

Post-hypoxic Recovery

4.2.3.3 Intensity changes of percentile bins

Figure (4.7a) shows the intensity histograms of a series of images before, during and after a brief hypoxic episode. Note that during hypoxia, the histogram decreases in height, increases in width and moves higher up the intensity axis. The intensity increase and spreading of the histogram implies that pixels of a higher intensity undergo a greater absolute intensity increase than those of a lower intensity.

Considering the histograms of the images normalized by their respective mean intensities (Fig.(4.7b,c)) however reveals that the shapes of the histograms during all three metabolic states are very similar. This behavior suggests that pixels largely maintain their intensity percentile rankings during hypoxia and reperfusion. Significant populations of pixels changing their percentile ranking would cause the shape of the histogram to change i.e. narrow.

Since the intensity percentile of a pixel does not change, on average, during a time series, it follows that a given range of intensity percentiles represents the same population of pixels throughout the time series. It is therefore reasonable to use a percentile range to define populations of pixels in each image. A given percentile range represents the same set of pixels throughout the time series, and we can therefore measure the average intensity of that percentile range as a function of time to arrive at the intensity response of different sets of pixels with different average baseline intensities.

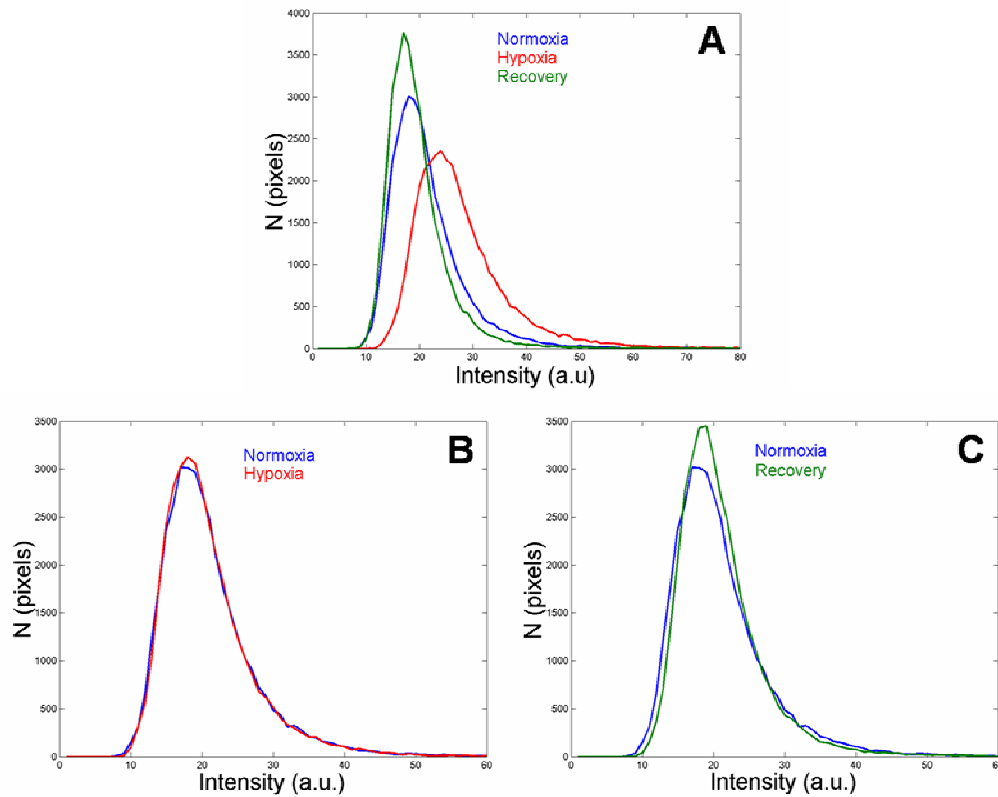


Figure 4.7 Intensity histograms of intrinsic fluorescence during transient hypoxia. (A) Intensity histogram of brain slice before, during and after hypoxia. (B) Intensity histograms of normoxic and hypoxic tissue normalized by their respective mean intensities. (C) Intensity histogram of normoxic and recovered tissue normalized by their respective mean intensities.

Furthermore, given the large difference in NADH fluorescence intensity between mitochondria and cytosol observed in cultured cells (see Section (3.2.1)), it is reasonable to expect a similar correspondence in tissue. It is therefore of particular interest to compare the responses of the highest and lowest intensity pixels. The average intensity of 5 percentile ranges (0-20%, 20-40%, 40-60%, 60-80%, 80-100%) is calculated as a function of time. The number of percentile bins was chosen as a compromise between reducing difference-intensity anti-correlation (see Section (4.1.5)) and still being able to discriminate high and low intensity pixels. The resulting

calculated responses of the highest and lowest intensity bins during the image intervals defined above (Section 4.2.3.2) are shown below in Figure (4.8).

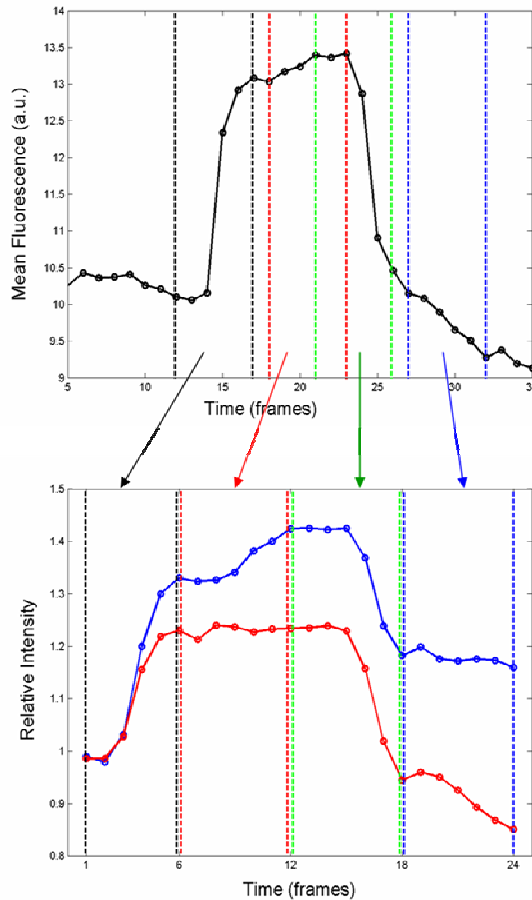


Figure 4.8 Response of the brightest and dimmest pixels to hypoxia. The motion corrected sub-series of the hypoxic response - defined by colored intervals in the top graph – were analyzed individually. The responses of the lowest 20th percentile (blue curve) and highest 20th percentile (red curve) during these intervals are plotted in the lower graph. The responses are pasted together for convenience of display.

During the normoxia to hypoxia transition (black interval) both intensity brackets respond similarly, with a slightly greater fractional increase in the lower intensity bracket. The higher intensity bracket stops increasing shortly after the

normoxia to hypoxia transition while the low intensity pixels continue to increase in intensity during the sustained hypoxia sub-series (red interval). Upon reperfusion, both intensity brackets decrease in intensity with a slightly greater fractional decrease in the high intensity bracket (green interval). During post-hypoxic recovery (blue interval), the low intensity bracket undergoes a slight continued decrease while the high intensity pixels continue to decrease in intensity very substantially.

4.2.3.4 Discussion of heterogeneous response to hypoxia

The observed heterogeneous response to hypoxia is consistent with the interpretation that the highest intensity pixels are predominately mitochondrial, while the lowest intensity pixels are predominately cytosolic. Hypoxia leads to a build up of cytosolic and mitochondrial ADP, Ca^{2+} and NADH (Section (4.2.2)). While all these factors would normally increase flux through the electron transport chain (ETC), the lack of oxygen does not allow the ETC to run faster. When the oxygen is returned to baseline levels during reperfusion, the ETC runs at a rate higher than baseline due to the built up ADP, Ca^{2+} and NADH. This elevated activity of the ETC is sustained, thereby producing a hyperoxidation of NADH to below its baseline level.

Low intensity pixels are cytosolic in origin. The cytosol is somewhat slower to reach its peak response than mitochondria, as seen in the continued rise of the low intensity pixels during the sustained hypoxia sub-series while the high intensity pixels remain constant. This is understandable given that hypoxia acts directly on mitochondria. The cytosolic NADH responds to the increase in mitochondrial NADH. Upon hypoxia, ATP must be generated from anaerobic glycolysis. In order to do this, glycolitically derived pyruvate in the cytosol, normally destined for mitochondria, is instead converted to lactate to prevent product inhibition of glycolysis, leading to a build up of lactate in the cytosol/extracellular space. Since the NADH/NAD⁺ ratio is

in rapid equilibrium with the lactate/pyruvate ratio (24), the lactate build up increases the NADH level. Upon reperfusion, this accumulated lactate will slow the decrease in the cytosolic NADH level as the lactate either diffuses out of the immediate extracellular space, or is reconverted into pyruvate for use in mitochondria.

4.2.4 Conclusions

Previous work done on intrinsic NADH fluorescence dynamics averages the fluorescence signal over a relatively large region of tissue (25-29). This provides no information about the spatial heterogeneity of the NADH response to metabolic inhibition. While two-photon microscopy provides adequate resolution to detect spatial heterogeneity on the length scale of metabolic compartmentation, pixel-by-pixel analysis is difficult due to sample motion. Motion correction provides the ability to discriminate and separately follow high and low intensity pixels which in turn allows the dissection of the mitochondrial and cytosolic response to hypoxia.

We find that pixels identified as mitochondria exhibit a rapid increase in intensity upon hypoxia and undergo a post-hypoxic hyperoxidation. In contrast pixels identified as cytosolic respond more slowly to hypoxia and incompletely recover on the time scale of our experiments. These results are consistent with the known hypoxic/ischemic response of NADH in isolated mitochondria and extracellular lactate in intact brain tissue. This demonstrates that pixel-by-pixel analysis of motion corrected 2P NADH fluorescence images can probe metabolic response heterogeneity in intact neural tissue. The ability to follow the time evolution of pixels will be applied in the next section to explore the controversial partitioning of activity induced metabolic load between neurons and astrocytes.

4.3 NADH response to activity induced metabolic load

4.3.1 Energy metabolism in active neurons

The prevailing view of metabolism in neurons in resting state (see previous Section) is largely agreed upon. In stark contrast, considerable controversy has surrounded the picture of metabolic dynamics in active neurons. Much of this controversy is due to the limitations of the various metabolic imaging techniques (fMRI, PET, optical spectroscopy) that have provided different and at times discordant pieces of the puzzle. Some of the most prolific contributors are techniques (fMRI, optical spectroscopy) whose relations to fundamental cellular mechanisms are not quantitatively understood.

The controversy surrounds the source of the additional energy used by active neurons. Fox et al (30) used PET to show that neural activity induces a transient glucose uptake in excess of the glucose actually consumed by oxidative metabolism – arguing for an increase in anaerobic glycolysis during activity. In contrast, evidence from NMR(31) and optical spectroscopy (32) suggests oxidative metabolism is the principal energy source for neural activity. Continued investigation of this controversy has led to the hypothesis that perhaps the partitioning of the metabolic cost of activity between astrocytes and neurons underlies the apparent disparities between these experimental results.

Pellerin & Magistretti showed that glutamate uptake by astrocytes in culture stimulates them to release lactate (33). Furthermore, lactate can serve in place of glucose as a substrate for active neurons (34,35). This evidence led Pellerin & Magistretti to propose what is now known as the lactate shuttle hypothesis (36) which postulates that astrocytes exhibit aerobic glycolysis, i.e. they convert glucose predominately into lactate, which is then transferred through the extracellular space to neurons and converted into pyruvate for oxidative metabolism. However, there was no

direct evidence for this specific interplay of astrocytes and neurons during neural activity.

The need to monitor rapid metabolic responses to electrical activity with sufficient spatial resolution to distinguish astrocytes and neurons was stated by a number of investigators (35,37-41). The techniques mentioned above (fMRI, PET, spectroscopy) however fall far short of the required spatial resolution (~1-10 μ m). This represents an ideal opportunity for multi-photon microscopy, which we have shown in previous chapters to have adequate spatial resolution to distinguish neurons versus astrocytes and even mitochondrial versus glycolytic compartments. The experiments and analysis presented here were done by Kasischke et al (3) and provided the first direct support for the lactate shuttle model of neurometabolic coupling.

4.3.2 Stimulation and imaging protocol

The stimulation and imaging of brain slices was done in 3 distinct phases analogous to the baseline, response and recovery phases of the hypoxia time series in the previous section.

1. Baseline – a basal level of activity was maintained by stimulating at 0.2Hz for 5 minutes during which images were recorded every 60 seconds. The purpose for the minimal stimulation is not to induce metabolic load, but rather, to monitor the response of the slice to stimulation. In particular, local field potentials (LFPs) that are stable and significant in amplitude are required before we can quantitatively study the response of the tissue to heightened stimulation. The stability and amplitude of the evoked local field potentials are often simply a function of the health of the slice and the location of the stimulation and recording electrodes. Brain slices that have not recuperated sufficiently from the preparation procedure respond only weakly to

stimulation. Typically, a brain slice requires 60-90 minutes to recover from preparation. On the other hand, significant LFP amplitude is often a question of optimizing the position of the stimulating and recording electrodes so that recording is occurring near the subset of the Schaeffer collaterals that are being stimulated.

2. Stimulation Response – the activity induced metabolic load was increased by increasing the stimulation frequency to 32Hz. This heightened activity was sustained for 5, 20, 60 or 240s during which time images were recorded every 5 seconds.

3. Recovery – the stimulation protocol was returned to that of baseline (i.e. 0.2 Hz) and images were recorded every 60 seconds for another 5 minutes while the brain slice recovered from the transient elevated load.

4.3.3 Image analysis protocol

4.3.3.1 Motion correction

This was done according to the algorithm detailed in Section (4.1). The specifics to these time series follow. Image series were broken up into 150x150 pixel regions to accommodate tissue distortion. Motion correction was done using maximization of the overlap integral of the brightest 1-2% of pixels. Motion in stimulation series is typically not as severe as it is in hypoxia series for a number of reasons. Firstly, in order to stimulate and record from the brain slice, electrodes are inserted into the tissue, this has the incidental benefit of anchoring the slice down so that only slight jitter must be corrected. Secondly, during the stimulation phase of the image series, images are acquired every 5 seconds – a much shorter time than the 30-60 second interval between hypoxia series images – reducing the amount of drift between sequential images. Lastly, the physiological changes that occur upon transient

metabolic load are much less drastic than those that occur upon hypoxia. Changes in average fluorescence (<5%) and tissue distortion due to swelling are comparatively small.

4.3.3.2 Criterion for significance of response

Perhaps the most significant difference between the analysis of the response to stimulation and to hypoxia is that not all points in the tissue will respond to stimulation. This simply reflects the fact that synaptic release is a stochastic process and hence not all synapses in the imaged region will be activated by stimulation. Therefore, to quantify NADH response to neural activity, it is necessary to exclude from analysis those pixels that do not respond. For each pixel, the mean and standard deviation of the intensity were calculated during intervals in the baseline and response phase. If the means were significantly different ($p < 0.05$) then that pixel was deemed to have a statistically significant change or response. Only pixels with a significant response were included in analysis.

4.3.3.3 Definition of overshoot and dip masks

In order to specify which pixels have statistically significant responses upon stimulation, we define Overshoot and Dip Masks. Overshoot and Dip Masks are arrays that have a 1 at those pixels with statistically significant fluorescence increases and decreases respectively, and a 0 at all other pixels. Generating these masks entails first calculating the following arrays from the recorded time series $I(x,y,t)$:

a. Baseline mean array: $\overline{I}_{base}(x, y) = \frac{1}{Nb} \sum_{t=1}^{Nb} I(x, y, t)$. This is the mean value of each

pixel during the Nb (~ 4) baseline images that constitute the baseline phase.

b. Baseline standard deviation array: $\sigma_{base}(x, y) = \sqrt{\frac{1}{Nb-1} \sum_{t=1}^{Nb} (I(x, y, t) - \overline{I_{base}}(x, y))^2}$.

This is the standard deviation of the fluctuations of each pixel during the baseline phase.

c. The Dip Image: $\overline{I_{dip}}(x, y)$ is an average of a range of images around the peak of the mean intensity dip (point of lowest mean intensity). This range usually begins immediately after the baseline phase at image 5 and extends for ~ 4 images.

d. The Overshoot Image: $\overline{I_{ovs}}(x, y)$ is an average of a range of images around the peak of the mean intensity rise (point of highest mean intensity). This range usually begins ~ 2 images after the dip range and can extend as far as the end of the response phase.

The Dip Mask (DM(x,y)), is then the logical array defined by:

$$\begin{aligned} DM(x, y) &= 1 \quad \text{if } I_{dip}(x, y) \leq \overline{I_{base}}(x, y) - T_{dip} \sigma_{base}(x, y) \\ DM(x, y) &= 0 \quad \text{if } I_{dip}(x, y) > \overline{I_{base}}(x, y) - T_{dip} \sigma_{base}(x, y) \end{aligned} \quad (4.9)$$

Analogously, the Overshoot Mask (OM(x,y)) is the logical array defined by:

$$\begin{aligned} OM(x, y) &= 1 \quad \text{if } I_{ovs}(x, y) \geq \overline{I_{base}}(x, y) + T_{ovs} \sigma_{base}(x, y) \\ OM(x, y) &= 0 \quad \text{if } I_{ovs}(x, y) < \overline{I_{base}}(x, y) + T_{ovs} \sigma_{base}(x, y) \end{aligned} \quad (4.10)$$

where

$$T_{dip} = t(n_{base}, n_{dip}) \sqrt{n_{base}^{-1} + n_{dip}^{-1}} \quad (4.11)$$

Here n_{dip} and n_{base} are the number of images averaged into the dip and baseline images respectively. The parameter $t(n_{base}, n_{dip})$ is the t value for a 95% confidence interval with $(n_{base} + n_{dip} - 2)$ degrees of freedom taken from a standard Student's t table. T_{ovs} is defined analogously.

These masks now define those pixels which have a statistically significant dip or overshoot, and hence exclude those pixels whose intensity change is due simply to spontaneous fluctuation (noise) and not true physiological response. Restricting analysis to these pixels enables the extraction of the true microscopic metabolic response to activity that is not diminished by averaging with non-responding regions.

4.3.3.4 Application of dip and overshoot masks

Once the Dip and Overshoot Masks are defined, they are multiplied (pixel-by-pixel) to any given image or set of images in the time series to restrict analysis to non-zero pixels. Using the dip and overshoot masks, we can calculate:

1. The correlation of the dip and overshoot masks. This parameter reveals whether regions that significantly dip and overshoot are correlated in their location within the tissue.
2. Baseline intensity histograms of dip and overshoot regions. Applying the Dip and Overshoot Masks to the baseline mean image, and histogramming the resulting non-zero pixels gives us the intensity histograms of those pixels that dip and those that overshoot.
3. Time evolution of the Dip and Overshoot regions. By applying the Dip and Overshoot Masks separately to the entire time series, we can follow the time evolution of these separate populations of pixels.

4.3.4 Results of analysis

4.3.4.1 Correlation of the dip and overshoot regions

An example of the spatial relationship between the dip regions, overshoot regions and underlying NADH intensity is shown in Fig.(4.9). The superposition of

the dip and the overshoot masks onto the baseline images revealed that the dip originated from small, roughly circular areas (Fig.(4.9c)). In contrast, overshoot regions were significantly larger than the dip regions, and often co-localized with identifiable astrocyte bodies (Fig.(4.9d)). Overlaying the dip and overshoot masks (Fig.(4.9b)) reveals that there is essentially no overlap between the two.

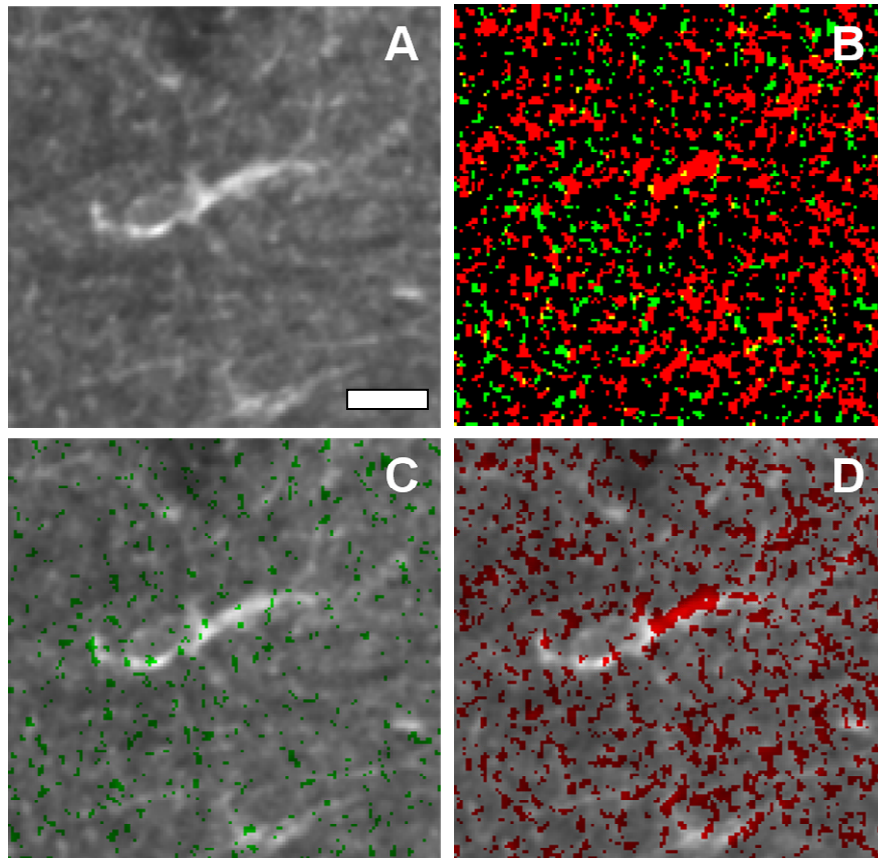


Figure 4.9 Spatial relation of dip, overshoot and NADH. (A) Intrinsic fluorescence from neuropil showing bright astrocyte. (B) Dip (green) and overshoot (red) masks show little co-localization (yellow). (C) Dip region (green) overlaid on intrinsic fluorescence. (D) Overshoot (red) overlaid on intrinsic fluorescence. Scale bar is 20 μ m.

The linear correlation coefficient or Pearson correlation coefficient (r) of the dip and overshoot masks is calculated to be $r = -0.92 \pm 0.02$ (N=9), indicating a strong

anti-correlation of the two regions. The linear correlation coefficient is a measure of the degree of linear correlation between two variables (42). Given two arrays A and B , the correlation coefficient is defined as:

$$r = \frac{\sum_m \sum_n (A_{mn} - \bar{A})(B_{mn} - \bar{B})}{\sqrt{\left(\sum_m \sum_n (A_{mn} - \bar{A})^2\right)\left(\sum_m \sum_n (B_{mn} - \bar{B})^2\right)}} \quad (4.12)$$

This is a continuous variable that ranges between -1 for completely anti-correlated arrays, to 0 for uncorrelated arrays, to 1 for correlated arrays. In calculating the correlation, the sum is over only those pixels that respond to stimulation, i.e. exhibit either a dip or an overshoot (or both). Pixels that fail to exhibit significant response to stimulation are not included in the sum. The quantity r^2 is also known as the coefficient of determination and represents the fraction of the variation between the two arrays that can be explained by a linear relationship. Small values of r^2 tend to indicate either significant scatter in the data, or a nonlinear relationship between the two variables. Given an observed correlation coefficient, r , between two arrays (of N pixels), the probability that the magnitude of this correlation arose from uncorrelated arrays is given by (42):

$$P(r, N) = \frac{2}{\sqrt{\pi}} \frac{\Gamma\left(\frac{N-1}{2}\right)}{\Gamma\left(\frac{N-2}{2}\right)} \int_{|r|}^1 (1-x^2)^{(N-4)/2} dx \quad (4.13)$$

This provides a measure of significance on our calculated correlation or anti-correlation. The large array sizes typical of our data ($N \sim 10000$), give $P(r, N)$ values that become negligible very rapidly as a function of r . For example, even for a low correlation coefficient of $r = 0.1$ ($N = 10000$), we find that $P(r, N) \sim 10^{-22}$. This simply

reflects the fact that large uncorrelated arrays yield $r = 0$ with a very narrow distribution in r . Hence, the correlation coefficients observed in our data analysis prove an underlying correlation, because the probability that they arose from uncorrelated data is negligible (typically $P(r, N) < 10^{-100}$).

4.3.4.2 Baseline intensity histograms of dip and overshoot regions

The baseline intensity histograms of the intrinsic fluorescence underlying the dip and overshoot regions are shown in Fig.(4.10). The mean baseline intensity of the dip region (mean \pm SD: 45 ± 11) is $\sim 22\%$ higher than that of the overshoot region (37 ± 8) and $\sim 10\%$ higher than the mean intensity of the entire tissue (41 ± 8).

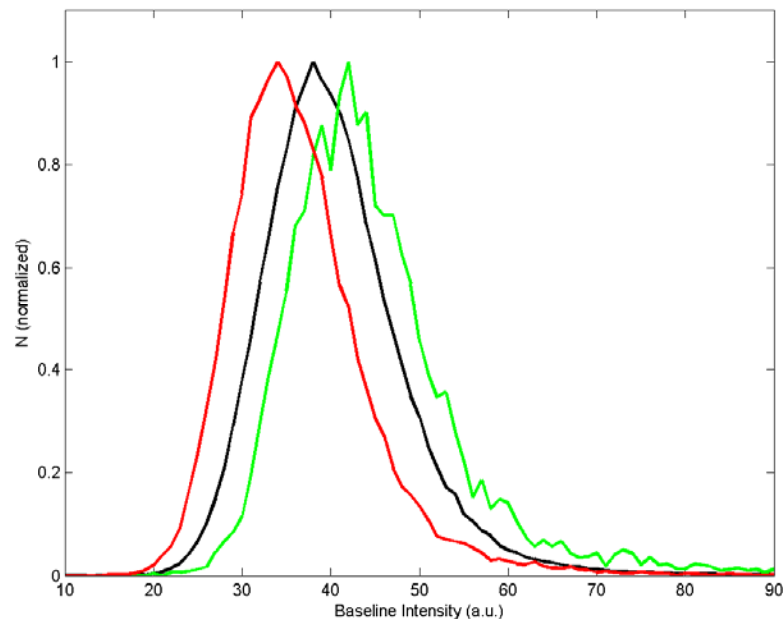


Figure 4.10 Baseline intensity histograms of dip region (green), overshoot region (red) and entire tissue (black).

It is notable however that while the overshoot region on average has a low intensity, overshoot pixels are often found on the somata of astrocytes which actually

have a higher intensity than the tissue mean. Nonetheless, most overshoot pixels have intensities lower than the tissue mean. Recall however (Section (3.4)), that only the astrocyte soma and proximal processes appear bright. The distal processes of astrocytes are indistinguishable from the surrounding neuropil.

4.3.4.3 Time evolution of the dip and overshoot regions

The intensity responses of those regions that overshoot and dip are different in their response magnitude and timing. The dip begins rapidly upon stimulation and reaches its maximal response (lowest intensity) in ~ 10 seconds (Fig.(4.11), red line) with a half-time of 2-3s. The dip signal begins to recover immediately upon cessation of stimulation. The signal returns to within $\sim 10\%$ of its baseline level in ~ 30 s with a ~ 5 s half time. In contrast, the overshoot begins slowly and peaks in ~ 50 seconds (green line) with a half time of 20-25s.

While the average dip and overshoot magnitude are approximately equal, the total area of the overshoot region is ~ 4 times larger than the total area of the dip region. Hence, the integrated response is dominated by the overshoot (black curve), and were it not for the temporal offset of these two responses, the dip would not be observable in the mean tissue intensity. The dip and overshoot regions do not strictly define distinct morphological compartments. Since the two photon focal volume in deep tissue ($\sim 2\mu\text{m}$ axial length) is larger than the size of astrocytic processes ($< 1\mu\text{m}$) and finer neuronal dendrites, any given pixel can potentially subsume some of both of these compartments. The response of a pixel will then depend on whether it is predominately astrocyte or dendrite.

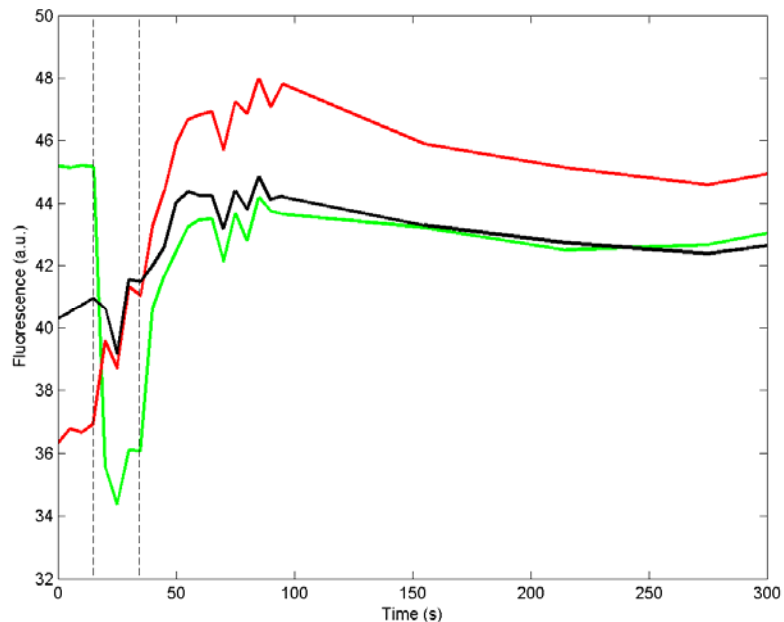


Figure 4.11 Response of intrinsic fluorescence to stimulation. The integrated fluorescence of the entire image (black) exhibits a small dip and a large overshoot. Dip and overshoot masks can be applied to dissect the dip (green) and overshoot (red) responses.

4.3.5 Discussion of heterogeneous response to activity

The high intensity of the dip regions, taken in conjunction with the fact that these regions are small and punctuate, suggests that the dip originates from neuronal mitochondria. This dip is not likely to arise from astrocytic mitochondria as it is almost completely abolished by CNQX, a non-NMDA receptor antagonist which is known to not interfere with astrocytic function (3). The effect of CNQX argues that the dip is not only neuronal but specifically post-synaptic. In contrast, the low intensity of the overshoot regions, as well as their co-localization with morphologically obvious astrocytes, reveals that the overshoot arises from astrocytes and possibly cytosolic regions of neurons as well.

From the identification of the compartments associated with the dip and overshoot, we can interpret the dip/overshoot time course. The initial response to tetanic stimulation is a rapid oxidation of NADH in neuronal mitochondria caused by an upregulation of the mitochondrial electron transport chain. The recovery of the NADH level is then due to an increased Krebs' cycle activity (NADH source). This increased NADH source counteracts the ETC sink of NADH and returns the mitochondrial NADH level to approximately baseline levels.

The mitochondrial dip was shown to be a dendritic response caused the activation of post-synaptic glutamate receptors (3,44). Blockade of these post-synaptic glutamate receptors by CNQX was found to almost completely annihilate the dip, with a much smaller attenuation of the overshoot.

The astrocytic/cytosolic increase in NADH is much slower and the elevated intensity is sustained for a substantial duration after stimulation. This indicates a delayed upregulation of astrocytic glycolysis in response to the transient neuronal mitochondrial activation. It also implies an increased cytosolic/extracellular lactate level (24). The concurrent elevation of extracellular lactate and NADH in response to activity has been observed in brain (45) and is thought to be due to lactate secretion by astrocytes triggered by glutamate uptake (33,45). Part of this lactate is taken up by neurons, converted back into pyruvate and used by neuronal mitochondria to recover from the sudden depletion of metabolites due to the activity induced ETC flux increase. However the sustained elevation of the astrocytic/cytosolic NADH level implies that not all of the lactate produced is committed to oxidative neuronal metabolism. This sustained, elevated lactate indicates that some of the glucose used by neural tissue is in fact non-oxidatively metabolized by astrocytes.

4.3.6 Conclusion

This work represents direct evidence in support of the lactate shuttle hypothesis (36), integrating previously conflicting views suggested by other functional imaging techniques on the oxidative or non-oxidative nature of neuro-metabolic coupling (30-32). Our results show the metabolic response of neural tissue has both oxidative and non-oxidative components and that these components partition between neurons and astrocytes respectively.

References

1. Sokoloff, L. (1999) *Neurochemical Research* **24**, 321-329
2. Gjedde, A., Marrett, S., and Vafaee, M. (2002) *Journal of Cerebral Blood Flow and Metabolism* **22**, 1-14
3. Kasischke, K. A., Vishwasrao, H. D., Fisher, P. J., Zipfel, W. R., and Webb, W. W. (2004) *Science* **305**, 99-103
4. Ames, A. (2000) *Brain Research Reviews* **34**, 42-68
5. Erecinska, M., and Silver, I. A. (1989) *Journal of Cerebral Blood Flow and Metabolism* **9**, 2-19
6. Erecinska, M., and Silver, I. A. (1994) *Progress in Neurobiology* **43**, 37-71
7. Erecinska, M., and Silver, I. A. (2001) *Respiration Physiology* **128**, 263-276
8. Silver, I., and Erecinska, M. (1998) in *Oxygen Transport to Tissue Xx* Vol. 454, pp. 7-16
9. Rader, R. K., and Lanthorn, T. H. (1989) *Neuroscience Letters* **99**, 125-130
10. Fried, E., Amorim, P., Chambers, G., Cottrell, J. E., and Kass, I. S. (1995) *Journal of Physiology-London* **489**, 557-565
11. Rice, M. E., and Nicholson, C. (1991) *Journal of Neurophysiology* **65**, 264-272
12. Zhang, Y. L., and Lipton, P. (1999) *Journal of Neuroscience* **19**, 3307-3315
13. Perez-Pinzon, M. A., Mumford, P. L., Carranza, V., and Sick, T. J. (1998) *Journal of Cerebral Blood Flow and Metabolism* **18**, 215-221
14. Perez-Pinzon, M. A., Mumford, P. L., Rosenthal, M., and Sick, T. J. (1997) *Brain Research* **754**, 163-170
15. Perez-Pinzon, M. A., Mumford, P. L., and Sick, T. J. (1998) *Brain Research* **786**, 165-170
16. Myers, R. E. (1981) *Journal of Perinatal Medicine* **9**, 78-86
17. Katsura, K., Asplund, B., Ekholm, A., and Siesjo, B. K. (1992) *European Journal of Neuroscience* **4**, 166-176
18. Katsura, K., Ekholm, A., Asplund, B., and Siesjo, B. K. (1991) *Journal of Cerebral Blood Flow and Metabolism* **11**, 597-599

19. Brooks, K. J., and Bachelard, H. S. (1992) *Neurochemistry International* **21**, 375-379
20. Kass, I. S., and Lipton, P. (1982) *Journal of Physiology-London* **332**, 459-472
21. Lamanna, J. C., Griffith, J. K., Cordisco, B. R., Lin, C. W., and Lust, W. D. (1992) *Canadian Journal of Physiology and Pharmacology* **70**, S269-S277
22. Schurr, A., Payne, R. S., Miller, J. J., and Rigor, B. M. (1997) *Brain Research* **744**, 105-111
23. Schurr, A., Payne, R. S., Miller, J. J., and Rigor, B. M. (1997) *Journal of Neurochemistry* **69**, 423-426
24. Bucher, T., Brauser, B., Sies, H., Langguth, O., Conze, A., and Klein, F. (1972) *European Journal of Biochemistry* **27**, 301-&
25. Stuart, B. H., and Chance, B. (1974) *Brain Research* **76**, 473-479
26. Stuart, B. H., and Chance, B. (1974) *Federation Proceedings* **33**, 425-425
27. Mayevsky, A., Zarchin, N., Kaplan, H., Haveri, J., Haselgroove, J., and Chance, B. (1983) *Brain Research* **276**, 95-107
28. Ji, S., Chance, B., Stuart, B. H., and Nathan, R. (1977) *Brain Research* **119**, 357-373
29. Chance, B., Stuart, B., and Ji, S. (1975) *Stroke* **6**, 237-237
30. Fox, P. T., Raichle, M. E., Mintun, M. A., and Dence, C. (1988) *Science* **241**, 462-464
31. Hyder, F., Chase, J. R., Behar, K. L., Mason, G. F., Siddeek, M., Rothman, D. L., and Shulman, R. G. (1996) *Proceedings of the National Academy of Sciences of the United States of America* **93**, 7612-7617
32. Malonek, D., and Grinvald, A. (1996) *Science* **272**, 551-554
33. Pellerin, L., and Magistretti, P. J. (1994) *Proceedings of the National Academy of Sciences of the United States of America* **91**, 10625-10629
34. Schurr, A., West, C. A., and Rigor, B. M. (1988) *Science* **240**, 1326-1328
35. Schurr, A., Miller, J. J., Payne, R. S., and Rigor, B. M. (1999) *Journal of Neuroscience* **19**, 34-39
36. Magistretti, P. J., and Pellerin, L. (1999) *Philosophical Transactions of the Royal Society of London Series B-Biological Sciences* **354**, 1155-1163

37. Rothman, D. L., Sibson, N. R., Hyder, F., Shen, J., Behar, K. L., and Shulman, R. G. (1999) *Philosophical Transactions of the Royal Society of London Series B-Biological Sciences* **354**, 1165-1177
38. Vanzetta, I., and Grinvald, A. (2001) *Neuroimage* **13**, 959-967
39. Chih, C. P., Lipton, P., and Roberts, E. L. (2001) *Trends in Neurosciences* **24**, 573-578
40. Mangia, S., Garreffa, G., Bianciardi, M., Giove, F., Di Salle, F., and Maraviglia, B. (2003) *Neuroscience* **118**, 7-10
41. Mayhew, J. E. W. (2003) *Science* **299**, 1023-1024
42. Bevington, P. R., and Robinson, D. K. (2003) *Data reduction and error analysis for the physical sciences*, 3rd Ed., McGraw-Hill, New York
43. Kageyama, G. H., and Wongriley, M. T. T. (1982) *Neuroscience* **7**, 2337-2361
44. Shuttleworth, C. W., Brennan, A. M., and Connor, J. A. (2003) *Journal of Neuroscience* **23**, 3196-3208
45. Merrill, D. K., and Guynn, R. W. (1976) *Journal of Neurochemistry* **27**, 459-464

Chapter Five

NADH Conformation and Concentration in Tissue

5.1 Introduction to intracellular NADH conformation and concentration

The role of the intrinsic fluorophore β -nicotinamide adenine dinucleotide (NADH) as the principal electron donor in glycolytic and oxidative energy metabolism makes it a convenient fluorescent probe of metabolic state (1,2). Traditionally, fluorimetric studies of metabolic dynamics have characterized metabolic states by the total NADH concentration. However, Williamson et al (3) pointed out that the reaction velocity of a given intracellular NADH-linked dehydrogenase depends on the concentration of locally available NADH i.e., the local concentration of free NADH. Given this thermodynamic importance of free NADH, considerable work has been done to discriminate the intracellular free fraction of NADH.

Analytical chemistry techniques have provided the most detailed information about intracellular free and total NADH. Pyridine nucleotide extraction (4,5) gives a measure of the total tissue NAD^+ and NADH concentrations, while the metabolite

indicator method (3,6-8) has been used to infer both the cytoplasmic and mitochondrial free NAD⁺/NADH ratio (9). However, these techniques entail destroying the tissue; thereby restricting the study of metabolic dynamics to single shot measurements. Furthermore, these techniques are also intrinsically incapable of resolving spatial variations in the free/bound state.

In contrast, fluorescence spectroscopic techniques (10-16) are non-destructive and readily extendable to an imaging modality to address spatial heterogeneity. These techniques are limited, however, by the ambiguous distinction between free and bound NADH fluorescence. Binding induced shifts of the emission spectrum (up to ~20nm) (10-12) are small compared to the width of the NADH spectrum (~150nm). Fluorescence lifetime is a more sensitive probe of NADH binding as it is enhanced significantly (up to 10 times) (13-15). However, the fluorescence decay of bound NADH is usually multi-exponential with shorter components that can be comparable to the decay time of free NADH (13). This makes it difficult to attribute a fast fluorescence decay component in tissue to free or bound NADH. Since intracellular NADH exists in dynamic pools of both the free form and bound to many different dehydrogenases, the integrated cellular spectra are an uncertain combination of many different spectral influences. What is required is a fluorescence signature that can unambiguously discriminate between free and bound NADH.

Here we show that global analysis of time resolved fluorescence and anisotropy decays (17,18) provides simultaneous information on the excited state dynamics and rotational mobility of intracellular NADH. Binding of NADH leads to an exceedingly large (>10 times) increase in the anisotropy decay time (16), reflecting the large difference in the size of the free NADH molecule and the binding enzyme. An anisotropy based approach therefore offers the most sensitive discrimination of free and enzyme bound NADH. Furthermore, the enhancement in the lifetime of

NADH in the intracellular environment provides a measure of the enhancement of its fluorescence quantum yield. By correcting for changes in the fluorescence quantum yield, we can infer fractional changes in the true NADH concentration as a function of metabolic state. We thus present a means of directly monitoring metabolic state dependent changes in the total concentration of NADH and its partition into free and bound pools, thereby bridging the gap between spectroscopy and analytical chemistry.

5.2 Photophysics of NADH in solution

5.2.1 Aqueous solution

Free aqueous NADH at room temperature exists in two conformations: folded (stacked nicotinamide and adenine rings) and extended (no such stacking). We measure the total fluorescence decay to be bi-exponential with lifetimes (and amplitudes) 350 ps (0.77) and 760 ps (0.23) arising from the extended and folded populations respectively (13,19). The resulting average lifetime is 444ps. The fluorescence quantum yield of free NADH in buffered aqueous solution is 0.019 (20) with an absorption peak at 340nm and an emission peak at 461nm as measured using steady state spectroscopy. Using the quantum yield (ϕ_f) measured by steady state fluorescence and the lifetime (τ) measured by time resolved fluorescence, it is possible to calculate both the radiative rate (k_r) and the non-radiative rate (k_{nr}) (Eqn.(5.1)).

$$\phi_f = k_r \tau = \frac{k_r}{k_r + k_{nr}} \quad (5.1)$$

The radiative rate, i.e. the rate of spontaneous emission (the Einstein A coefficient) is calculated to be $4.75 \times 10^7 \text{ s}^{-1}$. The non-radiative rate, or the rate at which

an excited molecule returns to the ground state without emitting a photon, is calculated to be $2.47 \times 10^9 \text{ s}^{-1}$.

5.2.2 Environmental Effects

The photophysical properties of NADH can be affected by any number of environmental parameters. We will focus on characterizing the effect of those parameters that are known to be variables in the type of *in vivo* experiments presented in this work. The fluorescence quantum yield of a fluorophore can be affected either through its radiative rate or through its non-radiative rate. Generally speaking, both viscosity and enzyme binding can act on NADH in a similar manner, that is, they suppress the vibrational modes of the NADH molecule and therefore reduce vibrational quenching of the excited state. This action reduces the non-radiative rate, thereby enhancing both the fluorescence lifetime as well as the quantum yield.

5.2.2.1 Viscosity

Upon increasing viscosity, we find an increase in the integrated fluorescence while the absorption remains unaffected. This indicates an increase in the fluorescence quantum yield. The increase in quantum yield is also accompanied by a blue shift of the emission spectrum (Fig.(5.1A)).

The average lifetime increases with viscosity (Fig.(5.1B)), due largely to the suppression of the non-radiative decay rate. The radiative decay rate is found to increase only slightly with viscosity (Fig.(5.1C)). In contrast, the non-radiative rate is greatly affected by the viscosity of the solvent (Fig.(5.1D)). The measured relation between non-radiative rate and viscosity follows the functional form proposed by Wilhelmi (21).

$$k_{nr} = a + b\eta^{-c} \quad (5.2)$$

Where $a = 0 \pm 1.5$, $b = 2.6 \pm 1.5$ and $c = 0.16 \pm 0.11$.

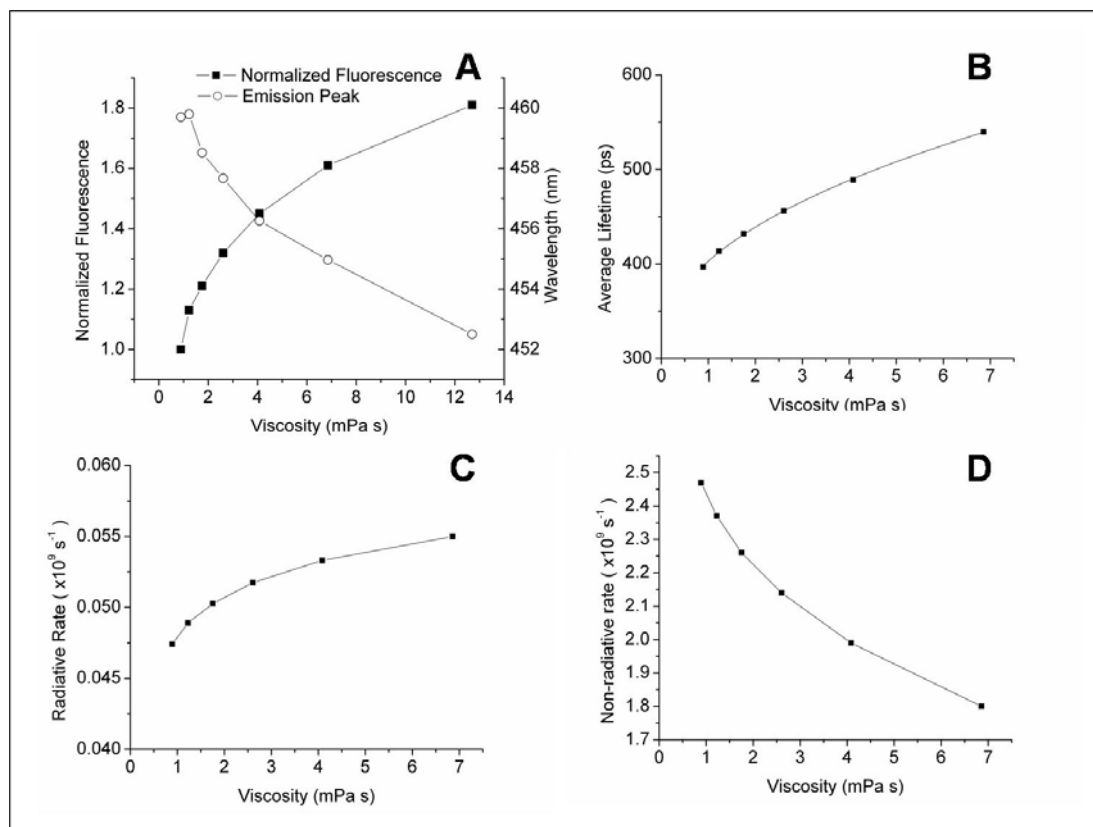


Figure 5.1 Effect of viscosity on NADH photophysics. (A) Emission peak and fluorescence enhancement. (B) Average lifetime. (C) Radiative rate. (D) Non-radiative rate.

It is possible that the non-radiative rate of a fluorophore has a component that is not coupled to motion (e.g photoionization). In the case of NADH however, we have shown that the functional dependence of the non-radiative rate on viscosity is of the form $k_{nr} = a + b\eta^{-c}$, where $a \sim 0$, indicating that the non-radiative decay is largely viscosity dependent and hence occurs via motion.

5.2.2.2 Enzyme Binding

There are seven different cellular dehydrogenases that are known to bind NADH in glucose metabolism alone. Each of these enzymes has its own specific effect on the NADH steady state and time-resolved properties. We have selected lactate dehydrogenase (LDH) and mitochondrial malate dehydrogenase (mMDH) as typical examples of these enzymes. Lactate dehydrogenase is a cytosolic enzyme that catalyzes the inter-conversion of pyruvate and lactate. Mitochondrial malate dehydrogenase is a mitochondrial enzyme that plays a role in the Krebs's cycle.

Complete binding of NADH to mMDH results in a 7nm red shift of the absorption spectrum without significant change in its amplitude. The fluorescence quantum yield is enhanced by a factor of 1.85 with a blue shift of the emission peak by 12nm as determined by steady state spectroscopy. Time resolved spectroscopy reveals that the lifetime of NADH upon binding is enhanced by a factor of 1.7, somewhat less than the enhancement of the quantum yield. This implies that the radiative rate is slightly enhanced by a factor of 1.09 (Eqn.(5.1)). In contrast, there is a large decrease in the non-radiative rate (factor 0.58).

Scott et al (20) have made similar studies of the photophysics of NADH bound to lactate dehydrogenase (LDH). Our measurements on mMDH, in combination with their results on LDH are summarized in Table (5.1).

Enzyme binding can be generally thought of as immersion in a highly viscous environment. Due to the tight, specific binding of enzymes to NADH, the fluorophore is very rigidly confined and hence the lifetime enhancement of enzyme bound NADH can be substantial. Typically the average lifetime of enzyme bound NADH is 2-10 times greater than that of aqueous NADH, depending upon the enzyme (13,22) and the binding of other substrates. In comparison, physiological viscosities produce a relatively small lifetime enhancement. Estimates of cellular viscosities vary from 1 to

4 times that of water (0.89 mPa s at room temperature) (23,24). From Fig.(6a), we can see that such viscosities correspond to an average lifetime enhancement by a factor of only ~1-1.3.

Table 5.1 Effect of enzyme binding on NADH photophysics

Enzyme	Absorption peak (nm)	Emission Peak (nm)	Quantum Yield	Lifetime	Radiative Rate	Non-radiative Rate
mMDH	347	448	1.85	1.7	1.09	0.58
LDH	335	440 (aq. NADH @ 470nm)	5.2	3.75	1.3	0.24

While it is true that tight binding suppresses vibrational relaxation of the excited state, the binding site of an enzyme can have specific interactions with NADH. These specific interactions could entail interaction of the nicotinamide ring with local groups in the binding site, or even with the adenine ring of NADH itself. These specific interactions can either enhance or reduce the lifetime depending on the interaction. At least one enzyme (GPDH: glycerol 3-phosphate dehydrogenase) is known to quench NADH fluorescence by 33% (12,25). This quenching is believed to be caused by GPDH binding NADH in a conformation in which the nicotinamide and adenine rings are stacked.

5.2.2.3 pH

The absorption and fluorescence spectra of NADH exhibited no significant change between pH 7 and pH 11. This pH range is physiologically relevant as the pH in cells varies between ~7-7.5 in the cytoplasm (26) to ~8-8.5 in the mitochondrial

matrix (27). The insensitivity of the fluorescence to this pH range is not unexpected. The transition between the stacked and extended conformations of the NADH molecule is pH dependent with a pK of ~ 4 (28), far below physiological values of pH. Since the relative concentrations of these two photophysically distinct conformations do not change in this pH range, therefore neither does the integrated fluorescence of the solution.

5.2.2.4 Oxygen quenching

While the concentration of intracellular NADH is affected by oxygen level via metabolism, the direct quenching of NADH fluorescence by oxygen is also known to occur. Czochralska et al (29) measured an oxygen quenching quantum yield (Φ_{O_2}) of 0.02 in the aerobic condition ($PO_2 \sim 0.2$ atm or 152mm Hg) and reported that the rate of oxygen quenching fell by a factor of ~ 4.3 in the anaerobic condition ($PO_2 \sim 0$ ($1.5 \cdot 10^{-5}$ M)). At room PO_2 , the fluorescence quantum yield (Φ_f) is 0.02, implying that the quantum yield of non-radiative pathways not associated with oxygen (Φ_{nr}) must be 0.96 ($1 - \Phi_f$).

Given that the lifetime of NADH at room PO_2 is ~ 400 ps, we can calculate the radiative rate (k_r), oxygen mediated non-radiative rate (k_{O_2}) and non-oxygen mediated non-radiative rate (k_{nr}) as $k_i = \Phi_i / \langle \tau \rangle$ summarized in Table (5.1). Under anaerobic conditions, k_{O_2} falls by a factor of 4.3 – giving $k_{O_2} = 1.15 \times 10^7 \text{ s}^{-1}$. Since the other intrinsic rates are not affected (by definition k_{O_2} is the rate affected by oxygen), we can now calculate the average lifetime as just $\langle \tau \rangle = (k_{O_2} + k_f + k_{nr})^{-1}$. This calculations yields: $\langle \tau \rangle = 406$ ps, a negligible change in the lifetime due to the direct effect of O_2 quenching.

Table 5.2 Excited state decay rates of aqueous NADH under aerobic conditions

Aerobic Rates		
k_r	k_{O_2}	k_{nr}
$5 \times 10^7 \text{ s}^{-1}$	$5 \times 10^7 \text{ s}^{-1}$	$2.4 \times 10^9 \text{ s}^{-1}$

5.2.3 Strickler-Berg calculation of radiative rate

In our solution studies, we are able to directly measure fluorescence and absorption, and therefore the quantum yield and the fluorescence lifetime. From the quantum yield and the lifetime, we can calculate the radiative rate (k_r) (Eqn.(5.1)). In tissue however, since we cannot easily measure two-photon absorption, we have no direct means of measuring the fluorescence quantum yield. Instead, we measure the fluorescence lifetime. Traditionally, the radiative rate has been ignored, assuming that its value in tissue is not significantly different from its value in solution, or that it represents a constant that does not change with metabolic perturbation.

It is possible, however, to use the steady state (wavelength resolved) spectral properties of some fluorophores to explicitly calculate their radiative rate from the Strickler-Berg relation (30) (Eqn.(5.3)).

$$k_r = 2.88 \times 10^{-9} n^2 \frac{\int F(\tilde{\nu}) d\tilde{\nu}}{\int \tilde{\nu}^{-3} F(\tilde{\nu}) d\tilde{\nu}} \int \varepsilon(\tilde{\nu}) d \ln \tilde{\nu} \quad (5.3)$$

Here n is the refractive index of the solution, $F(\tilde{\nu})$ and $\varepsilon(\tilde{\nu})$ are the fluorescence and absorption spectra respectively as a function of the wavenumber $\tilde{\nu}$. For free, aqueous NADH, we find that the radiative rate calculated using the measured quantum yield and lifetime ($k_r(\phi, \tau)$) is $4.75 \times 10^7 \text{ s}^{-1}$. In comparison, the radiative rate calculated from

the Strickler-Berg relation using the measured wavelength resolved spectra ($k_r(n,F,\epsilon)$) is $4.74 \times 10^7 \text{ s}^{-1}$. This excellent agreement suggests the possibility of using the wavelength resolved spectral properties of intrinsic NADH to probe its radiative rate.

Shifts in the fluorescence emission peak in response to environmental effects (e.g. enzyme binding) can be significant (up to 30nm (12)) and therefore contribute a significant change to the radiative rate. Figure (5.2) shows the calculated change in the radiative rate caused by the simulated shift of the emission peak assuming the refractive index and absorption spectrum remain constant.

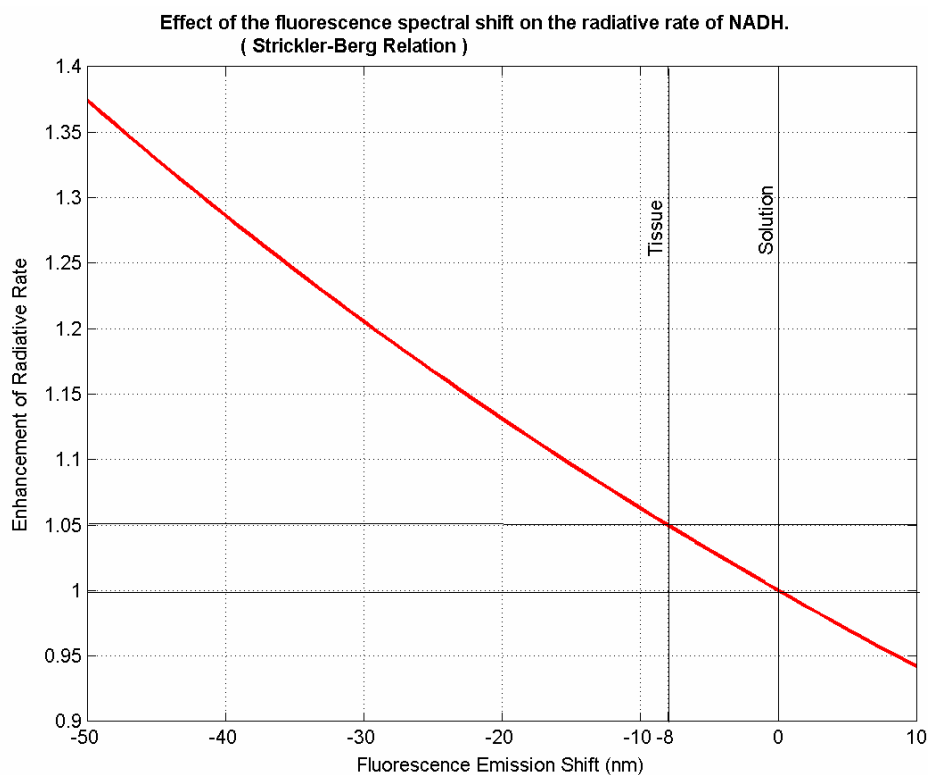


Figure 5.2 Calculated change in the radiative rate due to simulated fluorescence spectral shift.

In contrast, shifts in the 340nm absorption peak of NADH are small – rarely exceeding 10nm (12). A simulated shift of the 340nm absorption band contributes little to change to the radiative rate (Fig.(5.3)). Shifts characteristic of enzyme binding ($<\pm 10\text{nm}$) contribute a $<\pm 3\%$ change in the value of the absorption integral term in Eqn.(5.3). It is therefore not necessary to consider shifts in the absorption spectrum to get a reasonable approximation of the radiative rate.

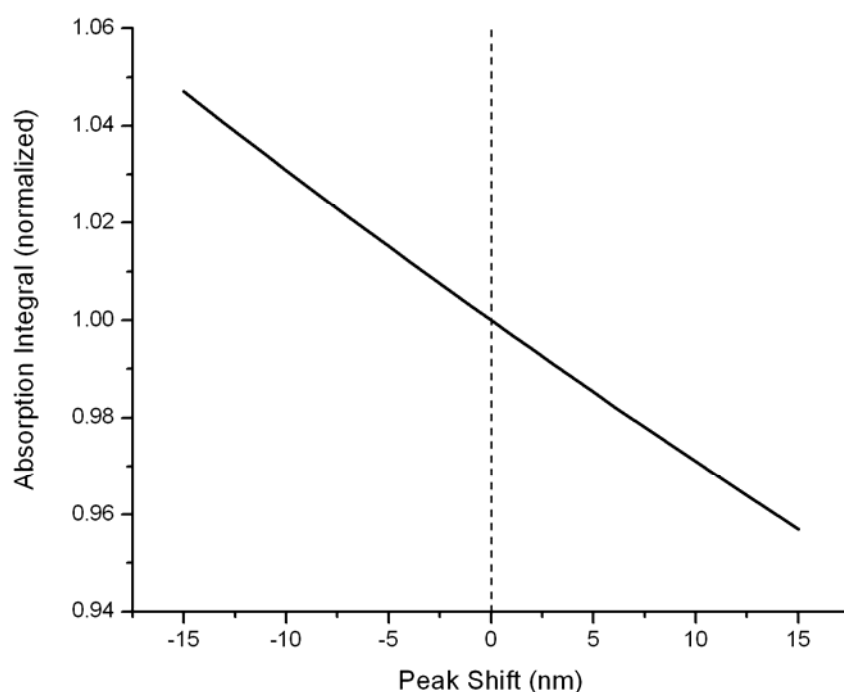


Figure 5.3 Calculated change in radiative rate due to simulated absorption shift.

To check the validity of applying the Strickler-Berg relation to NADH in a more complex environment, we compare the radiative rate calculated from the quantum yield and lifetime to that obtained from the Strickler-Berg relation in a viscous environment and bound to an enzyme.

A viscous environment has no effect on the 340nm absorption band, while it blue shifts and enhances the fluorescence in a well-defined way (see above). The blue

shift of the fluorescence increases the fluorescence integral term in Eqn.(5.3). Furthermore, the refractive index of the glycerol/water solvent mixture was taken from standard tables (31). Taking the changes in the fluorescence spectrum and the refractive index of the solvent into account in Eqn.(5.3) gave an excellent agreement (within 5%) between the radiative rates calculated by the Strickler-Berg relation and by the quantum yield/lifetime method. This agreement held for a wide range of physiologically relevant viscosities (<10 mPa s) (Fig. (5.4)), indicating that the Strickler-Berg model is a good approximation for free NADH in a viscous environment.

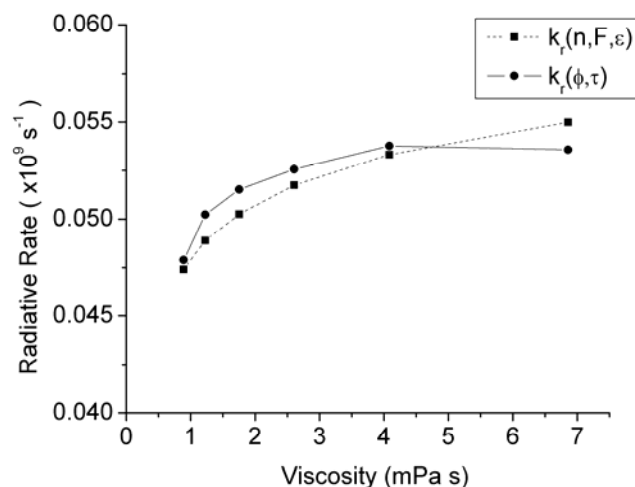


Figure 5.4 Strickler-Berg relation predicts the radiative rate of free NADH in a viscous environment.

Complete binding of NADH to mitochondrial malate dehydrogenase (mMDH) results in a 7nm red shift of the absorption spectrum without significant change in its amplitude. The blue shift in the emission spectrum increases the fluorescence integral term in Eqn.(5.3) by a factor of 1.08. The red shift of the absorption spectrum decreases the absorption integral term by a factor of 0.98. Therefore, the net change in

the radiative rate as calculated by a Strickler-Berg analysis of the steady state spectra is a factor of 1.06 – reasonably close to the enhancement of 1.09 calculated from the quantum yield and lifetime.

Scott et al (20) have made similar studies of the photophysics of NADH bound to lactate dehydrogenase (LDH) and have also found that the radiative rates calculated from the Strickler-Berg relation and the quantum yield/lifetime are in good agreement. Thus, in the cases of at least these two typical NADH binding enzymes and free NADH in a viscous environment, the wavelength resolved spectral properties of NADH appear to provide a good approximation of the radiative rate.

We have assumed here that the refractive index does not change during enzyme binding if the surrounding medium is aqueous buffer. However, the local environment of an enzyme bound fluorophore – which consists of the binding site of the enzyme as well as the solution surrounding the enzyme itself – can affect the radiative properties of the fluorophore. Toptygin et al (32) have shown that the radiative rate of tryptophan residues within an enzyme are affected by the local environment within the enzyme as well as the solution around the enzyme. In effect, the fluorophore is sensitive to any variations of the refractive index within several wavelengths of the fluorophore even if the length scale of those variations are sub-wavelength. As such, the variation of the refractive index on a microscopic scale in tissue remains an uncertainty in this work.

5.3 Fluorescence anisotropy and lifetime in tissue

5.3.1 Tissue fluorescence measurement

Time resolved fluorescence decays were recorded from the stratum radiatum (SR) of the CA1 layer of rat hippocampal slices. Each slice was subjected to a 10 minute hypoxic episode during which the intrinsic fluorescence increased in intensity

by an average of $48 \pm 26\%$. Reperfusion with oxygenated solution returned the integrated fluorescence to approximately baseline levels as expected (see Section 3.2.2 and 4.2), indicating negligible photodamage. The intrinsic fluorescence from the hippocampal slice consists of both a blue NADH peak and a yellow flavin peak that respond differently to hypoxia (see Section 3.3). However our choice of emission filter ensured the contribution from the NADH peak to the detected fluorescence was greater than 95%.

Fluorescence decays at parallel and perpendicular polarizations were measured sequentially and used to calculate the total (magic angle) fluorescence decay and the anisotropy decay. Each total fluorescence and anisotropy decay pair was fit simultaneously using a global analysis to obtain the parameters characterizing both the excited state lifetime and the rotational mobility.

5.3.1.1 Fluorescence decay functional form

Functional forms used in fitting fluorescence decays and measures of goodness of fit have been discussed in Section (2.4). A case study of a typical fit is presented here to justify the functional form that we have used to fit tissue fluorescence decay. The tissue fluorescence decay parameters are summarized in Figure (5.5).

It was found that fitting with 1 or 2 exponential decay components generated very large χ^2 and will not be discussed further. Hence, at least 3 exponential decay components were required. Furthermore, including a scatter term in the functional form resulted in a decrease in χ^2 by more than a factor of 2. The inclusion of a scattered light term is physically reasonable as tissue tends to be highly scattering. Since the two-photon action cross section of intrinsic fluorescence is extremely low, a relatively high power ($O(10\text{mW})$) must be sent into the tissue to achieve a detectable fluorescence signal. Even if only a small fraction ($\sim 1\%$) of this red excitation light is

backscattered, and largely extinguished by the emission filters ($\sim 1\%$), this still leads to a significant signal ($O(1\mu\text{W})$) reaching the detector. Given the single photon sensitivity of the lifetime detector, this can translate into a significant scatter signal.

	a1	τ_1	a2	τ_2	a3	τ_3	a4	τ_4	χ^2
n=3	0.5	180	0.3	850	0.16	3437			1.2
n=4	0.4	145	0.3	584	0.2	2239	0.03	6537	1.1

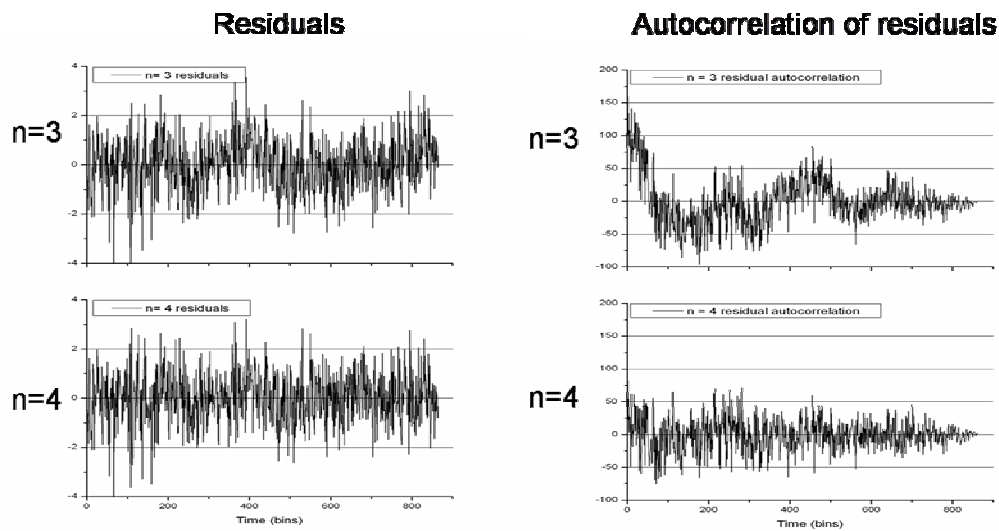


Figure 5.5 Case study - number of components required for tissue fluorescence decay fit.

We are left to consider whether 3 or 4 exponential decay components are sufficient. Figure (5.5) shows the fit parameters, χ^2 , residuals and the autocorrelation of residuals of the fits using 3 exponential decay components ($n=3$) versus those using 4 ($n=4$) exponential decay components. Both fit functions have scatter components. Relying solely upon χ^2 as the criterion for goodness of fit, one might conclude that 3 components is an adequate as it gives a low χ^2 (1.2) which improves by only 0.1 upon adding another decay component. However, if we examine the residuals and their

autocorrelations, we find that the $n=3$ fit residual has a non-random structure which is evidenced by its autocorrelation. The $n=4$ fit yields residuals and their auto-correlation that are randomly distributed about zero. Hence, the appropriate fitting model for tissue total fluorescence decay has 4 exponential decay components and a scatter term.

5.3.1.2 Average fluorescence decay fit parameters

The average of the total fluorescence decays ($n=6$) under both normoxic and hypoxic conditions are shown in Fig.5.6. The tissue fluorescence is found to have four exponential decay components (we will call these species 1 through 4) whose lifetimes(τ_i) and amplitudes (a_i), are summarized in Table (5.3).

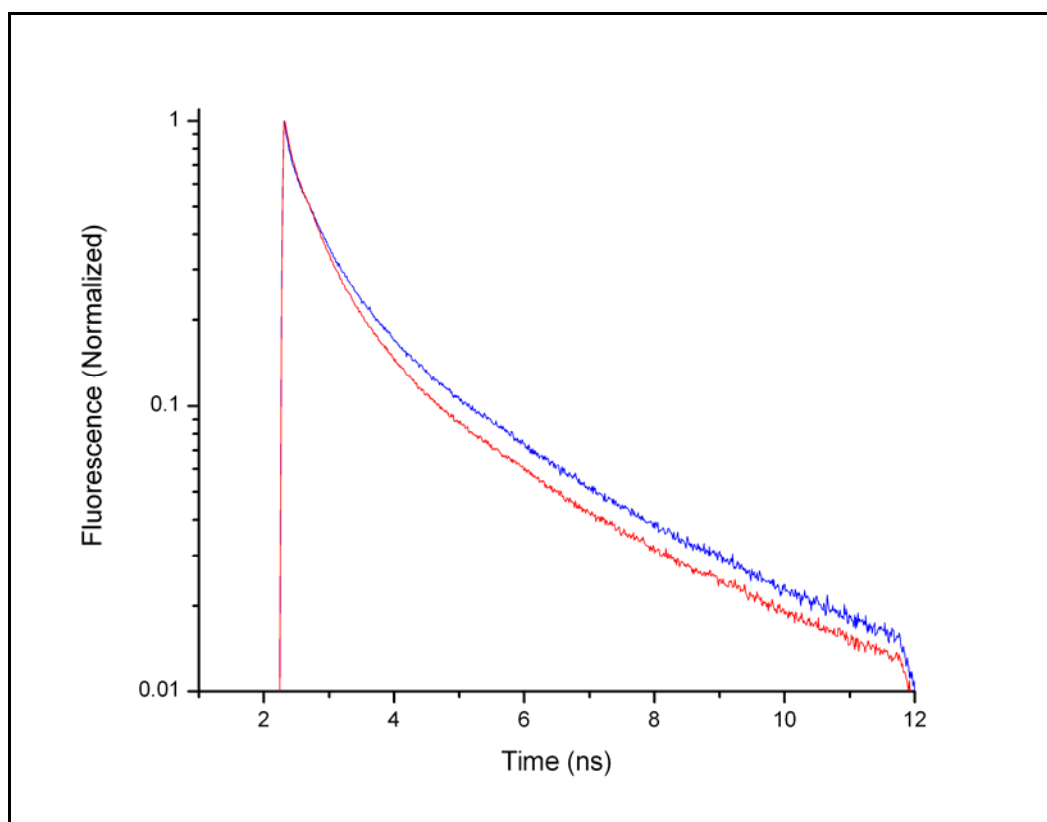


Figure 5.6 Intrinsic fluorescence decays. Intrinsic fluorescence decays are sensitive to metabolic state. The lifetime is reduced from the normoxic (blue) state to the hypoxic (red) state.

The lifetimes (τ_i) are characteristic decay times of the excited state of each species. The amplitudes (a_i) of the species are the relative concentrations of the species. In response to hypoxia, there is a modest decrease in all but the longest time constant. The amplitudes however are heterogeneous in their response. There are decreases in the amplitudes of the two longer lifetime species in favor of the two shorter lifetime species. The net effect of these changes is a decrease in the average lifetime from 948 ± 46 ps (normoxia) to 780 ± 17 ps (hypoxia).

Table 5.3 Mean (SEM) fit parameters for intrinsic fluorescence decays

	Species 1		Species 2		Species 3		Species 4		$\langle \tau \rangle$
	a_1	τ_1 (ps)	a_2	τ_2 (ps)	a_3	τ_3 (ps)	a_4	τ_4 (ps)	
Normoxia	0.44 (0.02)	155 (25)	0.32 (0.01)	599 (49)	0.20 (0.01)	2154 (79)	0.042 (0.003)	6040 (13)	948 (46)
Hypoxia	0.45 (0.02)	129 (7)	0.36 (0.01)	530 (17)	0.16 (0.01)	1975 (72)	0.0037 (0.001)	6054 (22)	779 (17)
% change upon Hypoxia	+2 (6)	-15 (15)	+13 (6)	-11 (9)	-22 (7)	-8 (6)	-12 (5)	+0.2 (0.5)	-18 (4)

From the total fluorescence decay parameters, we can calculate a number of physically important quantities. Firstly, the changes in the absolute concentrations of the individual species (ΔC_i) are calculated to be: $86 \pm 45\%$ (species 1), $104 \pm 43\%$ (species 2), $39 \pm 25\%$ (species 3) and $58 \pm 35\%$ (species 4). The increase in the total concentration of NADH upon hypoxia was calculated to be $81 \pm 39\%$, which is substantially greater than the change in the total fluorescence ($48 \pm 26\%$) due to the decrease in the fluorescence average lifetime. The large errors are due to significant variation in the integrated fluorescence response to hypoxia and not to large errors in the fitting parameters. Secondly, the fractional contributions to the fluorescence (f_i) from each species during normoxia can be calculated to be: 7% (species1), 20%

(species 2), 46% (species 3) and 27% (species 4). Note that while species 1 has the largest concentration (44%), it contributes the least to the total fluorescence due to its short lifetime.

The total fluorescence decay exhibits a spike at t_0 due to backscattered excitation light from the tissue that increased by $47 \pm 20\%$ upon hypoxia. This increase in scattered light has been observed during sustained hypoxia and although its cause is not fully understood, is possibly due to mitochondrial swelling (33-35).

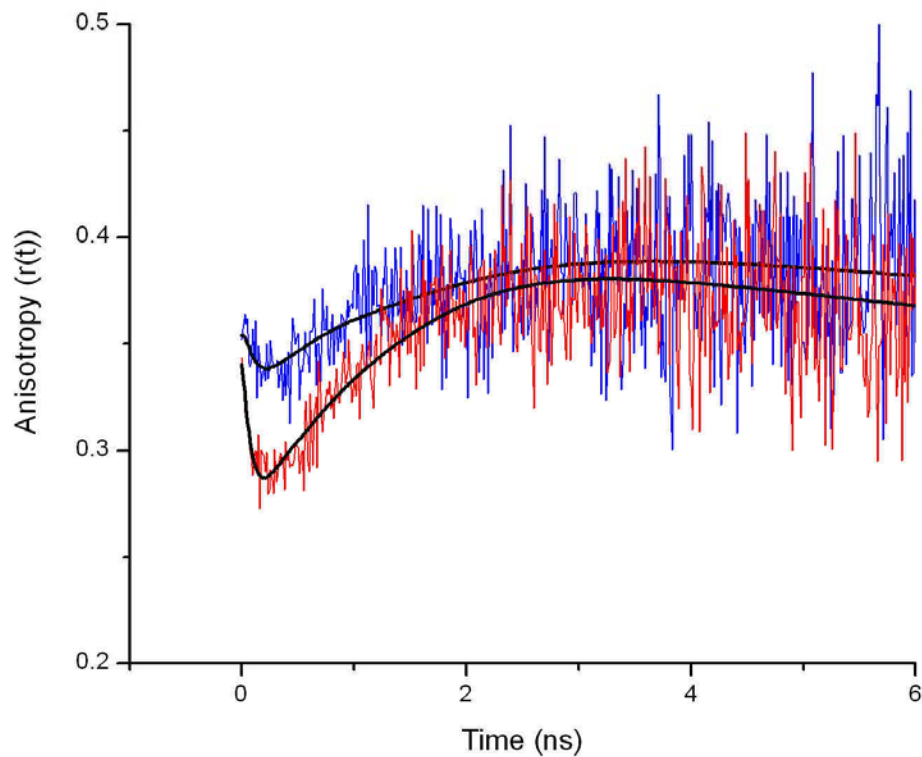


Figure 5.7 Anisotropy decays of intrinsic fluorescence. Both normoxic (blue) and hypoxic (red) decays exhibit the functional form of associated anisotropy – indicating multiple conformations of NADH.

To further characterize the fluorescent species, we calculated the rotational anisotropy decays from the intrinsic tissue parallel and perpendicular fluorescence components. Typical anisotropy decays (Fig.(5.7)) exhibit a rapid initial decay, followed by a rise and then a second slower decay. This form is characteristic of fluorescence anisotropy arising from a mixture of fluorophore species with each species having its own distinct fluorescence decay and fluorescence anisotropy decay, and is known as associated anisotropy (36,37).

Table 5.4 Mean (SEM) anisotropy decay fit parameters.

	r_{01}	θ_1 (ps)	r_{02}	θ_2 (ps)	r_{03}	θ_3 (ps)	r_{04}	θ_4 (ps)
Normoxia	0.42 (0.04)	318 (101)	0.33 (0.01)	8443 (2495)	0.41 (0.02)	∞	0.36 (0.02)	∞
Hypoxia	0.43 (0.06)	230 (58)	0.25 (0.02)	8070 (905)	0.39 (0.01)	∞	0.33 (0.02)	∞

By utilizing the associated anisotropy model in our fitting protocol we determined the rotational diffusion time and initial anisotropy of each species of the total fluorescence decay and thereby characterize the conformations of NADH as a function of metabolic state. The anisotropy parameters (r_{0i}, θ_i) obtained by the fit are summarized in Table (5.4). Of particular note, the shortest lifetime species (species 1) has a fast rotational diffusion time of 318 ± 101 ps during normoxia that decreases upon hypoxia to 230 ± 58 ps. In contrast, all three longer lifetime species are essentially immobile, with large rotational diffusion times that are insensitive to the tissue metabolic state. The two-photon initial anisotropies of all the species are also insensitive to metabolic state, excepting species 2 which exhibits a significant

decrease of the initial anisotropy from 0.33 ± 0.01 to 0.25 ± 0.02 , indicating an increased mode of depolarization faster than our time resolution.

5.3.2 Comparative measurements of NADH in solution

The photophysical properties of the intracellular fluorescence species can be used to physically identify them by comparatively considering the photophysical characteristics of NADH in solution. Free aqueous NADH at room temperature exists in two conformations: folded (stacked nicotinamide and adenine rings) and extended (no such stacking). We measure the total fluorescence decay to be bi-exponential with lifetimes (and amplitudes) 350 ps (0.77) and 760 ps (0.23) giving an average lifetime of 444 ps. The two lifetime components are comparable to those reported in literature and are believed to arise from the extended and folded populations respectively (13,19). The fluorescence anisotropy decay was found to be mono-exponential, with a rotational diffusion time of 290 ps and an initial anisotropy of 0.38 (Fig.(5.8), blue curve). The rotational dynamics reported here are consistent with those reported by Couprie et al (19) who further showed that the NADH rotational diffusion time exhibits a Stokes-Einstein dependence on viscosity and temperature (Eqn.(2.17)). Based on the Stokes-Einstein dependence measured by Couprie et al, we expect a reduced rotational diffusion time for free aqueous NADH of ~ 150 ps at the temperature of tissue in our experiments ($\sim 32^\circ\text{C}$).

NADH fluorescence and anisotropy are sensitive to enzyme binding. As an example, we titrate the large NADH-binding Krebs' cycle enzyme mitochondrial malate dehydrogenase (mMDH, MW=70kD) against NADH (MW=665). At a sufficiently high concentration of mMDH ($[\text{NADH binding sites}]/[\text{NADH}] = 4$), all available NADH is bound. In this case, the fluorescence decay is bi-exponential with components 602 ps (0.72) and 1.33 ns (0.28) yielding an average lifetime of 806 ps.

The anisotropy decays as a mono-exponential with an initial anisotropy of 0.49 and a rotational diffusion time of 30 ns (Fig.(5.8), red curve). The long, single exponential anisotropy decay implies that the NADH fluorophore is rigidly bound without significant segmental mobility within the much larger enzyme.

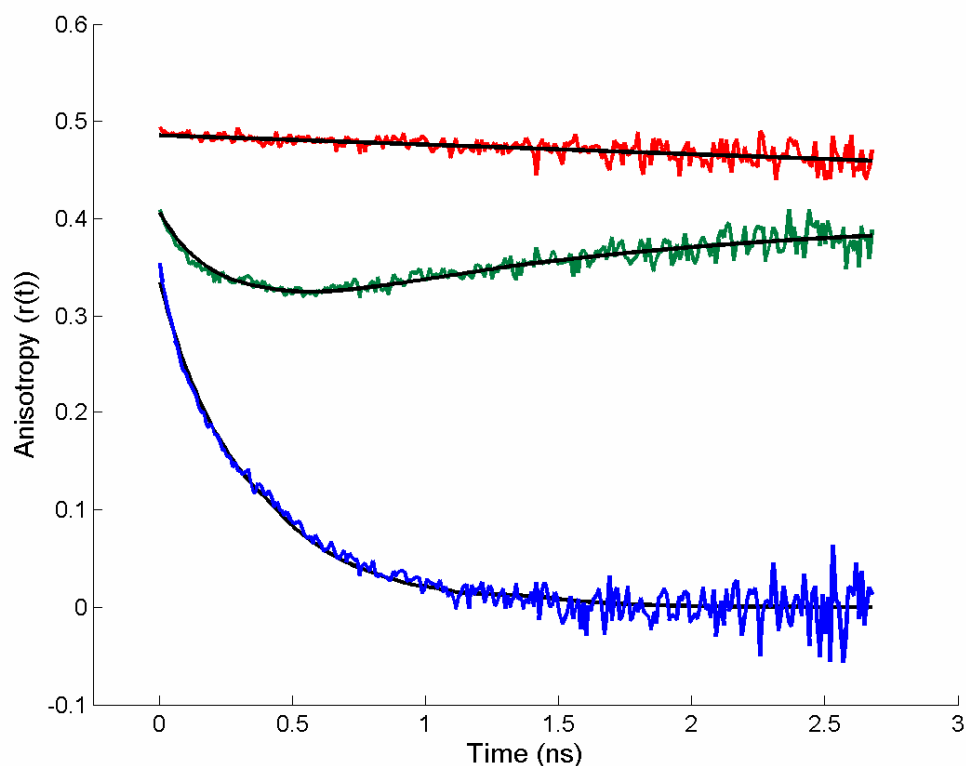


Figure 5.8 Anisotropy of free and bound NADH. Anisotropy of NADH free (blue) and fully bound to mMDH (red) are mono-exponential while a mixture of free and bound species (green) displays associated anisotropy.

At a non-saturating concentration of mMDH ($[NADH \text{ binding sites}]/[NADH] = 0.2$), there is a mixture of free and bound NADH yielding a fluorescence anisotropy decay with the form of associated anisotropy (Fig.(5.8), green curve). The anisotropy of this mixture was fit by setting the rotational and lifetime decay parameter values (Eqns. 12, 13) constant at the values for fully free and fully bound NADH measured

above. The relative population of free and bound NADH ($[NADH]/[NADH\cdot mMDH]$) was however taken as a floating parameter and determined by the global fit to be 1.0. The accuracy of the global fit determination of free/bound NADH was checked by independently estimating the free/bound ratio using the average lifetime of the mixture ($a_{free} \langle \tau_{free} \rangle + a_{bound} \langle \tau_{bound} \rangle = \langle \tau_{mixture} \rangle$, $a_{free} + a_{bound} = 1$; data not shown). This method gave a free/bound NADH ratio of 0.9 – in reasonable agreement with the value obtained from the global fit. The strong resemblance of the anisotropy decay of the bound-free mixture to that observed in tissue is indicative of coexistent free and bound NADH in tissue. This further validates the use of global lifetime and associated anisotropy fitting to discriminate and characterize intracellular free and bound NADH.

5.3.3 Identification of intracellular free and enzyme bound NADH

Comparing the lifetime and rotational anisotropy characteristics of NADH *in vitro* to our results in tissue enables us to identify the observed fluorescent species of intracellular NADH. This identification and the behavior of the species upon hypoxia are summarized in Table (5.5).

Table 5.5 Summary of intrinsic NADH conformation identification

Species	Identification	Concentration (normoxia) (arb. units)	Concentration (hypoxia) (arb. units)	Increase upon hypoxia
1	Free	44	80	82%
2	Bound	32	63	97%
3	Bound	20	27	35%
4	Bound	4	6	50%

The short lifetime species (species 1) has a relatively fast rotational diffusion time somewhat greater than that of aqueous NADH (150ps) at tissue temperature. This

high rotational mobility is consistent with this species being free NADH in a slightly viscous environment. The lifetime of species 1 is comparable to the lifetime of free extended NADH but substantially shorter than the lifetime of free folded NADH. Taken together, the lifetime and anisotropy parameters for species 1 suggest that it is free extended NADH in a slightly viscous environment.

Species 2 has a lifetime that is consistent with being either folded NADH, or enzyme bound NADH. Its rotational diffusion time however (~ 8 ns) is almost two orders of magnitude greater than that of free NADH, indicating that this species is also bound NADH. This species undergoes a significant decrease in its initial anisotropy (0.33 to 0.25) upon hypoxia, indicating an enhanced mode of fast depolarization, e.g. a fast segmental motion of the nicotinamide ring within an enzyme, or a specific interaction in the binding sites which increases the angle between the nicotinamide absorption and emission dipoles. While the cause is uncertain, we can still identify this species as enzyme bound from its diffusion time. The two longest lifetime species (species 3 and 4) are rotationally immobile on the timescale of our measurement window (~ 10 ns) and their lifetimes are much greater than the lifetimes of either folded or extended aqueous NADH. Both the highly enhanced lifetime and rotational immobility suggest that these two species are NADH bound to enzymes. The identification of species 2, 3 and 4 as enzyme bound does not imply that there are only three different enzymes binding NADH. In reality there are known to be many different enzymes binding NADH, and their net fluorescence is observed as components 2, 3 and 4.

It is noteworthy that we do not observe the expected ~ 600 ps fluorescence decay component of free folded NADH in brain slices. However, it is difficult to say whether this reflects an inability to separately resolve its decay, or a genuinely small intracellular concentration of free folded NADH.

From the identification of these species, the relative concentration of free NADH is given by the amplitude of species 1 ($a_{\text{free}}=a_1$) while the relative total concentration of bound NADH is given by the sum of the amplitudes of the 3 bound species ($a_{\text{bound}}=a_2 + a_3 + a_4$). The ratio of the free/bound NADH ($a_{\text{free}}/a_{\text{bound}}$) can then be calculated to be 0.78 ± 0.05 during normoxia and remains essentially unchanged upon hypoxia. Even though hypoxia does not affect the ratio of free NADH to the total concentration of bound NADH, it does affect the relative populations of the three enzyme bound species (Table (5.3)), indicating a redistribution of NADH among different enzymes. Hence while the free NADH concentration appears to remain approximately equal to the total concentration of bound NADH, its distribution amongst various bound species changes with its chemical potential – indicating a range of binding constants and cofactor concentrations in the intracellular environment.

5.3.4 Calculating the local intracellular viscosity

Having identified species 1 as free NADH, we can use its rotational diffusion time with the Stokes-Einstein relation for free NADH measured by Couprie et al (19) to calculate the local intracellular viscosity. In this way, the local viscosity experienced by free intracellular NADH is calculated to be $1.6\pm 0.5\text{mPa s}$ (2.1 ± 0.7 relative to water at 32°C) during normoxia and decreases upon hypoxia to $1.1\pm 0.3\text{mPa s}$ (1.5 ± 0.4 relative to water at 32°C).

5.3.5 Discussion of intracellular conformation and environment

Enzyme binding of NADH has been characterized by a number of fluorescence techniques that are differently sensitive to binding. The weakest effect is the shift of the NADH emission peak upon binding which is typically less than 10% ($\Delta\lambda/\lambda < 0.1$).

The lifetime of NADH is more sensitive to enzyme binding and can be enhanced by a factor of $\Delta\tau/\tau \sim 1-10$. Fluorescence anisotropy offers an even greater sensitivity to enzyme binding due to the large difference in size between NADH (MW=665) and the enzymes that tightly bind it, e.g. mitochondrial malate dehydrogenase has a molecular weight of 70kD. Enzyme binding increases the rotational diffusion time of NADH by more than an order of magnitude ($\Delta\theta/\theta \sim 10-100$), rendering the fluorophore effectively immobile on our time scale of measurement. Hence, measuring the rotationally mobile versus immobile intracellular NADH offers the most sensitive fluorescence probe of the free versus bound conformation.

Based on our measurements of rotational anisotropy, we conclude that intracellular NADH exists in both free and bound forms in comparable concentrations (free/bound = 0.78). However, it is the bound NADH that dominates (93%) the total tissue fluorescence due to its substantially enhanced lifetime. This dominance of the bound NADH fluorescence has lead analyses of the wavelength resolved tissue fluorescence spectra to prematurely conclude that tissue NADH is almost completely enzyme bound (10). In contrast, our results indicate that free NADH is in fact significant in concentration if not in fluorescence.

The ratio of free NADH to individual enzyme bound species of NADH is found to change significantly upon hypoxia, while the ratio of free NADH to total bound NADH does not. This indicates a redistribution of NADH amongst enzyme binding sites. Specifically, there is a large increase in the concentration of free NADH and the concentration of NADH bound to enzymes that cause low lifetime enhancement. The concentration of NADH bound to those enzymes causing large lifetime enhancement increases to a lesser extent. The net effect of this redistribution of NADH among binding sites is a decrease in the average lifetime of the intrinsic fluorescence, causing the observed fluorescence increase (48%) to underestimate the

calculated concentration increase (81%). Since the ratio of free to bound NADH does not change upon hypoxia, this calculated concentration increase applies to both free and bound pools of NADH.

In comparison, assays of chemically extracted NADH from cerebral cortical brain slices showed that the total NADH concentration increased by 107% upon acute hypoxia (5). Metabolite indicator methods reveal a 105% increase in the free mitochondrial NADH (8) in brain upon hypoxia. These concentration increases are clearly much closer to our calculated concentration increase than to our observed fluorescence increase. However, a strict comparison should not be drawn between our results and the results of the metabolic indicator method as NADH increases are dependent upon the degree of hypoxia as well as the region of the brain, both of which may differ from our experiments.

In relating fluorescence changes to concentration changes, we have assumed that changes in the quantum yield are proportional to changes in the lifetime. This is only strictly true if the radiative rate remains constant (Eqn.(5.1)). The radiative rate depends on the overlap of excited and ground states, which can be expressed as a function of the fluorescence and absorption spectral lineshapes (shape of the normalized spectra) as expressed by the Strickler-Berg relation (30). We find that the lineshape of the NADH portion of the intrinsic fluorescence changes only slightly upon hypoxia (Fig.(3.12)) - suggesting that the average radiative rate of intracellular NADH is not significantly altered. However this is not conclusive as we do not know the behavior of the absorption spectral lineshape.

The rotational dynamics of intracellular free NADH indicate a relatively low viscosity ($\sim 1.6 \text{ mPa s}$). This is not unexpected as fast rotational diffusion and conformational changes take place on length scales that are short and therefore sensitive to only the immediate fluid phase viscosity and molecular crowding (together

known as the effective viscosity) (38). Local fluid phase viscosities comparable to that of water have been observed in a number of cells and sub-cellular compartments, including mitochondria (23,24,38,39).

The decrease in the intracellular viscosity upon hypoxia (to 1.1mPa s) possibly reflects a dilution of the intracellular environment caused by the osmotic swelling of the cell soma and mitochondria. Sustained hypoxia is known to induce osmotic cell swelling and an increase in scattered light (33-35). The cause of this increase in scattered light is unknown, however it has been suggested that it is due to mitochondrial swelling (33) in response to hypoxia induced spreading depression. It is thought that mitochondrial swelling increases the cross-section of scatterers and therefore the scattering signal, assuming that there is a significant difference between the refractive index of mitochondria and of the cytosol. Given that we also observe an increase in scattered light upon hypoxia, it is plausible that compartmental swelling and the resulting dilution is reducing the intracellular viscosity.

As we have seen, the response of NADH to hypoxic metabolic inhibition is more complicated than a simple concentration increase. Changes occur in not only the concentration, but also in the conformation and the environment of intracellular NADH. We have presented here a means to discriminate and monitor these effects, enabling a more precise measurement of the dynamics of the actual intracellular NADH concentration and its partition into free and bound pools.

5.4 Regional variations of intrinsic NADH photophysics

Imaging experiments have shown that the magnitude of the fluorescence response to hypoxia is region specific. In particular, the fluorescence increase in the dendritic layer (stratum radiatum; SR) is 2-3 times greater than the increase in the cell soma layer (stratum pyramidale; SP). The variation of metabolic response reflects

differences in mitochondrial populations between different regions. This difference in the mitochondrial population also entails a different average environment for NADH in these regions. In order to characterize the differences in the photophysical properties of NADH in these different regions, we measured the time resolved intrinsic fluorescence in the CA1 SR and SP.

The time-averaged intrinsic fluorescence of the SR increased by $37 \pm 11\%$ in response to hypoxia. The average excited state fluorescence lifetime (1.2 ± 0.2 ns) is reduced (1.01 ± 0.09 ns) upon hypoxia. The response of the SP (cell layer) to hypoxia is qualitatively similar to that of the SR, with relatively minor differences. The magnitude of the response to changing metabolic state was generally lower. The integrated fluorescence increased by $17 \pm 7\%$. The average lifetime decreased upon hypoxia from 1.03 ± 0.08 ns to 0.91 ± 0.07 ns. The average decays from both regions and under both normoxia and hypoxia are shown in Fig.(5.9). The most obvious difference between the two regions is that the SP fluorescence is only slight affected by metabolic state while the SR effect is more substantial.

These experiments measured gross spatial variation in the decay characteristics of NADH fluorescence with respect to two morphologically different regions of the hippocampal CA1 layer. However, in order to accurately measure the scale of these spatial variations, it is necessary to use an imaging modality. Future experiments will employ fluorescence lifetime imaging to measure spatial variations within the hippocampus with cellular and sub-cellular resolution.

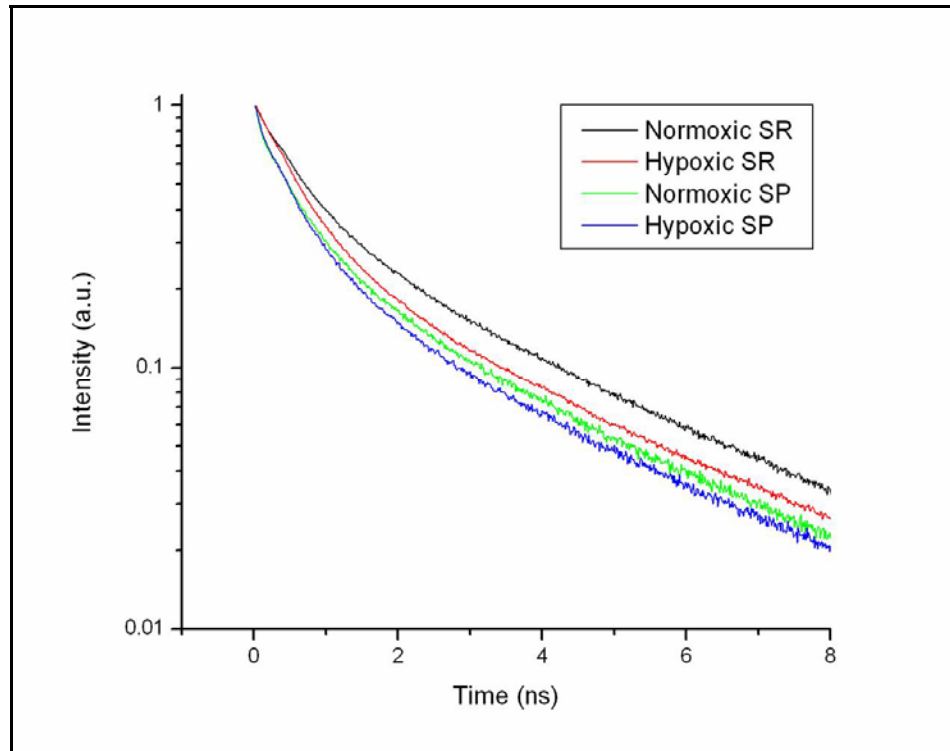


Figure 5.9 Lifetimes and hypoxic responses of different hippocampal regions.

5.5 Concentration calibration of intracellular NADH

In order to measure absolute concentration of NADH in the hippocampus, we compared fluorescence images of slices using two-photon laser scanning microscopy to the fluorescence of aqueous NADH solutions of known concentrations imaged under identical conditions. The solution fluorescence provides a calibration of fluorescence as a function of NADH concentration that is not yet corrected for light attenuation and the enhancement of the fluorescence quantum yield in tissue.

Correction for light attenuation: The decrease of the NADH fluorescence signal with depth is a function of light attenuation on one hand and the increase in the NADH concentration as a function of decreasing tissue oxygen on the other. However, NADH does not increase significantly until the local PO_2 falls to less than 0.1 atm. For a normoxic perfusate PO_2 (>0.6 atm), the oxygen level in tissue does not fall to this

level until a depth of $>60\mu\text{m}$ (see Section (2.6)). Hence the attenuation of the NADH signal in the superficial $60\mu\text{m}$ of a brain slice is due only to light attenuation.

The depth attenuation of the NADH fluorescence down to a depth of $60\mu\text{m}$ can be fit to an exponential decay (Fig.(5.10a)), with deviation occurring in the first 10-20 μm due to superficial cell death as a consequence of slice preparation. Having characterized the fluorescence attenuation, we can correct for this factor in images taken in deeper, healthy tissue (below 30 μm).

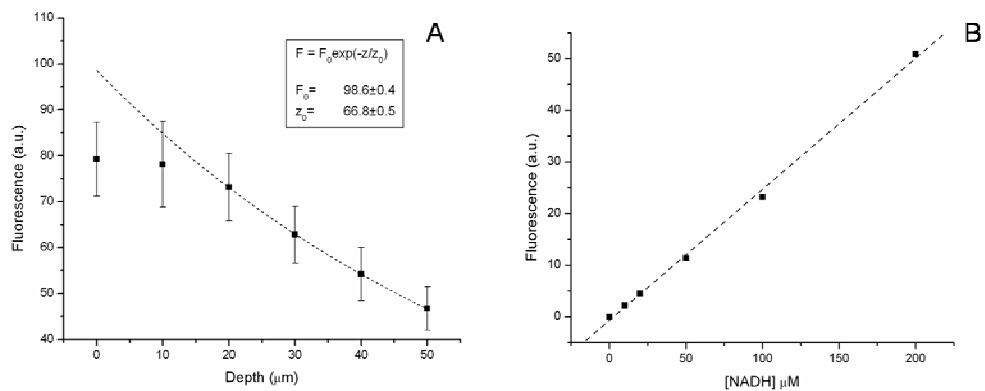


Figure 5.10 Calibrating intrinsic NADH fluorescence to concentration. Calibrating NADH fluorescence requires first characterizing the fluorescence attenuation (A) and then relating fluorescence and concentration (B) using standard solutions of NADH.

The attenuation corrected tissue fluorescence can then be compared to the fluorescence of aqueous NADH standards of known concentrations (Fig.(5.10b)) to provide a first estimate map of tissue NADH concentration. This first estimate (Fig.5.11) needs to be further corrected for the enhanced quantum yield of intrinsic NADH.

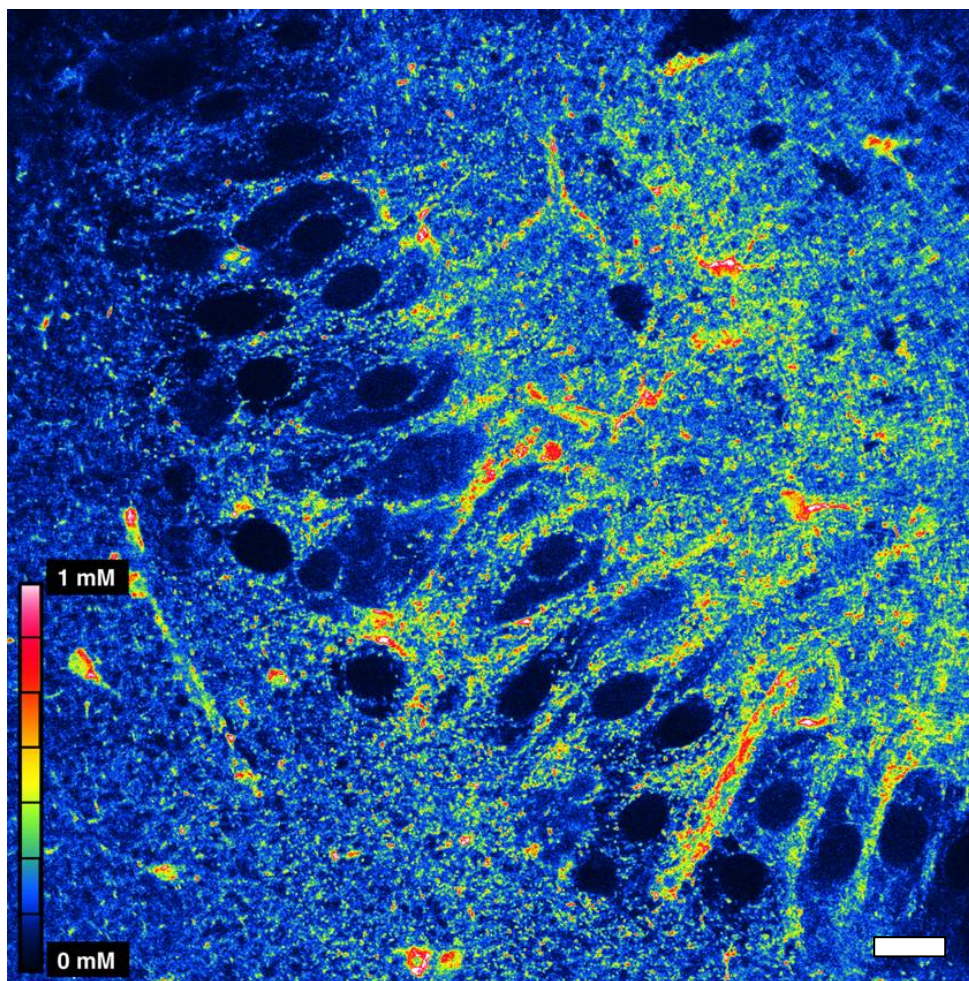


Figure 5.11 Map of NADH concentration - before correcting for quantum yield.
Scale bar is 20 μ m.

The enhancement of the quantum yield is simply the product of the enhancement of the radiative rate and the enhancement of the lifetime as measured by steady state and time resolved spectroscopy respectively. The measurement of these enhancement factors for both SR and SP have been discussed in previous sections and are summarized in Table (5.6). The fluorescence lineshape, and therefore the radiative rate, does not change significantly upon hypoxia. Since there is no way to measure the two-photon absorption spectrum in tissue, the contribution of the absorption integral

term to the radiative rate cannot be calculated here. However, as discussed above, the contribution of the absorption shift to a change in the radiative rate is small ($< \sim 3\%$) and can be neglected.

Table 5.6 Correction factors for estimating intrinsic NADH concentration.

Region	Enhancement			Uncorrected Concentration (μM)	Corrected Concentration (μM)
	Lifetime	Radiative Rate	Quantum Yield		
SR Normoxic	3.0 ± 0.4	1.09 ± 0.06	3.3 ± 0.4	390	119
SR Hypoxic	2.5 ± 0.2	1.09 ± 0.06	2.7 ± 0.2	534	195
SP Normoxic	2.5 ± 0.2	1.09 ± 0.06	2.7 ± 0.2	250	92
SP Hypoxic	2.3 ± 0.2	1.09 ± 0.06	2.5 ± 0.2	288	115

Under normoxic conditions, the uncorrected average concentration in the SR is calculated to be $\sim 390 \mu\text{M}$ and that in the SP is $\sim 250 \mu\text{M}$. Taking into account the enhancement of the quantum yields, the corrected average concentration in the SR is $119 \mu\text{M}$ while that in the SP is $92 \mu\text{M}$. Upon hypoxia, the total NADH concentration increases by 64% (to $195 \mu\text{M}$) in the SR and by 25% (to $115 \mu\text{M}$) in the SP. In contrast, the NADH fluorescence (uncorrected concentration) increases by only 37% in the SR and 13% in the SP. Hence we see already a significant error in the measure of concentration and concentration changes if the quantum yield is not monitored.

Analytical chemistry measurements of the NADH content in rodent brain tissue extracts typically fall in the range of ~ 57 - $128 \mu\text{M}$ (4,40,41). In particular Klaidman et al (4) used HPLC to determine the concentration of NADH in the mouse

hippocampus to be 0.057 ± 0.018 $\mu\text{mol/g}$ of brain tissue and the total NADH and NAD⁺ concentration to be 0.253 ± 0.037 $\mu\text{mol/g}$ brain tissue. These measurements correspond to an average intracellular NADH molar concentration of ~ 57 μM and a combined NADH and NAD⁺ concentration of ~ 253 μM , assuming the density of brain tissue to be roughly that of water.

The total concentration of NADH and NAD⁺ measured by these techniques is particularly important as it represents the maximal concentration that NADH can have in the tissue under the condition of complete reduction of the redox pair. This total concentration of NADH and NAD⁺ does not depend upon the specific metabolic state of the tissue nor is it sensitive to artefactual oxidation of NADH during sample preparation – which can be a problem in these types of measurements (4). The NADH level alone however is not a constant, but rather a variable that depends on the metabolic state.

While analytical chemistry (HPLC) has been able to measure NADH concentrations in gross tissue samples, these techniques entail destroying the tissue and are have the potential for artefactual oxidation of NADH during preparation. Two photon time resolved fluorescence measurement offers a probe of intracellular NADH excited state dynamics that is non-invasive and causes minimal photodamage, enabling prolonged data acquisition from a single living hippocampal slices in a controlled metabolic state.

5.6 Optical properties of brain slices

5.6.1 Absorption

Fluorescent chromophores intrinsic to biological tissue have been discussed earlier in Section (3.1). Besides these, there are also chromophores that absorb without fluorescence. Tissue absorbers that are metabolically inert (e.g. melanin) represent a

constant attenuation of excitation and emission light. However, tissue absorption spectra from 510 to 620nm contain distinct peaks that reflect the oxidation states of the several cytochromes in the electron transport chain (42) and therefore the metabolic state of the cell. Given the wavelength of these peaks, neither the two-photon excitation (730-740nm) nor emission (400-550nm) of NADH fluorescence overlaps significantly with these absorption peaks and are therefore not sensitive to cytochrome oxidation states - beyond the direct biochemical coupling of NADH concentration to metabolic state.

Jobsis (43) first demonstrated that near infrared spectroscopy can be used to monitor oxygen consumption in brain tissue by resolving spectral contributions of cytochrome oxidase (CytOx), hemoglobin (Hb) and oxygenated hemoglobin (HbO₂) to absorption in the 700-1000nm wavelength range. In brain slices, the differential absorption of Hb and HbO₂ is irrelevant as the brain slice is largely exsanguinated and receives oxygen directly from the perfusion medium. The absorption of light due to CytOx is dependent upon its oxidation state. The difference between oxidized and reduced CytOx specific extinction coefficient is $\Delta\epsilon \sim 0.002 \mu\text{M}^{-1}\text{cm}^{-1}$ at 700-750nm (44). At path length scales relevant to functional imaging in brain slices ($\sim 100\mu\text{m}$) and cytochrome oxidase concentrations typical of 2-3 week old rat brain ($\sim 3\mu\text{M}$)(45), this difference in extinction is $\Delta\epsilon \sim 6 \times 10^{-5}$. Assuming a maximal change in the CytOx oxidation state, the resulting fractional change in the attenuation of the red excitation beam reaching the focal plane is $\exp(-\Delta\epsilon) = 0.99994$. This is a negligible change, and hence we can ignore absorption changes due to the cytochrome oxidase oxidation state.

5.6.2 Scattering

Scattering due to morphological changes is monitored $>620\text{nm}$ as absorption changes in this region are small. Chance et al (1963) (46) measured the reflectance change at 700-710nm to be negligible upon anoxia in rat cortex. There were scattering changes in the 400-550nm region of NADH emission, however scattering changes of emission should not substantially affect the efficiency of collection as, on average, just as many photons scatter into our collection optics as scatter out of them.

Scattering changes are affected by the cellular and sub-cellular morphology of brain slices. Changes in morphology in turn depend upon the nature of the physiological perturbation of the brain tissue. These perturbations are usually via:

1. Osmolarity
2. Excitation
 - a. Sustained tetanic stimulation
 - b. Bulk depolarization (by K^+ or NMDA injection)
3. Hypoxia
 - a. Brief hypoxia without spreading depression
 - b. Sustained hypoxia with spreading depression

Depending upon the specific perturbation, the morphological changes can include cellular swelling/shrinkage, mitochondrial swelling/shrinkage, and dendritic beading.

During sustained hypoxia (~ 10 min), Bahar et al (34) found that a depolarization of the mitochondrial membrane (indicated by rhodamine 123 fluorescence increase) was accompanied by a biphasic response of the transmittance (at $\sim 650\text{nm}$) – an initial brief and small increase followed by a large sustained decrease. Measurements of interstitial volume and transmittance/scattering during osmotic perturbations have shown that cellular swelling is associated with increased transmittance (reduced scattering) (47,48)). Cellular swelling is known to occur during

hypoxia (49,50) and hence one might expect a reduction in scattering upon hypoxia, however the opposite has been observed. While the mechanism of this hypoxia induced scattering increase is not fully understood, it is known to occur with hypoxic spreading depression. Muller & Somjen (33) have suggested mitochondrial swelling as a possible cause assuming that the mitochondrial refractive index is sufficiently different from that of the cytoplasm. The bi-phasic response of the transmittance observed by Bahar et al could then be interpreted as a superposition of two different effects – cellular swelling induced scattering decrease and mitochondrial swelling induced scattering increase (35).

5.7 Conclusions

Metabolic perturbations to neural tissue have a wide range of effects that can influence the intrinsic NADH fluorescence. Unless these effects are accounted for, we cannot interpret changes in NADH fluorescence as strictly representing changes in NADH concentration. Among these effects, we have found that the binding state and local viscosity of intracellular NADH are sensitive to metabolic state. The net effect of the conformation and environmental changes on the lifetime of intracellular NADH causes the fluorescence change upon hypoxia to significantly underestimate the concentration change. We have used fluorescence lifetime and rotational anisotropy to measure these effects and thereby correct for them. The resulting calculation of NADH concentration change in response to hypoxia is in good agreement with analytical chemistry measurements and has the added advantage of being non-destructive.

It is a logical next step to apply this time resolved fluorescence-anisotropy probe to an imaging modality to explore the spatial heterogeneity of the NADH

concentration and conformation – both on an inter-cellular (e.g. neurons vs. astrocytes) and sub-cellular compartment level.

Furthermore, throughout this work, we have assumed that the local refractive index of intracellular NADH is unchanged. We have also assumed that the NADH two-photon absorption cross section experiences no significant change in amplitude or wavelength in tissue. Future work needs to clarify how these parameters are affected for intracellular NADH.

NADH fluorescence has seen a resurgence in its use as an intrinsic probe of a wide range of interesting cellular and tissue phenomena, ranging from neuro-metabolic coupling (51) to nuclear transcription regulation (52), to enzyme kinetics within intact cells (53). The fluorescence based assay of NADH concentration and conformation presented here will enhance our ability to precisely quantify the role of NADH in these phenomena and develop an accurate picture of NADH biochemistry *in vivo*.

References

1. Chance, B., Jobsis, F., Schoener, B., and Cohen, P. (1962) *Science* **137**, 499-&
2. Chance, B., and Williams, G. R. (1956) *Advances in Enzymology and Related Subjects of Biochemistry* **17**, 65-134
3. Williams.Dh, Lund, P., and Krebs, H. A. (1967) *Biochemical Journal* **103**, 514-&
4. Klaidman, L. K., Leung, A. C., and Adams, J. D. (1995) *Analytical Biochemistry* **228**, 312-317
5. Garofalo, O., Cox, D. W. G., and Bachelard, H. S. (1988) *Journal of Neurochemistry* **51**, 172-176
6. Bucher, T., Brauser, B., Sies, H., Langguth, O., Conze, A., and Klein, F. (1972) *European Journal of Biochemistry* **27**, 301-&
7. Merrill, D. K., and Guynn, R. W. (1976) *Journal of Neurochemistry* **27**, 459-464
8. Merrill, D. K., and Guynn, R. W. (1982) *Brain Research* **239**, 71-80
9. O'Connor, D. V., and Philips, D. (1984) *Time correlated single photon counting*, Academic Press, London
10. Chance, B., and Baltscheffsky, H. (1958) *Journal of Biological Chemistry* **233**, 736-739
11. Salmon, J. M., Kohen, E., Viallet, P., Hirschberg, J. G., Wouters, A. W., Kohen, C., and Thorell, B. (1982) *Photochemistry and Photobiology* **36**, 585-593
12. Velick, S. F. (1961) in *A Symposium on Light and Life* (McElroy, W. D., and Glass, B., eds), pp. 108-143, The Johns Hopkins Press, Baltimore, MD
13. Gafni, A., and Brand, L. (1976) *Biochemistry* **15**, 3165-3171
14. Paul, R. J., and Schneckenburger, H. (1996) *Naturwissenschaften* **83**, 32-35
15. Wakita, M., Nishimura, G., and Tamura, M. (1995) *Journal of Biochemistry* **118**, 1151-1160
16. Hones, G., Hones, J., and Hauser, M. (1986) *Biological Chemistry Hoppe-Seyler* **367**, 103-108

17. Knutson, J. R., Beechem, J. M., and Brand, L. (1983) *Chemical Physics Letters* **102**, 501-507
18. Lakowicz, J. R. (1999) *Principles of Fluorescence Spectroscopy*, 2 Ed., Kluwer Academic/Plenum Publishers
19. Couprie, M. E., Merola, F., Tauc, P., Garzella, D., Delboulbe, A., Hara, T., and Billardon, M. (1994) *Review of Scientific Instruments* **65**, 1485-1495
20. Scott, T. G., Spencer, R. D., Leonard, N. J., and Weber, G. (1970) *Journal of the American Chemical Society* **92**, 687-&
21. Wilhelmi, B. (1982) *Chemical Physics* **66**, 351-355
22. Lakowicz, J. R., Szmecinski, H., Nowaczyk, K., and Johnson, M. L. (1992) *Proceedings of the National Academy of Sciences of the United States of America* **89**, 1271-1275
23. Kao, H. P., Abney, J. R., and Verkman, A. S. (1993) *Journal of Cell Biology* **120**, 175-184
24. Partikian, A., Olveczky, B., Swaminathan, R., Li, Y. X., and Verkman, A. S. (1998) *Journal of Cell Biology* **140**, 821-829
25. Velick, S. F. (1958) *Journal of Biological Chemistry* **233**, 1455-1467
26. Lamanna, J. C., Griffith, J. K., Cordisco, B. R., Lin, C. W., and Lust, W. D. (1992) *Canadian Journal of Physiology and Pharmacology* **70**, S269-S277
27. Mitchell, P., and Moyle, J. (1969) *European Journal of Biochemistry* **7**, 471-&
28. Jardetzki, O., and Wade, J. D. (1966) *Journal of Biological Chemistry* **241**, 85-&
29. Czochralska, B., Kawczynski, W., Bartosz, G., and Shugar, D. (1984) *Biochimica Et Biophysica Acta* **801**, 403-409
30. Strickler, S. J., and Berg, R. A. (1962) *Journal of Chemical Physics* **37**, 814-822
31. Lide, D. R. (2004) *CRC Handbook of Chemistry and Physics*, 84 Ed., CRC Press
32. Toptygin, D., Savtchenko, R. S., Meadow, N. D., Roseman, S., and Brand, L. (2002) *Journal of Physical Chemistry B* **106**, 3724-3734
33. Muller, M., and Somjen, G. G. (1999) *Journal of Neurophysiology* **82**, 1818-1831

34. Bahar, S., Fayuk, D., Somjen, G. G., Aitken, P. G., and Turner, D. A. (2000) *Journal of Neurophysiology* **84**, 311-324
35. Fayuk, D., Aitken, P. G., Somjen, G. G., and Turner, D. A. (2002) *Journal of Neurophysiology* **87**, 1924-1937
36. Bialik, C. N., Wolf, B., Rachofsky, E. L., Ross, J. B. A., and Laws, W. R. (1998) *Biophysical Journal* **75**, 2564-2573
37. Fisz, J. J. (1996) *Chemical Physics Letters* **259**, 579-587
38. Garcia-Perez, A. I., Lopez-Beltran, E. A., Kluner, P., Luque, J., Ballesteros, P., and Cerdan, S. (1999) *Archives of Biochemistry and Biophysics* **362**, 329-338
39. Hess, S. T., Sheets, E. D., Wagenknecht-Wiesner, A., and Heikal, A. A. (2003) *Biophys. J.* **85**, 2566-2580
40. Glock, G. E., and McLean, P. (1955) *Biochemical Journal* **61**, 388-390
41. Jedeikin, L., and Weinhouse, S. (1955) *Cancer Research* **2**, 26-26
42. Chance, B., and Williams, G. R. (1955) *Journal of Biological Chemistry* **217**, 395-407
43. Jobsis, F. F. (1977) *Science* **198**, 1264-1267
44. Delpy, D. T., and Cope, M. (1997) *Philosophical Transactions of the Royal Society of London Series B-Biological Sciences* **352**, 649-659
45. Brown, G. C., Crompton, M., and Wray, S. (1991) *Biochimica Et Biophysica Acta* **1057**, 273-275
46. Chance, B., Legallais, V., and Schoener, B. (1963) *Review of Scientific Instruments* **12**, 1307
47. Aitken, P. G., Fayuk, D., Somjen, G. G., and Turner, D. A. (1999) *Methods* **18**, 91-103
48. Kreisman, N. R., Lamanna, J. C., Liao, S. C., Yeh, E. R., and Alcala, J. R. (1995) *Brain Research* **693**, 179-186
49. Perezpinon, M. A., Tao, L., and Nicholson, C. (1995) *Journal of Neurophysiology* **74**, 565-573
50. Jing, J., Aitken, P. G., and Somjen, G. G. (1994) *Journal of Neurophysiology* **71**, 2548-2551

51. Kasischke, K. A., Vishwasrao, H. D., Fisher, P. J., Zipfel, W. R., and Webb, W. W. (2004) *Science* **305**, 99-103
52. Zhang, Q. H., Piston, D. W., and Goodman, R. H. (2002) *Science* **295**, 1895-1897
53. Joubert, F., Fales, H. M., Wen, H., Combs, C. A., and Balaban, R. S. (2004) *Biophysical Journal* **86**, 629-645